PHYSICAL REVIEW B **106**, 075129 (2022)

Real-space numerical renormalization group computation of transport properties in side-coupled geometry

Ana Luiza Ferrari[*] and Luiz Nunes de Oliveira
University of São Paulo, Instituto de Física de São Carlos, São Carlos, SP 13566-990, Brazil

(Received 8 September 2021; revised 28 June 2022; accepted 14 July 2022; published 16 August 2022)

A real-space formulation of the numerical renormalization group (NRG) procedure is introduced. The real-space construction, dubbed eNRG, is more straightforward than the NRG discretization, and allows a faithful description of the coupling between quantum dots and conduction states even if the design of the couplings is intricate. General features of the two procedures are discussed comparatively. A more specific comparison is then developed, based on computations of the zero-bias transport properties for an Anderson-model description of a quantum wire side-coupled to a single quantum dot. An eNRG computation is shown to reproduce accurately the temperature-dependent electrical conductance for the uncorrelated model in the continuum limit, while significant deviations mark the corresponding NRG computation for thermal energies comparable to the conduction bandwidth. A combination of analytical and numerical results for the transport properties of the correlated model then provides a more exacting check on the accuracy of the eNRG procedure. A recent NRG analysis mapping the transport properties of a single-electron transistor onto universal functions of the temperature scaled by the Kondo temperature is extended to the side-coupled device, on the basis of eNRG reasoning. Numerical results for the electrical conductance, thermopower, and thermal conductance in side-coupled geometry are then shown to agree very well with the mappings. The numerical results are also checked against the thermal dependence of the thermopower measured by Köhler *et al.* [Phys. Rev. B **77**, 104412 (2008)] in $Lu_{0.9}Yb_{0.1}Rh_2Si_2$, and the remarkably accurate, recent conductance measurements by Xu *et al.* [Chin. Phys. Lett. **38**, 087101 (2021)].

DOI: 10.1103/PhysRevB.106.075129

I. INTRODUCTION

The numerical renormalization group method was proposed five decades ago, to calculate the thermodynamic properties of dilute magnetic alloys [1–3]. Since then, the scope of applications has been extended to include excitation and transport properties [4]. These developments and subsequent advances have converted the method into an apt instrument in the rapidly growing area of nanodevice development [5]. Numerous examples constitute recent literature [6–24].

The modifications have made the procedure more efficient, more accurate, or more general [4,25–27]. All of them have nonetheless preserved the core of Wilson's construction: logarithmic discretization of the conduction band followed by a Lanczos transformation, truncation, and definition of a renormalization group transformation.

That momentum-space construction seems less attractive today than in the 1970's. Approximations in real space suit the geometry of nanofabricated devices better than their counterparts in k-space. Granted, when the target is an elementary device, Bloch states are quite satisfactory. Consider, for example, the side-coupled device (SCD), a quantum dot side-coupled to a quantum wire, or the single-electron transistor, a quantum dot bridging two otherwise independent two-dimensional electron gases. The tunneling between the quantum dots and the conduction bands in the two devices are usually modeled by momentum-independent couplings. The logarithmic discretization, the subsequent Lanczos transformation, and the truncation in the standard NRG construction then leave the couplings intact, which guarantees numerical results to be uniformly accurate. What is more, it is safe to disregard any momentum dependence, given that rigorous renormalization group arguments associate the energy-dependent terms to irrelevant operators, which give no contribution to the universal physical properties of those two simple devices [3].

In more elaborate geometries, by contrast, the spatial arrangement of the quantum dots typically amounts to couplings with strong momentum dependence, which may introduce marginal operators, or even relevant ones [28]. This raises an issue, for the projection of the model Hamiltonian onto the basis of the logarithmically discretized states describes the momentum dependence only approximately. The result is intolerable deviations. To deal with difficulties of this nature, ingenious extensions of the logarithmic discretization have been developed [4]—at the expense of simplicity, alas.

Simplicity is an asset, one that is especially important in this context because it offers insight. Guided by this notion, we tread an alternative route to avoid the aforesaid unhandiness of the NRG formalism, and discretize the conduction band in real space. The discretization is analogous to the momentum-space formulation. Instead of lumping conduction states in logarithmically spaced intervals into discrete levels, the alternative approach assembles sites belonging to

---

[*] Corresponding author: ana.luiza.ferrari@usp.br

real-space blocks of exponentially growing size into discrete states. As a reminder of this exponential growth, we dub the alternative formulation eNRG. The resulting renormalization group transformation is practically identical to the NRG transformation at low energies, small in comparison with the conduction bandwidth. The virtues of the traditional approach are therefore preserved: rapid convergence of physical properties to the continuum limit, uniform accuracy over parametrical spaces, access to the tools of renormalization group theory, and relatively small computational cost. At higher energies, the eNRG and NRG transformations are distinct, and the former describes physical properties more accurately, as a simple example focused on a side-coupled device with momentum-independent coupling to a structureless conduction band will show. In more complex geometries, with more quantum dots and one or more wires, the real-space construction in the eNRG method guarantees the description of all couplings to be exact.

Notably, a parameter in the eNRG construction controls the number of lattice sites that the discretization will spare, while the other sites are lumped. Adjustment of this parameter ensures that all sites coupled to quantum dots be spared. As a result, physical properties numerically computed with the discretized Hamiltonian are uniformly accurate, independently of the couplings or Coulomb interactions. The parameter warrants uniform accuracy even if intricate designs couple the quantum dots to Wannier states. Likewise, adequate setting of the same parameter describes nonuniform densities of states accurately. Therefore simple adjustment of a parameter in the eNRG procedure is sufficient to eliminate two sources of error that require multiple transformations in the NRG approach.

The major thrust of this report is to describe the eNRG procedure and bring out its simplicity. With this in mind, we defer to subsequent work the analysis of more complex geometries and corroborate the above-mentioned virtues with a transparent illustration dovetailing numerical and analytical treatments. Specifically, our illustrative study will target the zero-bias transport properties of the side-coupled device and derive exact analytical results to demonstrate the precision of the new procedure. The same analytical results prove practical to interpret experimental data, as two independent examples will show.

The presentation is split into five sections. Section II defines the system and model that will serve as test beds. Section III describes the eNRG construction. Section IV then compares the new method with the NRG approach, on the basis of general arguments, numerical results, and fits to experimental data. Section V summarizes the findings and is followed by four appendices with technical details. In particular, Appendix B supports the discussion in the first part of Sec. IV.

II. MODEL

As Fig. 1 indicates, the SCD comprises a quantum dot weakly coupled to a quantum wire. Small electrical or thermal biases applied between the tips of the wire induce the electrical and thermal currents that determine the transport properties. At high temperatures, the coupling to the dot offers little resistance to conduction across the wire, even if the gate potential in the illustration is adjusted to favor formation of a magnetic moment at the quantum dot. Upon cooling, the coupling between the dot and conduction-electron spins gradually forms a Kondo cloud that screens the dot moment. The cloud obstructs transport. The electrical and thermal conductances are substantially reduced as the temperature falls below the Kondo temperature T_K.

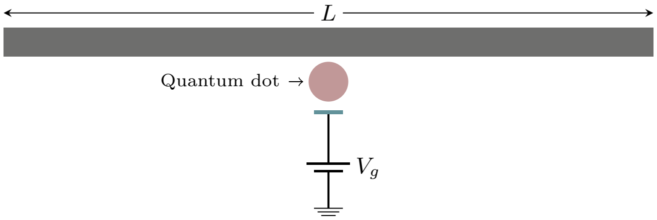

FIG. 1. Side-coupled device. The quantum wire contains an odd number L of sites. Electron tunneling is allowed between the quantum dot and the site at the center of the wire. The gate potential V_g controls the dot occupation.

The single-impurity Anderson model captures the essential physics of the device. A state d represents the quantum dot, and a conduction band, half-filled with noninteracting electrons, represents the quantum wire. The model Hamiltonian can be written in the form

$$H = H_{cb} + H_{\text{dot}} + H_{\text{dc}}. \tag{1}$$

Here the first, second, and third terms on the right-hand side represent the wire, the quantum dot, and the coupling between them.

Specifically, to describe the wire, we consider a lattice with L sites and the tight-binding Hamiltonian:

$$H_{cb} = -t \sum_{\ell \in \mathcal{L}} (c_\ell^\dagger c_{l+1} + \text{H.c.}), \tag{2}$$

where spin sums are implicit, a notation followed throughout the paper, and $\mathcal{L} = \{0, \pm 1, \dots, \pm (L-1)/2\}$.

The quantum dot is modeled by a single electronic orbital d, described by the Hamiltonian

$$H_{\text{dot}} = V_g \, \hat{n}_d + U n_{d\uparrow} n_{d\downarrow}, \tag{3}$$

where V_g is a gate potential, which controls the dot energy, and the term proportional to U accounts for the Coulomb repulsion between the electrons in the doubly occupied level.

The last term on the right-hand side of Eq. (1) is the coupling

$$H_{\text{dc}} = \mathcal{V}(d^\dagger c_0 + \text{H.c.}), \tag{4}$$

which models the tunneling between the dot orbital and the central wire site and hybridizes the dot with the conduction band.

The hybridization broadens the dot level to the width

$$\Gamma = \pi \rho \mathcal{V}^2, \tag{5}$$

where

$$\rho = \frac{1}{2\pi t} \tag{6}$$

is the per-particle density of states at the Fermi level.

A. Transformation to basis with well-defined parity

To simplify the numerical treatment of the model Hamiltonian, we exploit the left-right symmetry of the device in Fig. 1. H commutes with the parity operator Π, and its eigenstates can be classified by parity. The odd eigenstates are orthogonal to c_0, the site that is directly coupled to the dot, and are hence decoupled from the dot.

Specifically, it is convenient to define the even operators

$$a_0 \equiv c_0, \tag{7}$$

$$a_\ell \equiv \frac{c_\ell + c_{-\ell}}{\sqrt{2}} \quad (\ell = 1, \dots, \bar{L}), \tag{8}$$

where $\bar{L} \equiv (L-1)/2$, and the odd operators

$$b_\ell \equiv \frac{c_\ell - c_{-\ell}}{\sqrt{2}} \quad (\ell = 1, \dots, \bar{L}). \tag{9}$$

On the basis of the a_ℓ and b_ℓ, the Hamiltonian splits into an even and an odd term: $H = H_A + H_B$, where

$$H_A = -\sqrt{2}t(a_0^\dagger a_1 + \text{H.c.}) - t\sum_{\ell=1}^{\bar{L}}(a_\ell^\dagger a_{\ell+1} + \text{H.c.}) + H_{\text{dot}} + H_{\text{dc}} \tag{10}$$

and

$$H_B = -t\sum_{\ell=1}^{\bar{L}}(b_\ell^\dagger b_{\ell+1} + \text{H.c.}). \tag{11}$$

Since the quadratic form (11), which can be easily diagonalized, is completely decoupled from H_A, we will focus our attention on the latter Hamiltonian, henceforth.

B. Particle-hole transformation

The conduction-band Hamiltonian and the coupling between the conduction band and the quantum dot, that is, the sum of the first, second, and last terms on the right-hand side of Eq. (10), remain invariant under the particle-hole transformation

$$d \to -d^\dagger, \tag{12a}$$

$$a_\ell \to (-1)^\ell a_\ell^\dagger \quad (\ell = 0, \dots, \bar{L}). \tag{12b}$$

Application of (12) to the dot Hamiltonian H_{dot} yields the following expression:

$$\bar{H}_{\text{dot}} = -(U + V_g)\hat{n}_d + U n_{d\uparrow} n_{d\downarrow} + U + 2V_g. \tag{13}$$

The last two terms on the right-hand side constitute a constant, which merely redefines the energy zero. The particle-hole transformation maps H_A onto the conjugate Hamiltonian $\bar{H}_A$, with the same model parameters, except for the gate potential V_g, which undergoes the transformation

$$V_g \to -(U + V_g). \tag{14}$$

For $V_g = -U/2$ the two sides of (14) become equal. This parametric choice defines the (particle-hole) symmetric model Hamiltonian.

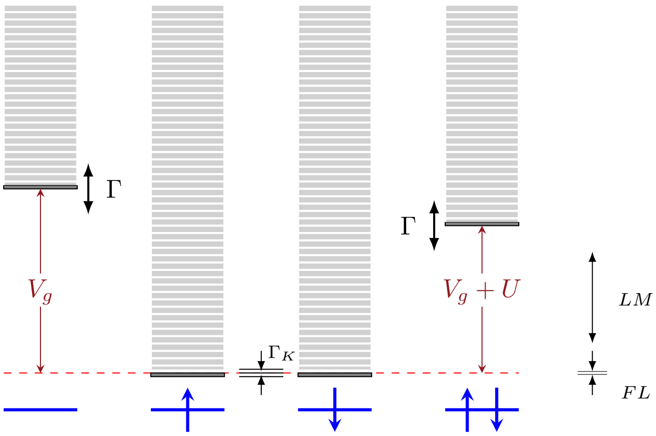

FIG. 2. Spectrum of the Anderson model near the symmetric point. With no hybridization ($\Gamma = 0$), the dot occupation n_d is conserved. The bold gray horizontal dashes represent the eigenvalues of the dot Hamiltonian, for the four configurations represented by the blue depictions at the bottom. The column with thin dashes above each dot energy represents conduction-band energies measured from the ground state. The tunneling amplitude broadens the dot level to a width Γ and hybridizes states in different columns. The arrows labeled *LM* and *FL* indicate fixed points of the renormalization group transformation defined in the text. The arrows labeled Γ_K define the low-energy region of the spectrum, in which the dot and conduction electrons lock into a Kondo singlet.

Figure 2 represents the $\Gamma \to 0$ spectrum of the model Hamiltonian in the vicinity of the symmetric point. The quantum dot is then decoupled from the conduction band, and the eigenvalues of the dot Hamiltonian (3) are $\mathcal{E}_0 = 0$, $\mathcal{E}_{1\uparrow} = \mathcal{E}_{1\downarrow} = V_g$, and $\mathcal{E}_2 = 2V_g + U$. Near particle-hole symmetry, as the dark bold boxes in the figure indicate, the lowest eigenvalue is degenerate, $\mathcal{E}_{\text{min}} = \mathcal{E}_{1\uparrow} = \mathcal{E}_{1\downarrow}$, and the energy differences are approximately equal:

$$\Delta_1 \equiv \mathcal{E}_0 - \mathcal{E}_1 = -V_g \tag{15}$$

and

$$\Delta_2 \equiv \mathcal{E}_2 - \mathcal{E}_1 = V_g + U. \tag{16}$$

With $\Gamma = 0$, each eigenstate of the model Hamiltonian is a combination of a many-body eigenstate of the conduction-band Hamiltonian with one of the four dot eigenstates, as indicated by the four stacks in the figure.

For $\max(\Delta_1, \Delta_2) \gg \Gamma > 0$, the coupling $\mathcal{V}$ hybridizes states in the inner stacks with outside states. The coupling breaks the degeneracy between the spin-1/2 states in the central columns to form a singlet ground state separated from a triplet state by an energy of $\mathcal{O}(\Gamma_K)$, where $\Gamma_K \equiv k_B T_K$ is the Kondo thermal energy. The hybridization between states in the two central stacks at energies $\epsilon \lesssim k_B T_K$ defines the Kondo resonance. For temperatures below the Kondo temperature, represented by the energy interval Γ_K in the figure, the conduction band electrons screen the singly occupied impurity, forming the Kondo singlet.

The eigenvalues ε of the Anderson Hamiltonian satisfying $\varepsilon < \Gamma_K$ are beyond the reach of perturbation theory. By contrast, the NRG describes accurately the entire spectrum of the Hamiltonian, including this low-temperature region [1].

III. MODIFIED NUMERICAL RENORMALIZATION GROUP METHOD

The NRG method provides an efficient nonperturbative solution to quantum impurity systems. Even though it is historically associated with the Kondo problem, its applications are more general. It can be applied to systems where a quantum mechanical impurity is coupled to a noninteracting bath of fermions or bosons [29]. There is extensive literature on NRG concepts [4], and numerical implementations [30]. For this reason, this section presents an overview of the method, focused on aspects that distinguish the two approaches.

A. NRG construction

While the odd term (11) of the model Hamiltonian can be diagonalized analytically, the even term (10) requires numerical treatment. Brute-force diagonalization is possible for small lattices. The dimension of the Fock space grows exponentially with L, however, and this approach soon becomes unfeasible.

Alternatives are offered by the NRG and the eNRG approaches. The latter retains basic features of the former. Cursorily described, the two methods rely on strictly controllable approximations that project the conduction-band Hamiltonian upon discrete bases. The resulting discrete Hamiltonians are tight-binding forms with position-dependent couplings and can be diagonalized iteratively with relatively small computational cost.

Notwithstanding the similarities, the two constructions are distinct. Brief recapitulation of the steps in Wilson's development seems therefore warranted, to facilitate comparison with the subsequent description of the real-space discretization.

1. Logarithmic discretization of the conduction band

The central approximation in the NRG procedure converts the conduction-band continuum to a logarithmic sequence of discrete levels. Specifically, Ref. [1] considered a band with uniform density of states $\bar{\rho}$, half-filled with noninteracting electrons. The band Hamiltonian describes a continuum of spin-degenerate states c_ϵ in the range $D \geqslant \epsilon \geqslant -D$:

$$H_0 = \int_{-D}^{D} \epsilon c_\epsilon^\dagger c_\epsilon \, d\epsilon. \tag{17}$$

The coupling between the impurity and the conduction band is given by the Hamiltonian

$$H_1 = \sqrt{2D}\mathcal{V}(c_d^\dagger \bar{f}_0 + \text{H.c.}), \tag{18}$$

where

$$\bar{f}_0 \equiv \sqrt{\frac{1}{2D}} \int_{-D}^{D} c_\epsilon \, d\epsilon. \tag{19}$$

The operator $\bar{f}_0$ defines a Wannier state with pivotal role in the NRG construction, because it controls the coupling between the conduction band and the impurity.

A dimensionless parameter $\Lambda > 1$ defines the discretization of H_0. Given Λ, the following expression introduces two infinite, discrete sequences of states:

$$a_{m\pm} \equiv \frac{1}{\mathcal{N}_m} \int_{\pm D\Lambda^{-m-1}}^{\pm D\Lambda^{-m}} c_\epsilon \, d\epsilon \quad (m = 0, 1, \ldots), \tag{20}$$

where $\mathcal{N}_m$ is a normalization factor.

The definition of the $a_{m\pm}$ offers an exact expression for the pivot:

$$\bar{f}_0 = \sqrt{\frac{1}{2D}} \sum_{m,\eta=\pm} \mathcal{N}_m a_{m\eta}. \tag{21}$$

The coupling between the dot level and the conduction states is not affected, therefore, by the discretization of the conduction band. This makes the NRG procedure uniformly accurate, for weak, moderate, or strong couplings.

While the coupling (18) can be faithfully described by the discrete operators, the conduction-band Hamiltonian cannot. The $a_{m\pm}$ constitute a basis that is incomplete relative to that of the c_ϵ. The substitution of the former basis for the latter is justified *a posteriori*, by the rapid convergence of computed physical properties to the continuum limit, as $\Lambda \to 1$ [1,2].

Projection of the conduction-band Hamiltonian upon the basis of discrete states, yields the approximate expression

$$H_0 = \sum_{m=0,\eta=\pm}^{\infty} \eta \mathcal{E}_m a_{m\eta}^\dagger a_{m\eta}, \tag{22}$$

with the discrete energies

$$\mathcal{E}_m = D\frac{1+\Lambda^{-1}}{2}\Lambda^{-m}. \tag{23}$$

2. Conversion to a tridiagonal basis

A Lanczos transformation starting with the operator $\bar{f}_0$ in Eq. (19) next converts the conduction-band Hamiltonian to the tridiagonal form

$$H_0 = \sum_{n=0}^{\infty} \bar{t}_n (\bar{f}_n^\dagger \bar{f}_{n+1} + \text{H.c.}), \tag{24}$$

where the $\bar{f}_n$ are normalized Fermi operators, and the codiagonal coefficients have the expression

$$\bar{t}_n = D\frac{1+\Lambda^{-1}}{2} \frac{1-\Lambda^{-n-1}}{\sqrt{1-\Lambda^{-2n-1}}\sqrt{1-\Lambda^{-2n-3}}} \Lambda^{-n/2}. \tag{25}$$

For large n the coefficients are accurately described by the simpler form

$$\bar{t}_n = D\frac{1+\Lambda^{-1}}{2}\Lambda^{-n/2} \quad (\Lambda^{-n} \ll 1). \tag{26}$$

The $\bar{f}_n$ basis is complete with respect to the basis of the a_m. The only approximation in the derivation of Eq. (24) is, therefore, the projection of the conduction-band Hamiltonian upon the basis of the a_m. The parameter Λ controls the accuracy of this approximation.

3. Renormalization of coupling constants

To accelerate convergence to the continuum limit, it proved necessary to renormalize the model parameters [3]. Each operator $\bar{f}_0$ or $\bar{f}_0^\dagger$ in a model Hamiltonian must be multiplied by a dimensionless factor $\sqrt{A_\Lambda}$, where

$$A_\Lambda = \frac{1+\Lambda^{-1}}{1-\Lambda^{-1}} \ln\sqrt{\Lambda} \tag{27}$$

converges rapidly to unity as $\Lambda \to 1$.

This upscaling is necessary because the discretization reduces the $\bar{f}_0$ spectral density by a factor A_Λ. This renormalization suffices to correct the procedure for model Hamiltonians with energy-independent impurity-band couplings, such as (18). Energy-dependent couplings, such as those in the two-impurity Anderson Hamiltonian, call for a modified discretization procedure [31].

B. Real-space approach

As explained in the introduction, the real-space discretization procedure shares with traditional NRG the initial goal of reducing the conduction band Hamiltonian to a tridiagonal form with progressively smaller off-diagonal coefficients. The starting point, instead of Eq. (17), is the tight-binding Hamiltonian on the right-hand side of Eq. (10):

$$H_{cb} = -\sqrt{2}t(a_0^\dagger a_1 + \text{H.c.}) - t\sum_{\ell=1}^{\bar{L}}(a_l^\dagger a_{\ell+1} + \text{H.c.}), \tag{28}$$

with $\bar{L} \to \infty$, which defines the continuum limit.

1. Overview

Before turning to the new procedure, it seems appropriate to discuss general aspects of discretization in momentum and real space comparatively. The conduction-band energies in Eq. (17) form a continuum ranging from $\epsilon = -D$ to $\epsilon = D$. Numerical treatment calls for discretization, to reduce the multiplicity of energy levels to a finite number. The simplest form is linear discretization, which splits the band into $2N$ identical intervals of width D/N each, where N is an arbitrary positive integer. A single operator is then defined as a linear combination of the c_ϵ within each interval. If the conduction band is coupled to a quantum dot, the linear combinations are designed to reproduce the coupling accurately.

The linear discretization gives rise to a potentially serious problem. In the original conduction band, particle-hole excitations are possible, across the Fermi level. If the energy of one such excitation is $\mathcal{E}$, given a dimensionless constant $\Lambda > 1$, one can always find other excitations with the smaller energies $\mathcal{E}/\Lambda, \mathcal{E}/\Lambda^2, \ldots$ The region of the conduction band centered at the Fermi level and close to it remains invariant under the scaling transformation $\mathcal{E} \to \Lambda\mathcal{E}$, a property whose significance was highlighted by Wilson [1].

The linear discretization breaks the invariance, because the mininum excitation energy in the spectrum of the discrete Hamiltonian is $\delta\mathcal{E} = D/N$. If the energy scale of interest is comparable to, or smaller than $\delta\mathcal{E}$, calculations of physical properties on the basis of linear discretizations will yield unreliable results. In an attempt to reduce $\delta\mathcal{E}$, one might argue that the high-energy degrees of freedom in the conduction band lie outside the range of interest and substitute a smaller energy, say $D' = D/100$, for the original half bandwidth.

This crude ultraviolet truncation is a very poor approximation, however, since the quantum dot effectively couples the high-energy degrees of freedom to the ones with low energy. Under such conditions, perturbation theory recommends treating the high-energy scales accurately before turning to the low-energy spectrum. In line with this prescription, Anderson's poor man's scaling defines a refined ultraviolet truncation [32]; unfortunately, that perturbative treatment breaks down before the bandwidth can be sufficiently reduced. Wilson therefore introduced the breakthrough summarized in Sec. III A: instead of a linear mesh, Ref. [1] employed the logarithmic mesh in Eq. (20), which preserves invariance under energy-scaling by powers of Λ.

Consider now the tight-binding Hamiltonian (28). Even though the lattice comprises discrete sites, the spectrum of the $\bar{L} \to \infty$ Hamiltonian constitutes a continuum ranging from $\epsilon = -2t$ to $\epsilon = 2t$. To discuss the scaling properties of the continuum, it is convenient to examine the wave vectors k, instead of the energies ϵ_k. Let a denote the lattice spacing. The allowed wave vectors then form a Brillouin Zone continuum ranging from $-\pi/a$ to π/a. Given an excitation of wave vector k in the spectrum of the conduction-band Hamiltonian, there will also be excitations with momenta $k/\lambda, k/\lambda^2, \ldots$, where $\lambda > 1$ is an arbitrary constant. The Hamiltonian is invariant under wave-vector transformations $k \to k/\lambda$.

Numerical treatment of the conduction-band Hamiltonian demands reduction of the number of sites to a manageable integer. The simplest expedient is to truncate the chain, from size $\bar{L} \to \infty$ to a small size L. This reduction is equivalent to linear discretization in energy space, and incurs the same limitation. Namely, the shortening from $\bar{L}$ to L is a rudimentary infrared truncation, which introduces the artificial wave-vector scale $k_{\min} = \pi/L$ and eliminates the small wave vectors, with $|k| < k_{\min}$, from the spectrum of the Hamiltonian. The inevitable result is poor description of physical properties at low energies.

An alternative procedure, one that deals well with small momenta while reducing the computational cost of diagonalizing the Hamiltonian is readily available. Instead of truncating the lattice size $\bar{L}$, one could keep $\bar{L}$ fixed and split the lattice into cells of size Na, containing a large, fixed number N of lattice points. All the degrees of freedom within each cell would then be lumped into a single Fermi operator, defined as a linear combination of the N operators c_ℓ associated with the cell sites. With the size of the lattice unchanged, the smallest k would be preserved in the resulting coarse-grained conduction-band Hamiltonian. In the opposite extreme, however, the largest allowed momentum would be $k_{\max} = 1/(Na)$, and the largest conduction energy would be $\epsilon_{k_{\max}} \approx 4t/N$. Coarse graining is hence akin to the above-described rough ultraviolet truncation and inherits the shortcomings of that simple-minded approximation.

Clearly, to ensure accuracy, numerical treatment of the tight-binding Hamiltonian demands a special construction to overcome the difficulties facing the crude ultraviolet and infrared truncations. The construction must preserve (i) the scale of the largest wave vectors in the Brillouin Zone, and (ii) wave-vector-scaling invariance, while thinning out the conduction-band degrees of freedom. To achieve this, Sec. III B chooses a natural number λ and defines an infinite sequence of cell sizes. To preserve the largest wave vectors, the sequence starts out with the size of the primitive cell. To preserve scale invariance, it grows geometrically. Accordingly, if a cell of size ℓ belongs to the sequence, for which the minimum wave vector is $k_{\text{min}} = \pi/\ell$, so do the cells with sizes $\lambda\ell, \lambda^2\ell, \ldots$, for which the minimum wave vectors are $\pi/(\lambda\ell), \pi/(\lambda^2\ell), \ldots$. Wave-vector invariance is hence saved, even though it is preserved in a restricted sense, just as the invariance of energies in the logarithmic sequence (23) is restricted to powers of Λ.

2. Discretization

The eigenvalues of the tight-binding Hamiltonian span the interval $-2t \leqslant \epsilon \leqslant 2t$. The discretization of this spectrum is parametrized by two natural numbers: the *offset* $\zeta \geqslant 0$, and the *common ratio* λ. The offset is a site index that divides the lattice into two complementary regions: the first one comprises all sites to the left of site ζ; the second comprises the remaining sites. The discretization leaves intact those terms in the Hamiltonian associated with the first set, but affects those associated with the second set.

More specifically, the offset splits the right-hand side of Eq. (28) into two tight-binding Hamiltonians:

$$H_{cb} = H_a + H_f, \tag{29}$$

where H_a comprises the first ζ sites plus the coupling to site ζ:

$$H_a \equiv -t\left(\sqrt{2}a_0^\dagger a_1 + \sum_{\ell=1}^{\zeta-1} a_\ell^\dagger a_{\ell+1} + \text{H.c.}\right) \tag{30}$$

and H_f comprises the remaining sites

$$H_f \equiv -t\sum_{\ell=\zeta}^{\bar{L}}(a_\ell^\dagger a_{\ell+1} + \text{H.c.}). \tag{31}$$

The common ratio λ defines a new basis comprising an infinite set of Fermi operators f_n $(n = 0, 1, 2, \ldots)$, to replace the operators a_ℓ $(\ell = \zeta, \ldots, \bar{L})$. As Fig. 3 indicates, the definition starts out with an infinite sequence of cells $\mathcal{C}_n$ $(n = 0, 1, \ldots)$. The first cell contains only one lattice site: $j = \zeta$. The second comprises λ sites, from $\ell = \zeta + 1$ to $\ell = \zeta + \lambda$.

The nth cell covers λ^n sites and extends from $\ell = \zeta + \mathcal{G}_n$ to $\ell = \zeta + \mathcal{G}_n + \lambda^n$, where

$$\mathcal{G}_n \equiv \frac{\lambda^n - 1}{\lambda - 1} \tag{32}$$

is the geometric series with common ratio λ.

With $\lambda = 1$, each cell reduces to a single site, and we recover the continuum limit. With $\lambda > 1$, the number of sites in cell $\mathcal{C}_n$ grows exponentially with n. It is then convenient to let $a_{n,j}$ denote the Fermi operator associated with the jth site in cell $\mathcal{C}_n$ $(j = 1, \ldots, \lambda^n; n = 0, 1, \ldots)$, to avoid the cumbersome indexing $a_{\zeta+\mathcal{G}_n+j-1}$.

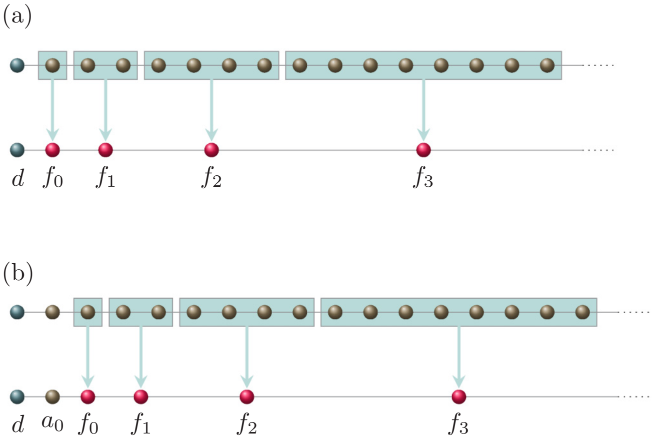

FIG. 3. Real-space geometry guiding the discretization of the conduction band, for *common ratio* $\lambda = 2$. The darker spheres at the top of each panel represent the dot and the wire lattice. The lattice sites are grouped into cells of exponentially increasing size. For each cell, Eq. (33) defines a linear combination f_n $(n = 0, 1, \ldots)$ of the wire states. The linear combinations form a basis $\{f_n\}$ upon which the conduction-band Hamiltonian is projected. The *offset* ζ specifies the position of the first cell. To illustrate, panels (a) and (b) depict the constructions for $\zeta = 0$ and $\zeta = 1$, respectively.

A normalized linear combination f_n of the operators $a_{n,\ell}$ in cell $\mathcal{C}_n$ can now be defined:

$$f_n \equiv \sum_{j=1}^{\lambda^n} \alpha_{n,j} a_{n,j} \quad (n = 0, 1, \ldots), \tag{33}$$

with complex coefficients

$$\alpha_{n,j} = |\alpha_{n,j}| \exp(i\phi_{n,j}), \tag{34}$$

which must satisfy the normalization condition:

$$\sum_{j=1}^{\lambda^n} |\alpha_{n,j}|^2 = 1. \tag{35}$$

The definition (33) makes the operators f_n $(n = 0, 1, \ldots)$ mutually orthogonal. The f_n form a basis that is incomplete with respect to the space spanned by the $a_{n,j}$ $(n = 0, 1, \ldots; j = 1, 2, \ldots, \lambda^n)$. The incompleteness notwithstanding, following traditional NRG reasoning we will project the conduction-band Hamiltonian onto the basis of the operators $d, a_0, \ldots, a_{\zeta-1}, f_0, \ldots, f_{N-1}$. This approximation is justified *a posteriori*, by the rapid convergence of physical properties to those of the $\lambda = 1$ Hamiltonian.

Explicitly, the approximation amounts to treating Eq. (33) as an orthonormal transformation, the inversion of which yields the expression

$$a_{n,j} = \alpha_{n,j}^* f_n \quad (n = 0, 1, \ldots; j = 1, 2, \ldots, \lambda^n). \tag{36}$$

Substitution of the right-hand side of Eq. (36) for the a_ℓ expresses the Hamiltonian (31) on the basis of the operators

f_n $(n = 0, 1, \dots)$:

$$H_{f\lambda} \equiv -t \sum_{n=1}^{\infty} \sum_{j=1}^{\lambda^n - 1} (\alpha_{n,j}\alpha^*_{n,j+1} + \text{c.c.}) f_n^\dagger f_n - t \sum_{n=0}^{\infty} (\alpha_{n,\lambda^n}\, \alpha^*_{n+1,1}\, f_n^\dagger f_{n+1} + \text{H.c.}). \tag{37}$$

The first term on the right-hand side in Eq. (37) is at odds with Eq. (31), which contains no diagonal terms. Judicious choice of the phases $\phi_{n,j}$ is necessary and sufficient to eliminate this discrepancy. Appendix A shows that the definition

$$\phi_{n,j} = \frac{\pi}{2}(\mathcal{G}_n + n + j) \tag{38}$$

reduces Eq. (37) to the equality

$$H_{f\lambda} = t \sum_{n=0}^{\infty} (|\alpha_{n,\lambda^n}|\, |\alpha_{n+1,1}|\, f_n^\dagger f_{n+1} + \text{H.c.}). \tag{39}$$

The absolute values $|\alpha_{n,j=\lambda^n}|$ and $|\alpha_{n+1,1}|$ $(n = 0, 1, \dots)$ must be specified before the sum on the right-hand side of Eq. (39) can be computed. More generally, absolute values $|\alpha_{n,j}|$ $(n = 0, 1, \dots;\ j = 1, \dots, \lambda^n)$ satisfying the normalization condition (35) must be specified. Out of the infinite set of alternatives—Appendix B 1 discusses a few—we pick the one that is physically most satisfactory: given the equivalence among lattice sites in the tight-binding lattice, we attribute equal weights to the sites in each cell. Explicitly, within cell $\mathcal{C}_n$ let

$$|\alpha_{n,j}| = \alpha_n \quad (j = 1, \dots, \lambda^n), \tag{40}$$

where α_n is a positive constant, independent of j.

It then follows from the normalization condition that

$$|\alpha_{n,j}| = \lambda^{-\frac{n}{2}}, \tag{41}$$

an equality that turns Eq. (39) into an expression similar to Eq. (24):

$$H_{f\lambda} = \sum_{n=0}^{\infty} (t_n f_n^\dagger f_{n+1} + \text{H.c.}), \tag{42}$$

where

$$t_n = t\lambda^{-n-\frac{1}{2}} \quad (n > 0). \tag{43}$$

The proviso $n > 0$ in Eq. (43) is necessary because t_0 takes a special value if $\zeta = 0$. In that case, the operator f_0 coincides with a_0, and the coupling between a_ζ and $a_{\zeta+1}$ on the right-hand side of Eq. (30) is $-\sqrt{2}t$, not $-t$. Hence

$$t_0 = \begin{cases} \sqrt{2}t\lambda^{-\frac{1}{2}} & (\zeta = 0) \\ t\lambda^{-\frac{1}{2}} & (\zeta > 0) \end{cases}. \tag{44}$$

Comparison between Eqs. (26) and (43) shows that, for n such that $\Lambda^{-n} \ll 1$, the identification $\Lambda = \lambda^2$ brings the NRG codiagonal coefficients $\bar{t}_n$ and the eNRG coefficients t_n into agreement, except for the constant prefactors $(1 + \Lambda^{-1})/2$ and $\lambda^{-1/2}$. Although distinct, the two factors are approximately equal: they approach unity as $\Lambda, \lambda \to 1$ and differ by less than 15% for discretization parameters as large as $\Lambda = \lambda^2 = 25$.

Substitution of $H_{f\lambda}$ for H_f yields a discretized approximation to the Hamiltonian H_A. Equation (10) becomes

$$H_{A\lambda} = -t\left(\sqrt{2}a_0^\dagger a_1 + \sum_{\ell=1}^{\zeta-1} a_\ell^\dagger a_{\ell+1} + a_\zeta^\dagger f_0 + \text{H.c.}\right) + H_{f\lambda} + H_{\text{dot}} + H_{\text{dc}}. \tag{45}$$

The real-space construction can be regarded as a decimation procedure that spares sites closest to the quantum dot but becomes rapaciously more inclusive as the distance from the dot grows. The offset controls the size of the region in which all sites are spared and hence controls the eNRG resolution in the vicinity of the quantum dot. Larger ζ offer more detailed description of the couplings.

Consider, for example, a quantum dot that is coupled to the central lattice site and to its nearest neighbors. The couplings are then described by the Hamiltonian

$$H'_{dc} = (\mathcal{V} d^\dagger a_0 + \mathcal{V}_1 d^\dagger a_1 + \text{H.c.}), \tag{46}$$

instead of H_{dc}.

If $\zeta = 0$, the nearest neighbor will be one of two sites in cell $\mathcal{C}_1$. The term $\mathcal{V}_1(d^\dagger a_1 + \text{H.c.})$ will therefore be only approximately represented by the $\{f_n\}$ basis, and the accuracy of the computation will depend on $\mathcal{V}_1$.

The offset should instead be set to $\zeta = 1$ or larger. With $\zeta = 1$, the operator a_1 will coincide with f_0 and the Hamiltonian H'_{dc} will be exactly described on the basis of the f_n.

Another aspect of this example deserves brief discussion. The addition of a coupling $(\mathcal{V}_1 d^\dagger a_1 + \text{H.c.})$ to the Hamiltonian (1) introduces only irrelevant operators, which affect such nonuniversal features of the single-impurity Anderson model as the Kondo temperature or the ground-state phase shift, but not its universal properties [2]. This addition may break particle-hole symmetry, however, as one can check by applying transformation (12) to Eq. (46). Given that the physical properties of more complex Hamiltonians may depend critically on its symmetry [33], we can see that accurate description of the couplings to the wire may be necessary. Under these circumstances, the spatial resolution of the eNRG approach will be a valuable asset.

3. Truncation

Equation (42) is closely analogous to the equality defining the logarithmically discretized conduction-band Hamiltonian in the standard NRG method. This allows us to follow the truncation and iterative diagonalization procedure described in Ref. [2].

The exponential decay on the right-hand side of Eq. (26) allows definition of a renormalization group transformation [1]. To this end, consider an energy $\mathcal{E}$, representative of an energy scale of interest, and a dimensionless *infrared-truncation* parameter $\gamma \ll 1$. One can then identify the smallest integer $\mathcal{N}$ satisfying the inequality

$$t\lambda^{-\mathcal{N}} < \gamma\mathcal{E}. \tag{47}$$

Substitution of $\mathcal{N}-1$ for the upper limit of the sum then reduces the right-hand side of Eq. (42) to a finite series:

$$H_{f\lambda} = \sum_{n=0}^{\mathcal{N}-1} t_n (f_n^\dagger f_{n+1} + \mathrm{H.c.}). \tag{48}$$

The inequality (47) controls the accuracy of this approximation. In the limit $\gamma \to 0$, Eq. (48) becomes equivalent to Eq. (42).

The right-hand side of Eq. (48) can now be substituted for $H_{f\lambda}$ on the right-hand side of Eq. (45). Next, the resulting finite series is scaled up by the factor $1/t_{\mathcal{N}-1} \equiv \lambda^{N-1/2}/t$, which yields the dimensionless, truncated Hamiltonian $H_{\mathcal{N}}$:

$$t_{\mathcal{N}-1} H_{\mathcal{N}} = H_{\mathrm{dot}} + H_{\mathrm{dc}} + \sum_{n=0}^{\mathcal{N}-1} t_n (f_n^\dagger f_{n+1} + \mathrm{H.c.}) - t\left(\sqrt{2}a_0^\dagger a_1 + \sum_{\ell=1}^{\zeta-1} a_\ell^\dagger a_{\ell+1} + a_{\zeta-1}^\dagger f_0 + \mathrm{H.c.}\right). \tag{49}$$

4. Renormalization group transformation and iterative diagonalization

The truncation of the infinite series in the model Hamiltonian has practical and conceptual implications. From the practical perspective, the truncation is valuable because it allows iterative diagonalization of the Hamiltonian, a procedure detailed in Ref. [30]. At iteration $\mathcal{N}$ ($n = 0, 1, \ldots$), the diagonalization determines all the eigenvalues of $H_{\mathcal{N}}$ below the *ultraviolet cutoff* E_{UV}, a dimensionless parameter that controls the cost and the scope of the diagonalization procedure. In addition, it gives access to the matrix elements of the Fermi operators a_ℓ ($\ell = 0, \ldots, \zeta - 1$) and f_n ($n = 0, \ldots, \mathcal{N}$) between pairs of eigenvectors associated with the computed eigenvalues; the effort necessary to determine such matrix elements is small in comparison with the computational cost of diagonalizing the Hamiltonian.

Conceptually, Eq. (49) is important because it defines the mapping $\tau[H_{\mathcal{N}}] = H_{\mathcal{N}+1}$, which adds a smaller energy scale to $H_{\mathcal{N}}$ and rescales the result so that the resulting smallest eigenvalue be of $\mathcal{O}(1)$. The mapping is, therefore, a renormalization group transformation. From Eq. (49), it follows that

$$\tau[H_{\mathcal{N}}] = \lambda H_{\mathcal{N}} + (f_{\mathcal{N}}^\dagger f_{\mathcal{N}+1} + \mathrm{H.c.}). \tag{50}$$

With the substitution $\lambda \to \Lambda^{1/2}$, Eq. (50) reproduces the large-N limit of the NRG transformation [2].

5. Fixed points

As first discussed in Ref. [2], for special combinations of the model parameters the Hamiltonian $H_{\mathcal{N}}$ is a fixed point of the renormalization group transformation τ^2. Consider, for example, the symmetric model. Given an energy $\mathcal{E}$, Eq. (47) determines the corresponding truncation number $\mathcal{N}$. At moderately high energies $\mathcal{E}$, such that $t \gg \mathcal{E} \gg U$, the eigenvalues of the truncated Hamiltonian (49) are approximately equal to the eigenvalues of the *free-orbital* fixed-point H_{FO}^* which is the $U = V_g = \Gamma = 0$ limit of the model Hamiltonian, that is, the sum of the last two terms on the right-hand side of Eq. (49).

Likewise, for energies in the range $U \gg \mathcal{E} \gg k_B T_K$, the eigenvalues of $H_{\mathcal{N}}$ are approximately equal to the eigenvalues of the *symmetric local-moment* fixed-point Hamiltonian. The local-moment Hamiltonian is the $-V_g/2 = U \to \infty$, $\Gamma = 0$ limit of the truncated Hamiltonian.

Finally, for energies $\mathcal{E}$ well below the Kondo energy $k_B T_K$, the eigenvalues of $H_{\mathcal{N}}$ approach those of the *symmetric frozen-level* fixed-point Hamiltonian. The latter is the $-V_g = U = 0$, $\Gamma \to \infty$ limit of $H_{\mathcal{N}}$.

The scope of the eNRG method is by no means restricted to particle-hole symmetric models. Below, we will consider, Hamiltonians with $-V_g/2 \gtrsim U \gg \Gamma$. At high energies, with $\mathcal{E} > -V_g/2$, the asymmetry is unimportant, and the truncated Hamiltonian again approaches the free-orbital fixed point H_{FO}^*. At lower energies, however, instead of the symmetric local-moment fixed point, the truncated Hamiltonian approaches a fixed point on the *local-moment line* of fixed points $\mathcal{H}_{\mathrm{LM},\bar{\delta}}^*$. At still lower energies, such that $k_B T_K \gg \mathcal{E}$ the truncated Hamiltonian approaches a stable fixed point on the *frozen-level line* of fixed points $\mathcal{H}_{\mathrm{FL},\delta}^*$.

The vertical arrows labeled FO, LM, and FL at the extreme right in Fig. 2 indicate the energy ranges in which the spectrum of the model Hamiltonian is close to the free-orbital (FO) fixed point, a point on the local-moment (LM) line or a point on the frozen-level (FL) line. Near the FO, since thermal or excitation energies are higher than the dot energies, the dot orbital is equivalent to a zero-energy level decoupled from the conduction band. Near the LM, as Fig. 2 indicates, the relatively small excitation energies freeze-out the vacant and the doubly occupied dot-orbital configurations, and the dot acquires a local moment. Since excitation energies are larger than the energy scale $k_B T_K$, at the LM fixed point the dot moment is free from screening.

As the energy is reduced, the spectrum of the Hamiltonian moves away from the LM structure, towards the FL structure. For energies much smaller than the Kondo thermal energy, the dot moment is completely screened, and the spectrum approaches the FL.

Each local-moment fixed point is equivalent to a phase-shifted conduction band decoupled from a spin-1/2 variable $\vec{S}$ and is described by the truncated Hamiltonian

$$\mathcal{H}_{\mathrm{LM},\bar{\delta}}^* = \frac{1}{t_{\mathcal{N}-1}}\left(\sum_{n=0}^{\mathcal{N}-1} t_n (f_n^\dagger f_{n+1} + \mathrm{H.c.}) + \bar{W} f_0^\dagger f_0\right), \tag{51}$$

where the scattering potential $\bar{W}$ depends on the model parameters U, V_g, and V; for $V_g = -U/2$, in particular, particle-hole symmetry allows only two potentials: $\bar{W} = 0$ or $\bar{W} = \infty$.

The quadratic form on the right-hand side of Eq. (51) can be diagonalized analytically [3]. For definiteness, let $\mathcal{N}$ be odd. Then, there are $M \equiv (\mathcal{N}+1)/2$ positive eigenvalues $\bar{\varepsilon}_{\ell+}$ and M negative eigenvalues $\bar{\varepsilon}_{\ell-}$, approximately given by the expressions

$$\bar{\varepsilon}_{\ell\pm} = \pm\lambda^{2(\ell\mp\frac{\bar{\delta}}{\pi})} \quad \left(\ell = 0, 1, \ldots, \frac{\mathcal{N}+1}{2}\right), \tag{52}$$

with phase shifts $\bar{\delta}$ determined by the scattering potential $\bar{W}$ on the right-hand side of Eq. (51):

$$\bar{\delta} = -\arctan(\pi\rho\bar{W}). \tag{53}$$

The phase shifts are defined mod π, in the interval $-\pi/2 < \bar{\delta} \leqslant \pi/2$.

Projected onto the basis of its eigenvectors g_ℓ, the fixed-point Hamiltonian reads

$$\mathcal{H}^*_{\mathrm{LM},\bar{\delta}} = \sum_{\ell,\alpha=\pm} \bar{\varepsilon}_{\ell\alpha} g^\dagger_{\ell\alpha} g_{\ell\alpha}. \tag{54}$$

The FL fixed points are equivalent to phase-shifted conduction bands, described by a Hamiltonian analogous to Eq. (51):

$$\mathcal{H}^*_{\mathrm{FL},\delta} = \frac{1}{t_{N-1}}\left(\sum_{n=0}^{\mathcal{N}-1} t_n (f^\dagger_n f_{n+1} + \mathrm{H.c.}) + W f^\dagger_0 f_0\right). \tag{55}$$

The right-hand sides of Eq. (55) and (51) have the same form. The eigenvalues of $\mathcal{H}^*_{\mathrm{FL},\delta}$ are therefore described by an approximate equality analogous to Eq. (52):

$$\varepsilon_{\ell\pm} = \pm\lambda^{2(\ell\mp\frac{\delta}{\pi})} \quad \left(\ell = 0, 1, \ldots, \frac{\mathcal{N}+1}{2}\right), \tag{56}$$

where

$$\delta = -\arctan(\pi\rho W). \tag{57}$$

Given that the spin of one electron is required to screen the dot moment, the Friedel sum rule ties the two phase shifts [34]:

$$\delta = \bar{\delta} - \frac{\pi}{2}. \tag{58}$$

A scattering potential $\bar{W} \neq 0$ breaks particle-hole symmetry. For the symmetric model, therefore, $\bar{\delta} = 0$ and the frozen-level phase shift is $\delta = \pi/2$.

IV. COMPARISON BETWEEN THE ENRG AND NRG PROCEDURES

As the similarity between Eqs. (24) and (42) suggests, the concepts and mathematical expressions in Secs. III B 3–III B 5 are equivalent to the notions and equations underlying the NRG formalism. As illustrated by the analysis and computations in Secs. IV B 3 and IV B 4, respectively, application of the two methods to simple Hamiltonians yields essentially the same physical properties at low temperatures, such that k_BT be small compared to the bandwidth. At higher temperatures, as the data in Sec. IV B 1 show, eNRG yields more accurate results, even when applied to an elementary device. Section IV A 2 discusses a slightly more elaborate geometry, with two quantum dots, to show that the real-space treatment ensures exact mathematical description of the dot-wire couplings onto the discretized basis, while standard NRG projection offers an approximate description that renders the accuracy of the procedure model-parameter dependent.

The NRG discretization can be tailored to the requirements of the geometry. As an example, Sec. IV A 4 details a generalization allowing for offsets equivalent to those defined by the eNRG parameter ζ. While the introduction of an offset in the eNRG procedure is straightforward—a natural extension—, the modification of the NRG discretization calls for a number of transformations. Analogous considerations apply to the two-dot system or other, more complex configurations. The eNRG constructions are simpler because devices are designed in real space, a point the following subsections substantiate.

A. General aspects

We first present general arguments pondering the advantages and shortcomings of the eNRG method against the NRG procedure.

1. Operational aspects

From the operational viewpoint, the eNRG and the NRG algorithms runs on parallel tracks. The codiagonal coefficients in the NRG Hamiltonian obey Eq. (25), while the eNRG Hamiltonian follows Eq. (43), but the iterative diagonalizations are otherwise identical. The parameters Λ, in the former equality, λ and ζ, in the latter, and the ultraviolet cutoff E_{uv} primarily determine the computational cost and accuracy of the diagonalizations. The computational costs of diagonalizing the eNRG and the NRG Hamiltonians are practically identical. For the symmetric model with Coulomb repulsion $U = t$ and dot-level width $\Gamma = 0.4t$, for instance, a standard laptop computer running code written in C++ executes full runs of the NRG procedure with $\Lambda = 4$ and $E_{\mathrm{uv}} = 40t$, and of the eNRG procedure with $\lambda = 2$, $E_{\mathrm{uv}} = 40t$, and $\zeta = 1$, yielding all three energy moments $\mathcal{L}_j$ $(j = 0, 1, 2)$ with less than 1% deviation at any temperature in CPU times of approximately 140 s. Our PYTHON code executes the same computation in roughly 500 s. With regard to computational cost, the eNRG and NRG procedures are equivalent.

As discussed in Sec. IV A 5, below, an extension of the NRG method has introduced a second discretization parameter z, an arbitrary real number in the interval $0.5 < z \leqslant 1.5$, so that the z-dependent eigenvalues of the discretized conduction-band Hamiltonian scan the entire conduction band as z runs from the lower to the upper limit of the interval [35,36]. Averaging over z eliminates the conspicuous artificial oscillations resulting from the computation of thermodynamical or transport properties as functions of the temperature for $\Lambda > 2$, and gives access to equilibrium excitation properties [37].

To a certain extent, the eNRG offset parameter ζ mimics the NRG parameter z. As Appendix B 5 shows, $\zeta = 0$ corresponds to $z = 1$, while $\zeta = 1$ corresponds to $z = 0.5$. The correspondence is not complete, however, because the definition of the offset restrains ζ to the set of integer numbers. This is a serious limitation, because differentiation with respect to z plays an important role in the computation of excitation properties [37]. Appendix B 5 therefore introduces a third discretization parameter w, which is in closer correspondence to the NRG parameter z since (i) averaging of the eNRG data over w eliminates artificial oscillations, much like averaging of NRG data over z eliminates the equivalent oscillations in NRG computations, and (ii) the definition of the w can be extended to the set of real numbers.

Another apparent limitation of the eNRG procedure is the definition of the discretization parameter λ, which is also restrained to the set of natural numbers. Even though it constitutes no serious shortcoming, since the choice $\lambda = 2$ offers an adequate compromise between accuracy and computational cost, this limitation may be removed. A mathematical proof appears in Appendix B 6, which shows that the domain can be extended to $\lambda \in \mathbb{R}$.

The formal constraints binding the eNRG parameters to the set of natural numbers and appearing to make the new construction narrower than the NRG formalism are therefore easily removed. On the other hand, more general considerations favor the eNRG approach. The combination of logarithmic discretization with Lanczos transformation at the foundation of the NRG method is more involved than the discretization in Sec. III B 2, even when one disconsiders the amendment delineated in Sec. III A 3. More importantly, the simplicity of the eNRG approach eases treatment of more demanding models, as the following discussion shows.

2. *Two-dot problem*

Consider, for example, a straighforward generalization of the device in Fig. 1, with two quantum dots coupled to the quantum wire at sites separated by a distance 2ℓ. The physics of this system is equivalent to that of the three-dimensional two-impurity Kondo problem, which has been brought to light by a combination of analytical, Monte Carlo, and NRG studies [28,38–44]. In brief, the RKKY interaction $\mathcal{I}$ between the impurities competes with Kondo thermal energy k_BT_K. The ratio $\mathcal{I}/k_BT_K$ parametrizes the physical properties and defines a ferromagnetic RKKY regime, an antiferromagnetic RKKY regime, and a Kondo regime. The NRG approach yields accurate Kondo temperatures. The computed $\mathcal{I}$ are less reliable, nonetheless. The innacuracy can be traced to the irrelevant operators that the logarithmic discretization of the conduction band introduces. Those operators make contributions of $\mathcal{O}(\epsilon/D)$. Since a substantial part of the RKKY interaction comes from conduction states with energies comparable to the bandwidth, the operators artificially introduced by the discretization limit the accuracy of the ratios $\mathcal{I}/k_BT_K$ in NRG computations.

3. *Control over high-energy artifacts of discretization*

The eNRG discretization is likewise the source of irrelevant operators. Nevertheless, one can easily control the resulting inaccuracies. Speficially, the irrelevant operators shrink as the offset ζ grows. To exhibit concrete evidence, Sec. IV B 1 will compare two computations of the temperature-dependent conductance through the device in Fig. 1, a standard NRG calculation compared with the equivalent eNRG calculation with $\zeta = 3$. At low temperatures, for thermal energies that are much smaller than the bandwidth, the results are virtually identical. At higher temperatures, however, the NRG conductances show deviations from the continuum limit, while the eNRG results are accurate. Equally precise estimates of the RKKY interaction can be expected from eNRG computations.

The cost of computation grows rapidly with ζ. The growth is by no means unmanageable, however, given that $\zeta = 3$ is sufficient to describe physical properties accurately at energies comparable to the bandwidth. Table I displays the computational times needed to calculate the thermal dependence of the conductance, with the Python code, for the model parameters $U = 10\,D$, $V_g = -U/2$, and $\Gamma = 0.04\,U$, and the indicated offsets. In each run, the ultraviolet cutoff $E_{\rm uv}$ was chosen to yield an average relative deviation $\langle\Delta\rangle$ close to 0.4%. Here, the deviation Δ is defined as the difference between the conductances at the same temperature calculated at two successive iterations $\mathcal{N}$ and $\mathcal{N}+1$ of the diagonalization procedure. Since the average deviation tends to rise with ζ, the ultraviolet cutoff had to be increased as the offset grew, which raised the computational time. The first tabulated CPU time lies outside this trend because the leading codiagonal coefficient t_0 is reduced from $\sqrt{2/\lambda}t$ for $\zeta = 0$ to $t/\sqrt{\lambda}$ for $\zeta > 0$.

TABLE I. Comparison between computational times required by a standard laptop computer running Python code with common ratio $\lambda = 2$ to yield equally accurate thermal dependencies of the electrical conductance with various offsets ζ.

ζ	CPU time (s)	$E_{\rm uv}/D$	$\langle\Delta\rangle$ (%)
0	432	14.	0.42
1	280	20.	0.44
2	500	41.	0.43
3	1 942	86.	0.42

Both the NRG and the eNRG procedures are based on controlable approximations. At low energies, ones that are small in comparison with the bandwidth, the deviations due to the discretization are controled by the parameter Λ and z in the NRG procedure. Likewise, the parameters λ and w control the deviations introduced by the eNRG discretization. The analytical computation of the temperature-dependent electrical conductance at a fixed point, in Appendix C, shows that the latter deviations grow in proportion to $\exp[-\pi^2/(2\ln\lambda)]$, and hence shrink as $\lambda \to 1$. Moreover, averaging of the conductances over w eliminates the deviations. In both procedures, the ultraviolet cutoff $E_{\rm uv}$ controls the deviations generated by the truncation of the discrete Hamiltonian.

As already discussed, at higher energies the offset controls the deviations due to the discretization. The parameter ζ guarantees that the largest energy scales in the conduction band, associated with the terms with index $n < \zeta$ in the infinite sum on the right-hand side of Eq. (10), be faithfully reproduced in the discretized Hamiltonian. The illustrative computation in Sec. IV B 1 will dwell on this point. Before that, however, Sec. IV A 4 describes a modification of the NRG procedure that would incorporate shifts analogous to the eNRG parameter ζ.

4. *Extension of the NRG method to accommodate offsets*

This section discusses a generalization of the momentum-space discretization allowing for offsets analogous to the eNRG parameter ζ in Fig. 3. The extension calls for a sequence of transformations. First, a Lanczos transformation, to convert the continuum of the conduction band into a tight-binding Hamiltonian. The second step is conceptual. It splits the tight-binding chain into two disjoint sets A and B. The former comprises the operators $a_0, a_1, \ldots, a_{\zeta-1}$, and the latter, the operators $a_\zeta, a_{\zeta+1}, \ldots, a_{\bar{L}}$. The quantum dot and set A are regarded as separate entities, to be coupled to B later. This ensures the states in the subspace spanned by the B operators to be orthogonal to those spanned by the A orbitals. The two sets are described by tight-binding Hamiltonians H_A and H_B.

The diagonalization of H_B yields $\bar{L} - \zeta + 1$ eigenvectors that are orthogonal to the operators in A and a band of eigenvalues that can be logarithmically discretized. Projection of H_B upon the resulting discrete states followed by a Lanczos transformation analogous to the one in Sec. III A 2 then reduces the discretized H_B to a tridiagonal form $\bar{H}_B$ coupled to the operator $a_{\zeta-1}$. At this point, the sum of the dot Hamiltonian, H_A, $\bar{H}_B$, and the couplings between the dot and between H_A and $\bar{H}_B$ constitute an infinite series that can be truncated and iteratively diagonalized. Clearly, this concatenation of operations is mathematically equivalent to the construction depicted in Fig. 3. By contrast, the eNRG procedure goes straight to the equivalent result.

As this example shows, the NRG and eNRG procedures are both flexible. Nonetheless, while a chain of operations are needed to bring out the flexibility of the former, the malleability of the latter is conspicuous. Section B 4 presents another example, focused on the two-dot problem. Two real-space discretizations are proposed. One of them, more accurate, is convenient if the dots lie close to each other. The other covers larger separations. Both might be used as blueprints to extend the NRG approach, much as Fig. 3 provided a road map leading to the above definition of a ζ-dependent NRG procedure. In those cases, too, the NRG constructions would be considerably more complex than their eNRG counterparts.

5. *eNRG analog of the z trick*

Comparison between the two procedures draws attention to two important constraints affecting the eNRG method only. Both limitations become evident when one examines the eigenvalues of the discretized conduction-band Hamiltonian. For odd truncation number $\mathcal{N}$ and $\zeta = 0$, for instance, the eigenvalues of the truncated eNRG Hamiltonian $H_{f\lambda}$ can be divided into symmetric pairs $\pm\epsilon_j$ $[j = 0, 1, \ldots, (\mathcal{N}+1)/2]$. Those whose absolute values are small compared to the tight-binding coupling t are approximately described by the equality

$$\epsilon_j = t_{\mathcal{N}-1}\lambda^{2j} \quad (j = 0, 1, \ldots). \tag{59}$$

The analogous NRG expression, approximately describing eigenvalues that are small compared in comparison with the half-bandwidth D, reads

$$\epsilon_j = \bar{t}_{\mathcal{N}-1}\Lambda^{j} \quad (j = 0, 1, \ldots), \tag{60}$$

but the *z trick* generalizes it to the form [35]

$$\epsilon_{j,z} = \bar{t}_{\mathcal{N}-1}\Lambda^{j+1-z} \quad (j = 0, 1, \ldots), \tag{61}$$

where z is an arbitrary real number in the interval $0.5 \leqslant z \leqslant 1.5$.

While Eq. (59) defines a single energy in each interval $[\lambda^{2j-1}, \lambda^{2j+1}]$, Eq. (61) spans the continuum of energies in the interval $[\Lambda^{j-\frac{1}{2}}, \Lambda^{j+1/2}]$, which proves practical to compute physical properties [4].

Appendix B 5 describes the analogous generalization for the eNRG approach. The extension introduces a third discretization parameter, the natural number w and modifies the real-space discretization so that cell $\mathcal{C}_n$ holds $w\lambda^n$ $(n = 0, 1, \ldots)$ sites, instead of λ^n. This *w trick* modifies the codiagonal coefficients (43), and substitutes the following expression for Eq. (59):

$$\epsilon_{j,w} = t_{\mathcal{N}-1}\lambda^{2j}/w \quad (j = 0, 1, \ldots; t_{\mathcal{N}-1}\lambda^{2j} \ll t). \tag{62}$$

With w restricted to the natural numbers, this amounts to a capped extension of Eq. (59). As the rigorous analysis in Sec. B 5 shows, however, the restriction can be removed. That Appendix extends expression (B35), from which Eq. (62) follows, to the domain $\{w \in \mathbb{R} \mid w \geqslant 1\}$. In particular, this extension maps the interval $\lambda \geqslant w \geqslant \lambda^{-1}$ onto the range $0.5 \leqslant z \leqslant 1.5$ covered by the NRG parameter.

Alternatively one can start out with the more general form of Eq. (59), valid for $\zeta = 0, 1, \ldots$:

$$\epsilon_j = t_{\mathcal{N}-1}\lambda^{2j+\zeta} \quad (j = 0, 1, \ldots; t_{\mathcal{N}-1}\lambda^{2j} \ll t). \tag{63}$$

Reasoning analogous to the mathematical analysis in Appendix B 5 can then be followed to extend the domain of the offsets from $\zeta \in \mathbb{N}$ to $\{\zeta \in \mathbb{R} \mid \zeta \geqslant 0\}$.

Comparison with Eq. (61) now relates the eNRG offset ζ to the NRG parameter z. Since Λ is equivalent to λ^2, the comparison yields

$$\zeta = 2(1 - z). \tag{64}$$

We might call this simple result the ζ trick. However, given that the offset is important on its own right, as the discussion in Sec. IV A 2 has shown, it seems more productive to confine ζ in the realm of the natural numbers and emulate the z trick with the w trick.

This concludes the first part of our comparison, which has appraised general aspects of the eNRG procedure. To sharpen the focus, we now turn to a specific problem.

B. Transport properties for the side-coupled device

Accurate NRG computations of the electrical and thermal conductances, and thermopower for the Anderson model were first reported by Costi and collaborators [45]. Their results for the thermal dependence of the electrical conductance have supported the interpretation of experimental data since the dawn of nanostructure fabrication [46–48]. More thorough studies of the other two transport properties emerged in the next decade and discussed the dependence of the thermopower on particle-hole asymmetry [49–51].

At the same time, NRG analysis centered on the series geometry showed that, while the transport properties for the symmetric model are universal functions of the temperature scaled by the Kondo temperature, particle-hole asymmetry breaks universality [52]. More recent work has shown that the transport properties for the asymmetric Hamiltonian can nonetheless be computed from temperature-dependent energy moments of the dot-orbital spectral density, which map linearly onto the universal thermal dependences for the symmetric Hamiltonian [53]. In all cases, the linear coefficients are trigonometric functions of the ground-state phase shift.

This record of NRG computations suffices to recommend the temperature-dependent transport properties as a means of comparison with the eNRG procedure. Clearly, either the series or the parallel geometries would serve that purpose; to sail unchartered waters, we prefer the latter. The comparison starts out in Sec. IV B 1 with the uncorrelated model. With $U = 0$, the physical properties for the tight-binding Hamiltonian can be calculated essentially exactly, and the iterative diagonalization procedures can bypass ultraviolet truncation. The exclusion of this significant source of deviation in the NRG and eNRG computations and the highly accurate conductances resulting from the diagonalization of the tight-binding Hamiltonian allow comparison between the two renormalization group procedures with nonpareil precision.

With $U \neq 0$, one must settle for less. The cost of diagonalizing the tight-bind Hamiltonian becomes prohibitive for $L > 30$, a limitation that blocks direct access to the thermal properties in the continuum limit. In the Kondo regime, nonetheless, universality offers an alternative. The thermal dependence of the electrical conductance through an SCD in the Kondo regime has already been shown to map linearly onto a universal function of the temperature scaled by the Kondo temperature [54,55]. Here, in Secs. IV B 2 and IV B 3, we show that the other transport properties, the Seebeck or Peltier coefficients, and the thermal conductance, conform to no such simple mapping. Like the properties for the single-electron transistor [53], however, they can be computed from three energy moments that map linearly onto universal functions. The deviations from linearity gauge the precision of numerical results. Such checks are reliable, even though less exact than the comparison between results for the $U = 0$ model.

1. Electrical conductances for the uncorrelated Hamiltonian

For $U = 0$, the model Hamiltonian is quadratic. The tight-binding Hamiltonian (1) can therefore be diagonalized for long chains, with very large L'. From the resulting eigenvalues and eigenvectors, physical properties can be accurately computed for energies $\mathcal{E}$ much larger than the energy splitting ΔE between successive single-particle levels in the vicinity of the Fermi level. Comparison with the same properties for the truncated Hamiltonian affords checks on the accuracy of the approximations leading to Eq. (49).

As an illustration, consider the thermal dependence of the electrical conductance G. A simple expression for the conductance of the device in Fig. 1 is available [55]; for $U = 0$, straightforward algebra reduces that expression to a sum involving the single-particle eigenvalues and eigenvectors:

$$G(T) = \frac{G_0}{\rho}\sum_n \{a_0^\dagger, g_n\}^2 \left(-\frac{\partial f_\beta(\epsilon)}{\partial \epsilon}\right)_{\epsilon=\mathcal{E}_n}, \tag{65}$$

where $G_0 \equiv 2e^2/h$ is the conductance quantum, g_n and $\mathcal{E}_n$ denote the nth single-particle eigenoperator and the corresponding eigenvalue of the truncated Hamiltonian (49), respectively, $\beta \equiv 1/(k_B T)$, and $f_\beta(\epsilon)$ is the Fermi function

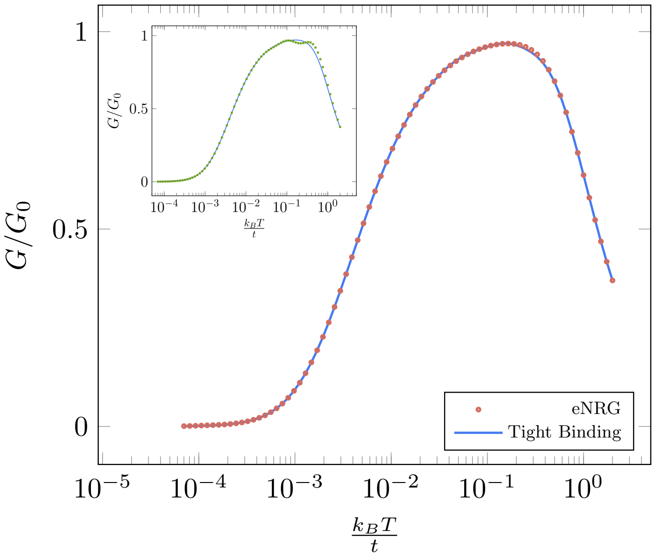

FIG. 4. Thermal dependence of the conductance for the $U = V_g = 0$ model, with level width $\Gamma = 1 \times 10^{-2}t$. The main plot shows the electrical conductance as a function of temperature. The circles were computed by the eNRG procedure, as the text describes. Each circle represents the average of two computations with $\lambda = 2$, for offsets $\zeta = 3$ and 4. The solid line resulted from numerically diagonalizing the ($\lambda = 1$) tight-binding Hamiltonian for $L = 20\,001$. The inset displays the analogous comparison for the NRG procedure. Each square is the average over z of two computations with $\Lambda = 4$, for $z = 0.5$ and $z = 1$.

$$f_\beta(\epsilon) = \frac{1}{1 + \exp(\beta\epsilon)}. \tag{66}$$

Figure 4 shows conductances numerically computed from Eq. (65) for the $U = V_g = 0$ model with $\Gamma = 0.01t$. The circles resulted from the diagonalization of the Hamiltonian $H_\mathcal{N}$ in Eq. (49) with $\lambda = 2$ for two offsets: $\zeta = 3$ and 4. Each point is the arithmetic average between $G(\zeta = 3, T)$ and $G(\zeta = 4, T)$.

The solid line in the figure represents conductances computed with $\lambda = 1$, that is, for the Hamiltonian (10), with $L' = 10\,000$. The resultant level spacing near the Fermi level, $\Delta E = 2\pi/L'$, allows accurate computation of the condutance for temperatures above $k_BT = 1 \times 10^{-3}t$.

The inset displays conductances obtained from Eq. (65) with eigenvalues and eigenvectors resulting from NRG diagonalizations of the model Hamiltonian, with the same model parameters. The circles result from diagonalization with $\Lambda = 4$ and $\mathcal{N} = 40$, while the solid line represents conductances computed with $\Lambda = 1.0001$ and $\mathcal{N} = 10\,000$. The solid lines in the main plot and inset are pratically identical, even thoug the latter is based on the NRG expression (17), which describes a conduction band with linear dispersion relation, while the former corresponds to a conduction band described by the tight-binding Hamiltonian in Eq. (28).

The rapid decay of the conductance has simple physical interpretation. At high temperatures, with $k_BT \gg \Gamma$, the impurity is effectively decoupled from the conduction band and allows ballistic transport through the chain. At low temperatures, with $k_BT \ll \Gamma$, the strong coupling to the impurity bars transport across the site a_0 and reduces G to zero.

As the plots show, at low temperatures both the NRG and eNRG procedures yield essentially exact results. At higher temperatures, the agreement between the circles and the solid line in the main plot is also excellent, while the inset displays significant deviations for $k_BT > 0.1t$. These discrepancies, of $\mathcal{O}(k_BT/D)$, are due to irrelevant operators introduced by the logarithmic discretization of the conduction band. By contrast, the eNRG procedure with offset $\zeta \geqslant 3$ describes the higher-energy degrees of freedom very well and hence allows accurate computation of physical properties over the entire temperature axis.

2. *Energy moments*

Consider, now the transport properties for the correlated model, and give attention to the Kondo regime, defined by the inequality

$$|V_g + \frac{U}{2}| < \frac{U}{2} - \Gamma. \tag{67}$$

In the Kondo regime, as the temperature is lowered past $\min(|V_g|, V_g + U)$, a local moment is formed at the quantum dot. Upon further cooling, a Kondo cloud gradually screens the magnetic moment. Well below the characteristic Kondo temperature T_K, the physical properties associated with the quantum dot show that the effective magnetic moment has been reduced to zero.

In the same way that the strong coupling between the quantum dot and the a_0 orbital blocks electrical conductance at low temperatures in Fig. 4, the formation of the Kondo cloud affects the transport properties of the side-coupled device. This section discusses the computation of three temperature-dependent energy moments, from which the electrical and thermal conductances, and the thermopower can be obtained.

Specifically, the following three moments have to be computed:

$$\mathcal{L}_j \equiv \frac{2}{\rho h}\int\left(-\frac{\partial f_\beta}{\partial\epsilon}\right)(\beta\epsilon)^j\rho_0(\epsilon, T)d\epsilon \quad (j = 0, 1, 2), \tag{68}$$

where $\rho_0(\epsilon, T)$ is the spectral density of the a_0 orbital:

$$\rho_0(\epsilon, T) = \frac{1}{\mathcal{Z}f_\beta(\epsilon)}\sum_{m,n} e^{-\beta E_m}|\langle m|a_0^\dagger|n\rangle|^2\delta(\epsilon - E_{mn}). \tag{69}$$

Here $|p\rangle$ and E_p $(p = m, n)$ denote the pth eigenvector and the corresponding eigenvalue of the model Hamiltonian, respectively, $E_{mn} \equiv E_m - E_n$, and $Z(T)$ is the partition function.

Substitution of the right-hand side of Eq. (69) for the spectral density on the right-hand side of Eq. (68) yields a simpler expression:

$$\mathcal{L}_j = \frac{2}{h}\frac{\beta}{\rho Z}\sum_{m,n}\frac{|\langle m|a_0|n\rangle|^2}{e^{\beta E_m} + e^{\beta E_n}}(\beta E_{mn})^j \quad (j = 0, 1, 2). \tag{70}$$

Once the energy moments are computed, the following equalities yield the electrical conductance G, thermopower S, and thermal conductance κ [49,56]:

$$G(T) = e^2\mathcal{L}_0(T), \tag{71}$$

$$S(T) = -\frac{\mathcal{L}_1(T)}{e\mathcal{L}_0(T)}, \tag{72}$$

and

$$\beta\kappa(T) = \mathcal{L}_2(T) - \frac{\mathcal{L}_1^2(T)}{\mathcal{L}_0(T)}. \tag{73}$$

In practice, to determine the transport properties we only have to compute the three moments $\mathcal{L}_j$ $(j = 0, 1, 2)$. This is a relatively simple task, since the iterative diagonalization of the truncated Hamiltonian (49) determines the eigenvalues, and the recursive procedure introduced in Ref. [30] gives immediate access to the matrix elements on the right-hand side of Eq. (70).

3. *Universality*

In the Kondo model, a spin-1/2 variable represents the impurity, and the renormalization group space comprises only the symmetric LM and the FL fixed points. In his groundbreaking study of the Kondo Hamiltonian, Wilson offered a renormalization group analysis proving the crossover from the LM to the FL fixed point to be universal [1].

The analysis was subsequently extended to the Anderson Hamiltonian, and additional fixed points emerged: the free-orbital and the valence-fluctuation (VF) fixed points [2,3]. At high temperatures, the model Hamiltonian may be close to the FO fixed point, already discussed in Sec. III B 5. At lower temperatures it may or may not come close to a VF fixed point before approaching the LM fixed point. While the higher-temperature transitions are nonuniversal, the crossover from any LM fixed point to the FL line of fixed points is universal. The thermodynamical properties for the Kondo model and Kondo regime of the Anderson model are therefore universal functions of the temperature scaled by the Kondo temperature [1,2]. Zero-temperature excitation properties are, likewise, universal functions of the energy scaled by the Kondo thermal energy [35].

Universality provides insight and simplifies theoretical analyses, on the one hand, and aids the interpetation of experimental results, on the other. Fits to laboratory data offer *prima-facie* evidence of Kondo physics [46], for instance.

In contrast with the temperature dependence of thermodynamical properties and with the frequency dependence of excitation properties, the temperature-dependent transport properties cannot be universal functions of T/T_K, however. Straightforward scattering theory analysis shows that, at the LM fixed point with phase shift $\bar{\delta}$, the probability for transmission across the side-coupled device is $\cos^2\bar{\delta}$. The three energy moments must therefore depend on $\bar{\delta}$, which is model-parameter dependent.

For the symmetric model, early renormalization group analysis showed that the Kondo-regime electrical conductance of the side-coupled device is a universal function $G_{\text{uni}}(T/T_K)$, of the temperature scaled by the Kondo temperature [45]. For asymmetric models, the conductance was later shown to map linearly onto G_{uni}, with coefficients dependent on the phase shift δ only [54,55]. Recent work has extended the approach to the three energy moments that determine the transport properties for the single-electron transistor [53]. It resulted that, for the symmetric model, each moment is a universal function $f_n(T/T_K)$ and that, for asymmetric models, the nth moment maps linearly onto $f_n(T/T_K)$, with n-dependent coefficients fixed by the FL.

Here, with a view to benchmarking the accuracy of the eNRG procedure on the basis of new analytical results, we extend the findings of Refs. [54,55] to the energy moments in Eq. (68). To gauge the precision of the procedure, we can then compute the thermal dependence of each energy moment numerically and compare the result with the temperature dependence predicted by the mapping to the pertinent universal function. Our derivation moreover maps the temperature-dependent electrical and thermal conductances and thermopower calculated in parallel geometry to universal functions, a development of practical interest, since it simplifies the interpretation of experimental results in bulk systems. Section IV B 6 presents two illustrative examples.

Whether one is interested in laboratory data or in theoretical results, the mappings cover the relatively low temperatures associated with the Kondo crossover, from the LM to the FL fixed point. The higher temperature transitions are nonuniversal and cannot be mapped onto unique functions. They cannot be described by the Kondo model, either. They nonetheless lie within the scope of the Anderson model, and the physical properties in the pertinent temperature range can therefore be accurately computed by the eNRG procedure, as the numerical results in Secs. IV B 1 and IV B 4 a will show.

a. Universal matrix elements. In the Kondo regime, well above the Kondo temperature, the model Hamiltonian lies close to the LM. The deviations are described by the Kondo Hamiltonian $\mathcal{H}_{\text{JW}}$:

$$\mathcal{H}_{\text{JW}} = \sum_k \epsilon_k a_k^\dagger a_k + \bar{W} a_0^\dagger a_0 + J \sum_{\mu\nu} a_{0\mu}^\dagger \sigma_{\mu\nu} a_{0\nu} \cdot \mathbf{S}, \tag{74}$$

where the potential scattering $\bar{W}$ and the exchange J depend on the model parameters.

Where guidelines are needed before numerical diagonalization, estimates can be obtained from the Schrieffer-Wolff expressions [57]

$$\rho J = \frac{2\Gamma U}{\pi |V_g|(V_g + U)} \tag{75}$$

and

$$\rho \bar{W} = \frac{\Gamma(V_g + \frac{U}{2})}{\pi |V_g|(V_g + U)}, \tag{76}$$

which become accurate near the symmetric point $V_g = -U/2$ [3,58,59].

In practice, however, both J and W are extracted from the numerical results. In particular, the eigenvalues of the Hamiltonian in the vicinity of the LM fixed point determines the scattering potential. Equation (53) then yields the LM phase shift $\bar{\delta}$ and, through Eq. (58), the FL phase shift δ. Alternatively, the latter can be extracted from the low-energy eigenvalues, a simpler expedient that yields more accurate results, and Eq. (58) determines the LM phase shift. The following analysis shows that this is sufficient to determine the transport properties as functions of the temperature scaled by the Kondo temperature.

Given the FL phase shift, we must eliminate the scattering potential from Eq. (74). To this end, it is sufficient to project $\mathcal{H}_{\text{JW}}$ onto the basis of the $\mathcal{H}^*_{\text{LM},\bar{\delta}}$ eigenvectors g_ℓ. The projection generates irrelevant operators, which can be safely dropped. The remaining terms yield the expression [52]

$$\mathcal{H}_{\text{JW}} = \sum_\ell \varepsilon_\ell g_\ell^\dagger g_\ell + J_{\bar{W}} \sum_{\mu\nu} \phi_{0\mu}^\dagger \vec{\sigma}_{\mu\nu} \phi_{0\nu} \cdot \vec{S}, \tag{77}$$

where

$$J_{\bar{W}} = J \cos^2(\bar{\delta}) \tag{78}$$

and

$$\phi_0 \equiv \frac{1}{\sqrt{N}} \sum_\ell g_\ell. \tag{79}$$

At high energies, comparable to the conduction bandwidth $4t$, the contribution from the irrelevant operators makes the spectra of the Hamiltonians on the right-hand sides of Eqs. (74) and (77) somewhat different. As the energy $\mathcal{E}$ decreases, however, the deviations shrink and become negligible for $\mathcal{E} \ll t$.

Equation (77) describes the physical properties of the model Hamiltonian in the vicinity of the LM. As the energy scale is reduced, the eigenstates and eigenvalues of the model Hamiltonian progressively deviate from the spectrum of $\mathcal{H}^*_{\text{LM},\bar{\delta}}$. It is then convenient to switch to another basis, in which the basis vectors are linear combinations of the operators g_ℓ with the Legendre polynomials $P_k(\epsilon)$ $(k = 0, 1, \ldots)$ as coefficients:

$$\phi_k \equiv \mathcal{N}_k \sum_\ell P_k(\epsilon_\ell) g_\ell \quad (k = 0, 1, \ldots), \tag{80}$$

and appropriate normalization factors $\mathcal{N}_k$.

The leading basis vector is ϕ_0, defined by Eq. (79). Next comes the operator

$$\phi_1 \equiv \sqrt{\frac{\lambda^2 - 1}{2\lambda}} \sum_\ell P_1(\epsilon_\ell) g_\ell, \tag{81}$$

which plays an important role in the following analysis.

The second term on the right-hand side of Eq. (77) is a marginally relevant operator, which brings the Hamiltonian from the LM to the FL. The trajectory in renormalization group space is universal, since a single operator drives the flow. The coupling $J_{\bar{W}}$ defines the Kondo temperature T_K. Scaling by $k_B T_K$ brings the spectra of Hamiltonians of the form (77) with different couplings to congruence.

In other words, the same eigenvalues and eigenstates contribute to physical properties computed for Hamiltonians with different couplings at temperatures such that the ratio T/T_K is the same. Matrix elements of the operators ϕ_0 and ϕ_1 between eigenstates of the Kondo Hamiltonian are likewise universal.

To determine the energy moments (70), the matrix elements $\langle m|a_0|n\rangle$ must be computed, where $|m\rangle$ and $|n\rangle$ are eigenstates of the truncated Hamiltonian (49). The matrix elements are linear combinations of the matrix elements $\langle m|\phi_0|n\rangle$ and $\langle m|\phi_1|n\rangle$ [52]:

$$\langle m|a_0|n\rangle = \alpha_0\langle m|\phi_0|n\rangle + \alpha_1\langle m|\phi_1|n\rangle, \tag{82}$$

with model-parameter dependent coefficients α_0 and α_1.

Given that all coefficients t_n in the truncated Hamiltonian are real, the α_n $(n = 0, 1)$ and matrix elements in Eq. (82) can be asssumed real, with no loss of generality. The squared matrix element in the summand on the right-hand side of Eq. (70) are therefore given by the equality

$$\begin{aligned}|\langle m|a_0|n\rangle|^2 =& \alpha_0^2\langle m|\phi_0|n\rangle^2 + \alpha_1^2\langle m|\phi_1|n\rangle^2\\ &+ 2\alpha_0\alpha_1\langle m|\phi_0|n\rangle\langle m|\phi_1|n\rangle.\end{aligned} \tag{83}$$

Substitution of the right-hand side for $|\langle m|a_0|n\rangle|^2$ in Eq. (70) splits each energy moment into three terms:

$$\mathcal{L}_j = \alpha_0^2\mathcal{L}_{00}^{(j)} + 2\alpha_0\alpha_1\mathcal{L}_{01}^{(j)} + \alpha_1^2\mathcal{L}_{11}^{(j)} \quad (j = 0, 1, 2), \tag{84}$$

where

$$\mathcal{L}_{00}^{(j)} \equiv \frac{2}{\rho h}\frac{\beta}{Z}\sum_{m,n}\frac{\langle m|\phi_0|n\rangle^2}{e^{\beta E_m} + e^{\beta E_n}}(\beta E_{mn})^j, \tag{85}$$

$$\mathcal{L}_{01}^{(j)} \equiv \frac{2}{\rho h}\frac{\beta}{Z}\sum_{m,n}\frac{\langle m|\phi_0|n\rangle\langle m|\phi_1|n\rangle}{e^{\beta E_m} + e^{\beta E_n}}(\beta E_{mn})^j, \tag{86}$$

and

$$\mathcal{L}_{11}^{(j)} \equiv \frac{2}{\rho h}\frac{\beta}{Z}\sum_{m,n}\frac{\langle m|\phi_1|n\rangle^2}{e^{\beta E_m} + e^{\beta E_n}}(\beta E_{mn})^j. \tag{87}$$

The summand on the right-hand side of Eq. (80), which defines ϕ_k $(k = 0, 1, \ldots)$, is proportional to the Legendre Polynomial $P_k(\epsilon)$, a function of the energy with the parity of k. The matrix elements $\langle m|\phi_k|n\rangle$ and $\langle n|\phi_k|m\rangle$ hence have the same sign for $k = 0$ and opposite signs for $k = 1$. For even j, therefore, the summands on the right-hand sides of Eqs. (85) and (87) remain invariant under exchange of the summation indices $(m \leftrightarrow n)$, while the summand in Eq. (86) changes sign. Conversely, for odd j the summands in Eqs. (85) and (87) change sign under index exchange, while the summand on the right-hand side of Eq. (86) remains invariant. It follows that

$$\mathcal{L}_{01}^{(0)} = \mathcal{L}_{01}^{(2)} = \mathcal{L}_{00}^{(1)} = \mathcal{L}_{11}^{(1)} = 0. \tag{88}$$

Moreover, as Appendix D shows, the moments defined in Eq. (87) are related to the ones in Eq. (85):

$$\frac{\pi^2}{2}\mathcal{L}_{11}^{(0)}(T) = \frac{2}{h} - \mathcal{L}_{00}^{(0)}(T) \tag{89}$$

and

$$\frac{\pi^2}{2}\mathcal{L}_{11}^{(2)}(T) = \frac{2\pi^2}{3h} - \mathcal{L}_{00}^{(2)}(T). \tag{90}$$

TABLE II. Gate potential, phase shifts and Kondo temperatures for the six eNRG runs that yielded the data in Fig. 5 (runs $a - c$), and Figs. 6, 8–12 (runs $A - C$).

Run	Symbol	U	V_g/U	δ/π	k_BT_K/t	ρJ
a	—	0.01	−0.5	0.500	6.4×10^{-5}	0.65
b	⋯	0.01	−0.65	−0.491	1.5×10^{-4}	0.71
c	- - -	0.01	−0.80	−0.470	2.0×10^{-3}	1.01
A	—	10	−0.5	0.500	6.4×10^{-5}	0.65
B	⋯	10	−0.65	−0.491	1.5×10^{-4}	0.71
C	- - -	10	−0.80	−0.470	2.0×10^{-3}	1.01

Only the moments $\mathcal{L}_{00}^{(0)}(T)$, $\mathcal{L}_{01}^{(1)}(T)$, and $\mathcal{L}_{00}^{(2)}(T)$ need be computed, therefore, to determine the right-hand side of Eq. (84). For $j = 0$, given that $\mathcal{L}_{01}^{(0)} = 0$, the equality is equivalent to the expression

$$\mathcal{L}_0(T) = \left(\alpha_0^2 - \tilde{\alpha}_1^2\right)\mathcal{L}_{00}^{(0)}(T) + \frac{2}{h}\tilde{\alpha}_1^2, \tag{91}$$

with the shorthand $\tilde{\alpha}_1 \equiv \sqrt{2}\alpha_1/\pi$.

For $j = 1$, Eq. (84) amounts to

$$\mathcal{L}_1(T) = 2\alpha_0\alpha_1\mathcal{L}_{01}^{(1)}(T), \tag{92}$$

and for $j = 2$, to

$$\mathcal{L}_2(T) = \left(\alpha_0^2 - \tilde{\alpha}_1^2\right)\mathcal{L}_{00}^{(2)}(T) + \frac{2\pi^2}{3h}\tilde{\alpha}_1^2. \tag{93}$$

As already explained, the matrix elements $\langle m|\phi_k|n\rangle$ $(k = 0, 1)$ and the eigenvalues E_m and E_n on the right-hand sides of Eqs. (85), (86), and (87) are universal functions of the energy scaled by k_BT_K. The three moments $\mathcal{L}_{00}^{(0)}$, $\mathcal{L}_{01}^{(1)}$, and $\mathcal{L}_{00}^{(2)}$ are universal functions of the ratio T/T_K. Equations (91)–(93) map the energy moments $\mathcal{L}_0$, $\mathcal{L}_1$, and $\mathcal{L}_2$ onto $\mathcal{L}_{00}^{(0)}$, $\mathcal{L}_{01}^{(1)}$, and $\mathcal{L}_{00}^{(2)}$, respectively. The following analysis shows the linear coefficients α_0 and $\tilde{\alpha}_1$ to be trigonometric functions of the fixed-point phase shifts.

b. Linear coefficients. At the LM and FL, the spectral densities for the operator f_0 are [54]

$$\rho_0 = \rho\cos^2\bar{\delta} \quad \text{(LM)}, \tag{94}$$

$$\rho_0 = \rho\cos^2\delta \quad \text{(FL)}. \tag{95}$$

Equation (58) relates the LM phase shift $\bar{\delta}$ to the FL phase shift δ. Substitution of Eq. (94) for the spectral density on the right-hand side of Eq. (68) followed by integration yields the following limits for the lowest-order moment:

$$\mathcal{L}_0 = \begin{cases}\dfrac{2}{h}\sin^2\delta & \text{(LM)}\\[2mm] \dfrac{2}{h}\cos^2\delta & \text{(FL)}\end{cases}. \tag{96}$$

The right-hand sides of Eq. (96) can now be combined with Eq. (91) to relate the high- and low-temperature limits of the universal moment $\mathcal{L}_{00}^{(0)}$ to the phase shift:

$$\frac{2}{h}\sin^2\delta = \left(\alpha_0^2 - \tilde{\alpha}_1^2\right)\mathcal{L}_{00}^{(0)}(LM) + \frac{2}{h}\tilde{\alpha}_1^2 \quad \text{(LM)} \tag{97}$$

and

$$\frac{2}{h}\cos^2\delta = \left(\alpha_0^2 - \tilde{\alpha}_1^2\right)\mathcal{L}_{00}^{(0)}(FL) + \frac{2}{h}\tilde{\alpha}_1^2 \quad \text{(FL)}. \tag{98}$$

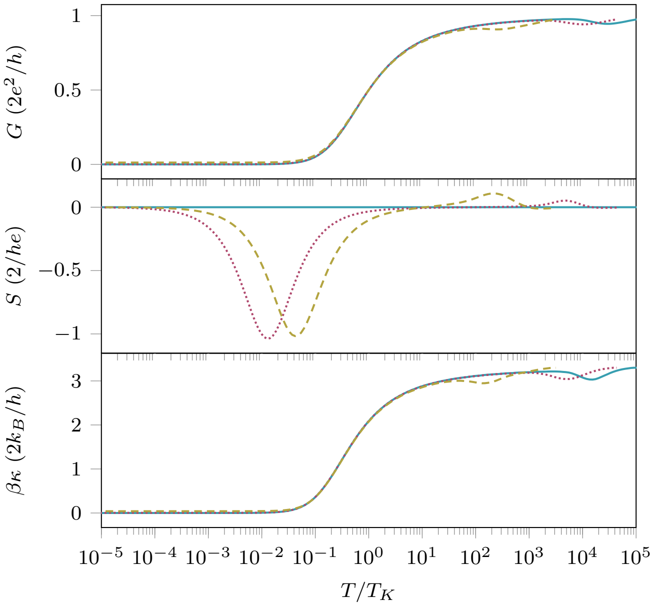

FIG. 5. Temperature dependence of the conductance (top), thermopower (central), and thermal conductance divided by the temperature (bottom panel), computed from Eqs. (71), (72), and (73), respectively. In each panel, the solid cyan, dotted magenta, and dashed olive lines represent runs a, b, and c, respectively, defined by the parameters in Table II. Each panel depicts two crossovers. The nonuniversal crossover from the free-orbital to the local moment occurs above $T = 10\,T_K$, while the universal transition from the local moment to the strong-coupling fixed point takes place in the vicinity of $T = T_K$.

The universal moment $\mathcal{L}_{00}^{(0)}(T/T_K)$ is proportional to the SCD conductance for the symmetric model [54] and hence drops from $\mathcal{L}_{00}^{(0)}(LM) = 2/h$ at the LM to $\mathcal{L}_{00}^{(0)}(FL) = 0$ at the FL. Equations (97) and (98) therefore reduce to the equalities $\alpha_0^2 = \sin^2\delta$ and $\tilde{\alpha}_1^2 = \cos^2\delta$, respectively, which determine the absolute values of α_0 and $\tilde{\alpha}_1$.

To determine the signs, we set $J = 0$ on the right-hand side of Eq. (74). The resulting Hamiltonian is quadratic and can be diagonalized analytically [52]. It is then a simple matter to evaluate the matrix elements on both sides of Eq. (82), from which it follows that that $\alpha_0 = \cos\bar{\delta}$ and $\tilde{\alpha}_1 = -\sin\bar{\delta}$. Equation (58) then expresses the two coefficients as trigonometric functions of the FL phase shift:

$$\alpha_0 = -\sin\delta \tag{99}$$

and

$$\tilde{\alpha}_1 = -\cos\delta. \tag{100}$$

Substitution on the right-hand side of Eq. (92) yields the mapping between the energy moment $\mathcal{L}_1$ and the universal moment $\mathcal{L}_{01}^{(1)}$:

$$\mathcal{L}_1(T/T_K) = \frac{\pi}{\sqrt{2}}\sin(2\delta)\mathcal{L}_{01}^{(1)}(T/T_K). \tag{101}$$

Likewise, substitution of Eqs. (99) and (100) on the right-hand sides of Eqs. (91) and (93) determines the coefficients mapping $\mathcal{L}_0$ and $\mathcal{L}_2$ onto the universal moments $\mathcal{L}_{00}^{(0)}$ and $\mathcal{L}_{00}^{(2)}$,

$$\mathcal{L}_0(T/T_K) = -\cos(2\delta)\mathcal{L}_{00}^{(0)}(T/T_K) + \frac{1}{h}(1+\cos 2\delta) \tag{102}$$

and

$$\mathcal{L}_2(T/T_K) = -\cos(2\delta)\mathcal{L}_{00}^{(2)}(T/T_K) + \frac{\pi^2}{3h}(1+\cos 2\delta), \tag{103}$$

respectively.

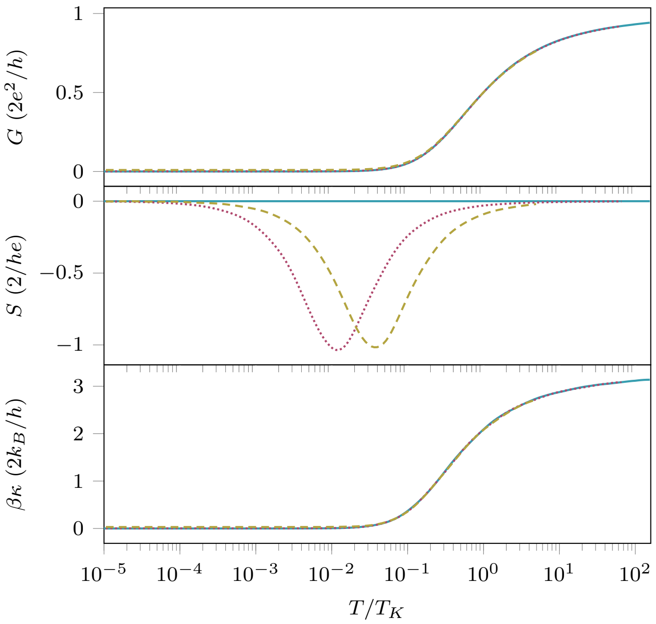

FIG. 6. Temperature dependence of the conductance (top), thermopower (middle), and thermal conductance divided by the temperature (bottom), computed from Eqs. (71), (72), and (73), respectively. In each panel, the solid cyan, dotted magenta, and dashed olive lines represent runs A, B, and C, respectively

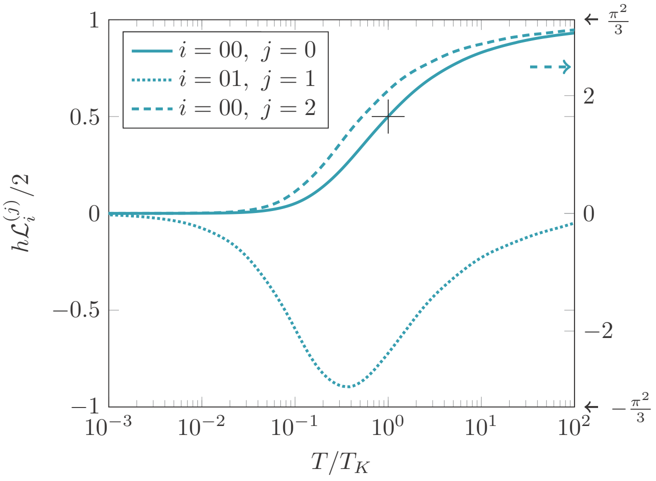

FIG. 7. Universal energy moments $\mathcal{L}_{00}^{(0)}$, $\mathcal{L}_{01}^{(1)}$, and $\mathcal{L}_{00}^{(2)}$ as functions of the temperature scaled by T_K. The hairlines mark the definition $\mathcal{L}_{00}^{(0)}(T/T_K = 1) = 1/h$ of the Kondo temperature.

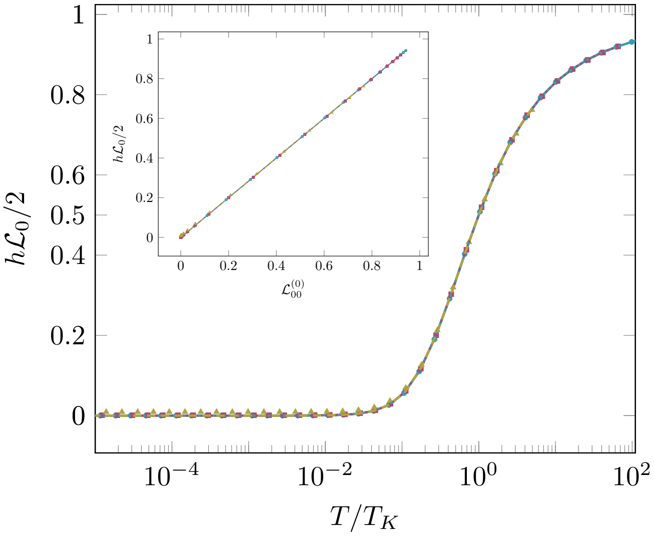

FIG. 8. First energy moment as a function of the temperature scaled by T_K. The filled circles, squares, and triangles, fitted by the solid cyan, dotted magenta, and dashed olive lines depict the numerical data resulting from eNRG runs A, B, and C, respectively. The lines represent Eq. (102) for the tabulated phase shifts in the three runs. The inset shows the energetic moment as a function of the universal curve $\mathcal{L}_{00}^{(0)}(T/T_K)$ for the three runs. The excellent agreement between the circles and the straight line fitting them witnesses the linearity of the mapping.

The phase shift for the symmetric Hamiltonian is $\delta = \pi/2$. Equations (101)–(103) then reduce to $\mathcal{L}_1(T/T_K) = 0$ and $\mathcal{L}_j(T/T_K) = \mathcal{L}_{00}^{(j)}(T/T_K)$ ($j = 0, 2$), as expected.

The three expressions map the three energy moments onto universal functions. They reduce all temperature dependence to universal functions, which we need to compute only once. At the symmetric point, $\mathcal{L}_1$ vanishes, while $\mathcal{L}_0$ and $\mathcal{L}_2$ reduce to the universal functions. Particle-hole asymmetry makes $\mathcal{L}_1$ nonzero and flattens the temperature dependence of the other two moments. In all cases, the mapping is linear, with slopes and intercepts that depend on the ground-state phase shift only. The following section exhibits eNRG data confirming these findings.

4. *Numerical results*

Table II lists the gate potentials defining six eNRG runs. The Coulomb repulsion is $U = 0.01\,t$ in runs $a - c$ and $U = 10\,t$ in runs $A - C$. In all cases, the dot-level width is a fixed fraction of the Coulomb repulsion, $\Gamma = 0.040\,U$. The ratio $\Gamma/\min(|V_g|, U + V_g)$ is 0.08, 0.11, and 0.2 in runs a and A, b and B, and c and C, respectively. At sufficiently low temperatures, runs a, b, A, and B lie well within the Kondo regime, a condition that warrants the mappings to the universal functions and enhances the departures from the Wiedemann-Franz law, as discussed in Sec. IV B 4 c. By contrast, the proximity of runs c and C to the charge-degeneracy point $V_g = -U$ gives rise to significant deviations from universality. In runs a and b, with $U \ll t$, the model Hamiltonian only enters the Kondo regime at relatively low temperatures, $k_BT \ll U$. In runs A and B, by contrast, a local moment is formed around $k_BT = 0.1\,t$, which marks the inception of Kondo screening. Universality therefore prevails at relatively high temperatures in runs A and B.

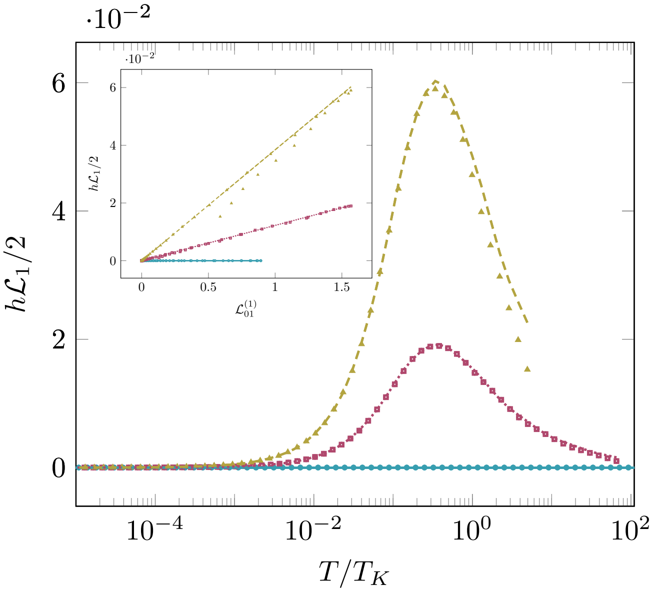

FIG. 9. Temperature dependence of the second energy moment. The plots follow the symbol convention in Fig. 8. The inset shows $\mathcal{L}_1(T/T_K)$ as a function of the universal moment $\mathcal{L}_{01}^{(1)}(T/T_K)$, to probe Eq. (101) visually. Both the main plot and inset display distinct deviations from universal behavior at high temperatures, an indication that the relatively large $|V_g + U/2|$ has pushed run C too close to the charge degeneracy point $V_g = -U$.

a. Thermoelectric properties. Along with the Coulomb energy U, and gate potential V_g, Table II presents the ground-state phase shift δ, the Kondo thermal energy k_BT_K, the Kondo coupling J computed from Eq. (75), and the style of the line representing each run in Figs. 5, 6, and 8–11. Figure 5 displays the conductance, thermopower, and thermal conductance computed in runs $a - c$ as functions of the temperature scaled by the Kondo temperature. In each panel, for $T > 10T_K$, the three curves resulting from the three runs display clear distinctions. The broad minima in the top and bottom panels, and the maxima in the middle panel mark the nonuniversal crossovers from the free-dot-orbital fixed point (region above $V_g + U$ in Fig. 2) to the local-moment fixed points (region between $V_g + U$ and Γ_K in that figure). As T drops below $10T_K$, the nearly coincident plots in Figs. 5(a) and 5(b) signal ascent into the Kondo regime, and consequent mapping of the energy moments $\mathcal{L}_j(T/T_K)$ onto universal functions. Since G is proportional to $\mathcal{L}_0$, and $\beta\kappa$ is approximately equal to $\mathcal{L}_2$, the two conductance curves are weakly dependent on the model parameters. The thermopower is the ratio between two energy moments; moreover, Eq. (101) shows that $\mathcal{L}_1$ is proportional to a trigonometric function that vanishes under particle-hole symmetry. Even in the Kondo regime, $S(T/T_K)$ is therefore sensitive to changes in the model parameters.

Comparison between the plots in Fig. 5 ($U = 0.01\,t$) and the corresponding plots in Fig. 6 ($U = 10\,t$) corroborates this interpretation. Even though the model parameters are

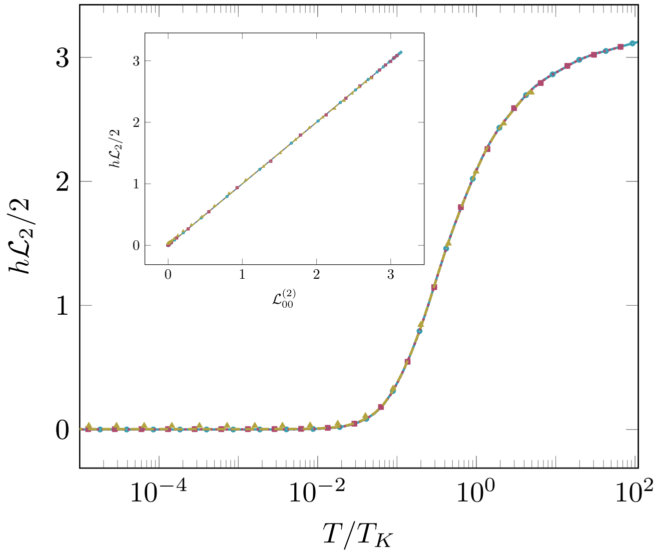

FIG. 10. Temperature dependence of the third energy moment. The plots follow the symbol convention in Figs. 8 and 9. The inset shows $\mathcal{L}_2(T/T_K)$ as a function of the universal moment $\mathcal{L}_{00}^{(2)}(T/T_K)$ to corroborate Eq. (103).

thousandfold larger than in runs $a-c$, the representations of $G(T/T_K)$, $S(T/T_K)$, and $\beta\kappa(T/T_K)$ in Fig. 6 are virtually identical to those in the Kondo-regime temperature range of Fig. 5. The crossover from the free-orbital to the local-moment fixed point for the parameters in runs $A-C$ lies above the highest computed temperatures. Only the Kondo crossover is encompassed in the figure. The displayed physical properties are therefore in the interval within the scope of universality.

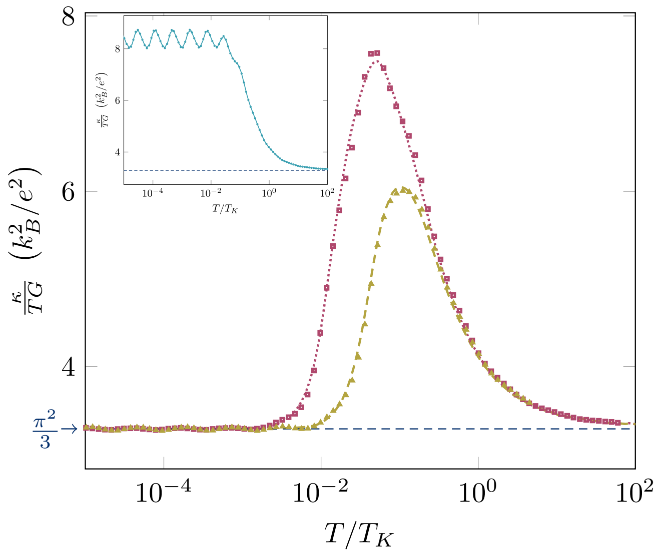

FIG. 11. Wiedemann-Franz ratio as a function of the temperature scaled by T_K for runs B and C. The symbol convention follows Fig. 6. At high and low temperatures, the plots approach the Lorenz number $L_0 = (\pi^2/3)(k_B/e)^2$. The inset shows the results from run A, which are markedly different for $T < T_K$ because both G and $\beta\kappa$ vanish as $T \to 0$ at the symmetric point.

In Fig. 6, and in the Kondo-regime range of Fig. 5, the electrical-conductance $G(T/T_K)$ and the thermal-conductance $\beta\kappa(T/T_K)$ curves are similar. As the temperature drops, both functions decay monotonically to zero, from the high-temperature plateaus of $G(T \gg T_K) = G_0$ and $\beta\kappa(T/T_K) = (2\pi^2/3)k_B/h$. Physically, at high temperatures, the conduction electrons flow ballistically across the quantum wire; the antiferromagnetic interaction with the dot magnetic moment offers little resistance to transport. Upon cooling, the Kondo cloud is gradually formed, and the progressively stronger coupling between conduction states and the dot orbital obstructs conduction through the central region of the wire.

The three conductance curves in each top panel are nearly undistinguishable, a coincidence that turns our attention to the phase shifts in Table II. The tabulated phase shifts are close to $\pi/2$ because the three runs are in the Kondo regime: on the scale of Γ, runs A and B are far from the charge-degeneracy point $V_g = -U$, while run C is moderately distant from it. How does that affect the conductance? Equation (102) shows that the moment $\mathcal{L}_0(T)$ and, hence, the conductance $G(T)$ are parametrized by $\cos 2\delta$. In the Kondo regime, this trigonometric function lies close to its minimum and is, hence, nearly independent of δ. The three curves in the top panel are, therefore, practically congruent.

For the same reason, the three curves in each bottom panel are virtually identical. In the middle panel, however, the distinctions are patent. The Seebeck coefficient monitors the difference between electron and hole conduction. Unlike the conductances, the thermopower changes sign under the particle-hole transformation. $S(T)$ vanishes in run A, for the symmetric model, with $V_g + U/2 = 0$, depicted by the solid cyan line in the figure. For $V_g + U/2 < 0$, as in runs B and C, the thermopower is negative. For $V_g + U/2 > 0$ (not shown), it is positive.

Physically, the thermoelectric effect stems from transport across the quantum wire assisted by virtual excitations to the quantum dot. In the Kondo regime, the dot occupation is close to $n_d = 1$, as Fig. 2 indicates. With $V_g + U/2 < 0$ ($V_g + U/2 > 0$) the dominant excitation is a transition from one of the central columns to the rightmost (leftmost) one, which transfers an electron (a hole) to the quantum dot; the resulting Seebeck coefficient is negative (positive).

At high temperatures, independently of the sign of $V_g + U/2$, electrons flow freely across the wire. Nonetheless, the weak coupling to the dot reduces $S(T \gg T_K)$ to zero. At low temperatures, the dot is strongly coupled to the wire, but the Kondo cloud blocks transport. Only at intermediate temperatures can the Seebeck coefficient differ significantly from zero.

The thermopower is the ratio on the right-hand side of Eq. (72), between the moments $\mathcal{L}_1(T)$ and $\mathcal{L}_0(T)$. If the ratio were proportional to a universal function, only the amplitude of the plot would depend on V_g. The numerator $\mathcal{L}_1(T)$ is, in fact, proportional to the universal moment $\mathcal{L}_{01}^{(1)}(T/T_K)$, but the denominator $\mathcal{L}_0(T)$ is neither universal nor proportional to a universal function, as Eq. (102) shows. The weak dependence of the denominator on the phase shift δ is sufficient to shift the symmetric maximum from $0.01T_K$ to approximately $0.04T_K$ as the phase shift grows from $\delta = -0.49\pi$ to $\delta = -0.47\pi$.

b. Universal moments. Figure 7 shows the thermal dependence of the universal energy moments $\mathcal{L}_{00}^{(0)}$, $\mathcal{L}_{01}^{(1)}$, and $\mathcal{L}_{00}^{(2)}$ onto which the temperature dependencies of the transport moments $\mathcal{L}_0$, $\mathcal{L}_1$, and $\mathcal{L}_2$ are linearly mapped, respectively. The solid line depicts $\mathcal{L}_{00}^{(0)}(T/T_K)$, which is proportional to the conductance at the symmetric point. As the temperature drops, $\mathcal{L}_{00}^{(0)}$ diminishes monotonically to zero, from the ballistic limit $\mathcal{L}_{00}^{(0)}(T \gg T_K) = 2/h$. The hairlines identify the halfway point $\mathcal{L}_{00}^{(0)}(T = T_K) \equiv 1/h$, which defines the Kondo temperature.

The dashed line depicts the analogous decline of the universal moment $\mathcal{L}_{00}^{(2)}(T/T_K)$. The curve decays to zero from the high-temperature plateau $\mathcal{L}_{00}^{(2)} = 2\pi^2/(3h)$, and crosses its half-maximum $\pi^2/(3h)$ at $T \approx T_K/2$.

The temperature dependence of the universal moment $\mathcal{L}_{01}^{(1)}(T/T_K)$ is conspicuously distinct. The moment vanishes at high and low temperatures, and becomes negative throughout the crossover from the LM to the FL. The dotted line in Fig. 7 displays a broad, nearly symmetric minimum centered at $T \approx 0.4T_K$.

Figure 8 compares numerically computed moments with the mapping (102). The moments $\mathcal{L}_0(T)$ computed in the three runs in Table II are represented by circles, plotted as functions of the ratio T/k_BT_K in the range $1 \times 10^{-5} < T/T_K < 1 \times 10^2$. The solid lines show the right-hand side of Eq. (102), parametrized by the tabulated δ. The phase shifts being close to each other, the three curves are nearly coincident. Even the small differences between moments correspondent to phase shifts only a few percent apart are accurately reproduced by the universal mappings, however.

For better comparison, the inset of Fig. 8 plots the computed moments as functions of the universal moment $\mathcal{L}_{00}^{(0)}$. The excellent agreement with the straight lines representing Eq. (102) for the pertinent phase shifts attests the accuracy of the data. The same procedure can be applied to experimental results, as illustrated by analyses focused on data collected in side-coupled devices [54] or single-electron transistors [60]. More on that in Sec. IV B 6 a.

Figure 9 shows the analogous plots for the $\mathcal{L}_1(T)$ moment. The results from run A are shown for completeness only, because $\mathcal{L}_1(T)$ vanishes at all temperatures. The moments from runs B and C are positive because $V_g + U/2 < 0$, which makes the Schrieffer-Wolff scattering potential $\bar{W}$ negative. The LM phase shift $\bar{\delta}$ is hence positive, the FL phase shift δ is negative, and so is the factor multiplying $\mathcal{L}_{01}^{(1)}$ on the right-hand side of Eq. (101). For $V_g + U/2 > 0$ (not shown), the moment is negative at all temperatures, a reminder that the thermopower is very sensitive to particle-hole asymmetry.

The dotted magenta lines in the main plot and inset show good agreement with the filled magenta squares. The small deviations at the highest temperatures are contributions from the $\mathcal{O}(\rho k_B T)$ terms neglected in the derivation of Eq. (101), which become significant for $k_BT \gtrsim 5 \times 10^{-3}$, that is, for $T \gtrsim 5T_K$ in run B. Manifest deviations with the same origin separate the olive triangles representing the moments computed in run C from the olive dashed line. Since run C is relatively close to the charge-degeneracy point $V_g = -U$, the Kondo temperature $k_BT_K = 2 \times 10^{-3}t$ is fairly high, and the discrepancies become visible even below the Kondo temperature.

The filled circles, squares, and triangles in the main plot of Fig. 10 show the $\mathcal{L}_2$ computed in runs A, B, and C as functions of the temperature scaled by the Kondo temperature, respectively. The solid, dotted, and dashed lines represent the right-hand side of Eq. (102) with $j = 2$ and the phase shifts listed in Table II for runs A, B, and C, respectively. The inset shows the same moments and universal mappings as functions of the universal moment $\mathcal{L}_{00}^{(2)}(T/T_K)$. All curves, including those in the inset, are in close analogy with the plots in Fig. 8. In particular, in contrast with the main plot in Fig. 9, the three curves are close to congruence, because the right-hand side of Eq. (102) is insensitive to changes in the phase shift near $\delta = \pi/2$. Another contrast with Fig. 9 is the excellent agreement between each line and the corresponding set of circles, squares, or triangles, which indicates that the terms of $\mathcal{O}(\rho\epsilon)$ dropped in the derivation of Eq. (102) make smaller contributions to $\mathcal{L}_0$ and $\mathcal{L}_2$ than to $\mathcal{L}_1$.

c. Wiedemann-Franz law. The Wiedemann-Franz law states that the ratio between the thermal and electrical conductances is proportional to the temperature:

$$\frac{\kappa(T)}{G(T)} = L_0 T, \tag{104}$$

where $L_0 \equiv (\pi^2/3)(k_B/e)^2$ denotes the Lorenz ratio [61].

This expression of the equivalence between energy and charge transport results from rigorous expressions for the electrical and thermal conductances of free electrons. It is, therefore, reliable at Fermi-liquid fixed points. Here, the law is valid at the fixed points of the renormalization group transformation τ^2. At the LM and FL, Eq. (104) follows from Eqs. (102) and (103), which read

$$\left.\begin{aligned} \mathcal{L}_0 &= \frac{2}{h}\sin^2\delta, \\ \mathcal{L}_2 &= \frac{2\pi^2}{3h}\sin^2\delta \end{aligned}\right\} \quad (LM) \tag{105}$$

and

$$\left.\begin{aligned} \mathcal{L}_0 &= \frac{2}{h}\cos^2\delta, \\ \mathcal{L}_2 &= \frac{2\pi^2}{3h}\cos^2\delta. \end{aligned}\right\} \quad (FL) \tag{106}$$

As one might expect, Fig. 11 shows that the proportionality between $G(T)$ and $\beta\kappa(T)$ breaks down in the intermediate temperature range. The ratio $\beta\kappa/G$ peaks below the Kondo temperature, an indication that, as the temperature is reduced past T_K, the Kondo cloud starts to block charge transport more efficiently than to obstruct energy transport; at lower temperatures, the two forms of obstruction become comparable.

The peak is less pronounced for $V_g = -8U$ than for $V_g = -6.5U$. This is expected from Eqs. (102) and (103), which show that, as functions of the phase shift, the differences ΔG and $\Delta\kappa$, between the high- and low-temperature electrical and thermal conductances are maximized at the symmetric point, with $\delta = \pi/2$. As $|V_g + U/2|$ grows and $|\delta|$ is reduced, the differences shrink, and the thermal dependencies of the conductances become flatter. If the phase shift were $\delta = \pi/4$, both conductances would be independent of T, and Eq. (104) would be valid at all temperatures.

At the symmetric point $V_g = -U/2$, particle-hole symmetry forces the phase shift to be $\pi/2$. In the Kondo regime, as the numbers in Table II show, the phase shift stays close to $\pi/2$. Values closer to $\pi/4$ can only be found in the vicinity of the charge-degeneracy condition $V_g = -U$, where Eqs. (102) and (103) are invalid, because universality breaks down.

Nonetheless, the trend to thermal independence, of which $\delta = \pi/4$ is the extreme, emerges in the Kondo regime as the gate potential grows away from particle-hole symmetry. As a result, the deviations from Wiedemann-Franz behavior become less pronounced, and the peak drawn by the olive triangles and dashed line in Fig. 11 is substantially smaller than the one drawn by the magenta squares and dotted line, even though the phase shifts are by no means close to $\pi/4$.

The inset of Fig. 11 shows the Wiedemann-Franz ratio as a function of temperature for run A. With $\delta = \pi/2$, both G and $\beta\kappa$ vanish at $T = 0$. The ratio between the two conductances is hence determined by their low-temperature expansions and deviates from the Lorenz number. The oscillations in the plot are artifacts of the discretization that have been only partially eliminated by the averaging procedure.

d. Efficiency of the thermopower generator. To configure the device in Fig. 1 as a thermopower generator, one opens the circuit and keeps the left- and right-hand ends of the quantum wire at different temperatures T_L and T_R, respectively, with $T_L > T_R$. The efficiency of the generator is governed by the competition between the energy generated by the Seebeck voltage and the losses due to Joule heating and heat conduction across the wire. Large efficiencies result from the combination of large thermopowers S with large electrical conductances G, to reduce Joule heating, and small thermal conductances, to reduce heat transfer across the wire.

The competition is quantified by the dimensionless figure of merit

$$zT \equiv k_B T \frac{S^2(T)G(T)}{\kappa(T)}. \tag{107}$$

Specifically, $zT(T)$ provides an estimate for the efficiency η of the generator. If $zT(T)$ is approximately constant in the temperature range $T_L \geqslant T \geqslant T_R$, η is a function of the efficiency η_C of the Carnot cycle between T_L and T_R, the product zT_L, and the external load [62]. For fixed η_C, the efficiency η grows monotonically with zT. It is small for $zT \leqslant 1$ and approaches η_C for $zT \gg 1$ [62].

One can now relate the figure of merit to the energy moments. To this end, substitute the right-hand sides of Eqs. (71)–(73) for the transport properties in Eq. (107). It results that

$$zT = \frac{\mathcal{L}_1^2}{\mathcal{L}_0\mathcal{L}_2 - \mathcal{L}_1^2}. \tag{108}$$

Figure 12 show the temperature dependence of the product zT, calculated from Eq. (108). The circles, triangles, and squares show data computed in runs A, B, and C, respectively. The solid, dashed, and dotted lines resulted from substitution of Eqs. (101), (102), and (103) for $\mathcal{L}_1(T)$, $\mathcal{L}_0(T)$, and $\mathcal{L}_2(T)$, respectively. In the symmetric case, as expected since solid-state devices depend on particle-hole asymmetry to generate thermopower [62], the figure of merit equals zero at all temperatures. This result can also be understood from Eq. (107), given that $\mathcal{L}_1(T)$ vanishes under particle-hole symmetry.

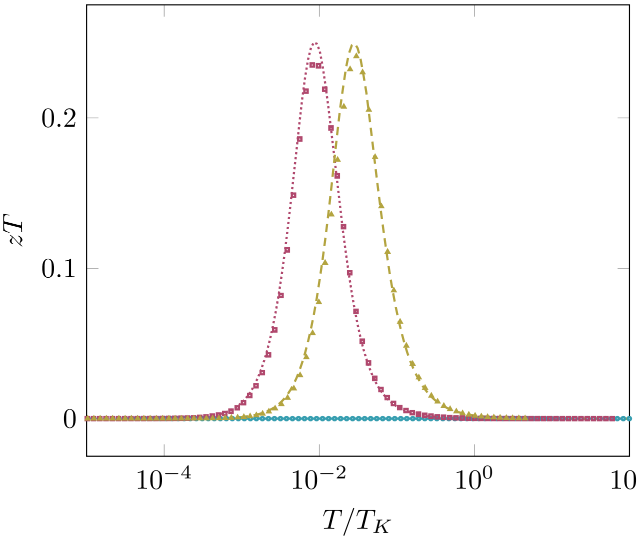

FIG. 12. Dimensionless figure of merit for thermoelectric efficiency as a function of temperature. The symbols and lines follow the convention in Fig. 6.

For each of the asymmetric runs B and C, zT peaks sharply, well below the Kondo temperature. Only for relatively small temperature differences around each peak does the figure of merit offer a reliable, significant estimate of η, and even then, with $zT < 0.25$, the effectiveness is very small. The side-coupled device is far from promising as a thermopower generator.

5. Comparison with mappings to universal functions for the serial geometry

As already mentioned, the mathematical analysis in Sec. IV B 3 is similar to the discussion of the serial geometry in Ref. [53], which derived mappings between the energy moments for the single-electron transistor to universal functions analogous to Eqs. (101)–(103). The following expressions were obtained [53]

$$\bar{\mathcal{L}}_0 = -\cos(2\delta)\frac{\pi^2}{2}\mathcal{L}_{11}^{(0)} + \frac{2}{h}\cos^2\delta, \tag{109}$$

analogous to Eq. (102),

$$\bar{\mathcal{L}}_1 = \frac{\pi}{\sqrt{2}}\sin(2\delta)\mathcal{L}_{01}^{(1)}, \tag{110}$$

analogous to Eq. (101), and

$$\bar{\mathcal{L}}_2 = -\cos(2\delta)\frac{\pi^2}{2}\mathcal{L}_{11}^{(2)} + \frac{2\pi^2}{3h}\cos^2\delta, \tag{111}$$

analogous to Eq. (103).

The right-hand sides of Eqs. (101) and (110) are identical, and the complementarity relations (89) and (90) bring the

TABLE III. Comparison between mappings for the side-coupled and serial geometries.

Side-coupled	Serial
$\mathcal{L}_0 = -\cos(2\delta)\mathcal{L}_{00}^{(0)} + \frac{2}{h}\cos^2(\delta)$	$\bar{\mathcal{L}}_0 = \cos(2\delta)\mathcal{L}_{00}^{(0)} + \frac{2}{h}\sin^2(\delta)$
$\mathcal{L}_1 = \frac{\pi}{\sqrt{2}}\sin(2\delta)\mathcal{L}_{01}^{(1)}$	$\bar{\mathcal{L}}_1 = \frac{\pi}{\sqrt{2}}\sin(2\delta)\mathcal{L}_{01}^{(1)}$
$\mathcal{L}_2 = -\cos(2\delta)\mathcal{L}_{00}^{(2)} + \frac{2\pi^2}{3h}\cos^2(\delta)$	$\bar{\mathcal{L}}_2 = \cos(2\delta)\mathcal{L}_{00}^{(2)} + \frac{2\pi^2}{3h}\sin^2(\delta)$

equations for the first and third moments into closer similarity: substitution of Eq. (89) for $(\pi^2/2)\mathcal{L}_{11}^{(0)}$, and of Eq. (90) for $(\pi^2/2)\mathcal{L}_{11}^{(2)}$ simplifies Eqs. (109) and (111), respectively. Table III collects the results and shows that the transformation $\delta \to \pi/2 - \delta$ interchanges the mappings for the side-coupled device and the single-electron transistor. Physically, the transport properties of the latter device are controlled by the screening charge around the quantum dot, while the screening charge surrounding the Wannier orbital f_0 governs the transport properties of the side-coupled device.

6. Comparison with experiments

The central results in Sec. IV B 3, Eqs. (101)–(103), simplify the interpretation of measurements. The scope of applications goes beyond devices like the one discussed in Sec. II, for transport in the parallel geometry of Fig. 1 is akin to conduction in bulk materials. This contrasts with the serial geometry of such devices as the single-electron transistor [46], in which the quantum dot allows conduction between two otherwise decoupled electron gases. The side-coupled dot obstructs transport, instead of assisting conduction. The obstruction is feeble at high temperatures, but its strength grows to the unitary limit as the temperature drops below T_K. The growth is tantamount to the low-temperature rise in the resistance of dilute magnetic alloys that motivated Kondo's classical paper [63]. To emphasize the equivalence, the following comparison with experimental data will focus on measurements of two bulk properties.

The comparison requires tabulation of the universal moments $\mathcal{L}_{00}^{(0)}(T/T_K)$, $\mathcal{L}_{01}^{(1)}(T/T_K)$, and $\mathcal{L}_{00}^{(2)}(T/T_K)$, an initial step requiring small computational effort. Once the three universal functions have been calculated, it becomes possible to fit the temperature dependence of transport properties measured in the Kondo regime. Since this second step involves two adjustable parameters, the Kondo temperature and phase shift, the linearity of the mappings (101)–(103) acquires special significance, because it supports algorithms that expedite the fitting, such as the ones described below.

a. Conductance. Since the conductance is proportional to $\mathcal{L}_0$, it follows from Eq. (102) that plots of $G(T/T_K)$ as functions of $\mathcal{L}_{00}^{(0)}(T/T_K)$ are straight lines. In practice, T_K is unknown. However, given that the curvature of the plot reverses as trial values for the Kondo temperature grow past T_K, a bisection algorithm readily yields the Kondo temperature. The slope or the intersection of the straight line then determines the phase shift. A number of examples dealing with conductance data from SET or side-coupled devices have been presented [53,54,60]. The algorithm yields excellent fits and allows accurate determination of the Kondo temperature, even though background currents of unknown origin increment the SCD conductances, while contact asymmetries restrict the SET conductances to maxima substantially below the conductance quantum.

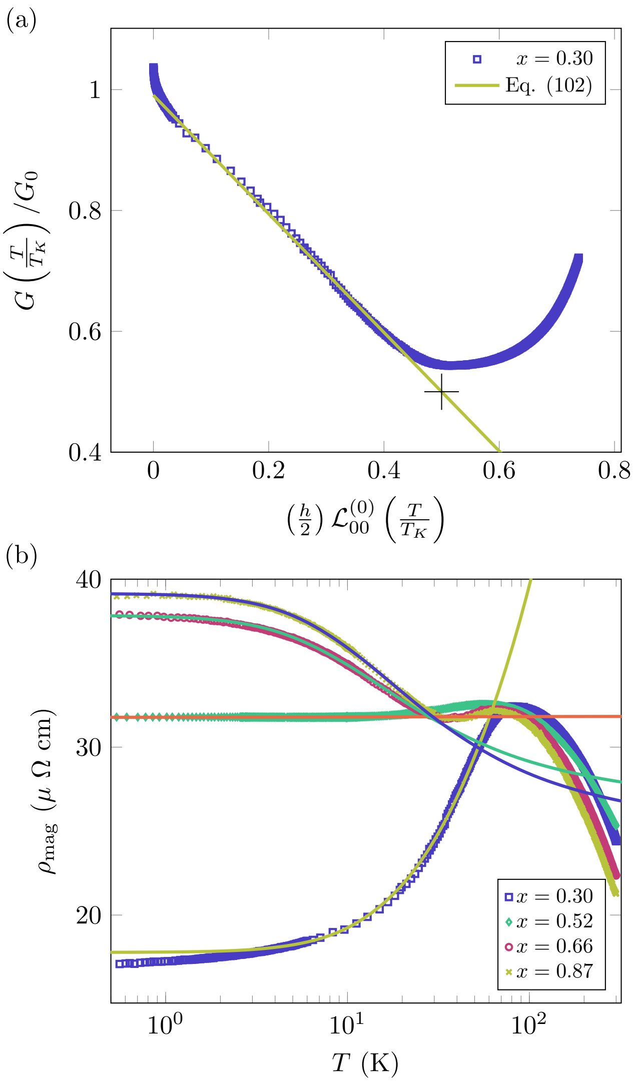

FIG. 13. (a) Fitting procedure, applied to the Ce-ion contribution to the temperature-dependent resistivity of $\mathrm{Ce_{0.7}La_{0.3}Rh_6Ge_2}$ reported in Ref. [64]. The small crosses are the experimental conductivities at the scaled temperatures T/T_K, divided by the adjustable factor $\mathcal{G}_0$ and plotted as functions of the universal function $G_K(T/T_K)$. The straight line is the linear mapping (102). The crosshairs mark the fiducial point $G(T = T_K) = \mathcal{G}_0/2$. (b) Temperature dependence of the Ce-ion contribution to the resistivity of $\mathrm{Ce_{1-x}La_xRh_6Ge_2}$ for the indicated dopant concentrations. The symbols show the excess resistivity defined by Eq. (112), and the solid lines, fits of the mapping (102) with the parameters in Table IV.

Bulk measurements offer an alternative that proves instructive. Figure 13 shows data recently reported by Xu *et al.* [64], who measured the resistivity of $\mathrm{Ce_{1-x}La_xRh_6Ge_4}$ for various dopant concentrations. At high dopant concentration, $x \to 1$, the Ce ions become impurities. At moderately low temperatures, of the order of 100 K, crystal field splittings freeze out all but the lowest, spin-degenerate ionic level, which becomes

TABLE IV. Parameters yielding the optimized fits in Fig. 13.

x	$\mathcal{G}_0$(kS/cm)	T_K(K)	δ/π
0.87	31.60	31.8	0.280
0.66	31.59	30.0	0.275
0.52	31.46	30.0	0.2504
0.30	31.50	60.5	0.111

equivalent to a spin-1/2 variable coupled to the conduction band. To identify the contribution of the associated magnetic moments to the resistivity $\rho(T)$, the authors have computed the excess resistivity

$$\rho_{\mathrm{mag}}(T) \equiv \frac{\rho_x(T) - \rho_{x=1}(T)}{1-x}. \tag{112}$$

The resulting experimental points for $x = 0.30,\ 0.52,\ 0.66$, and 0.87 are represented by the symbols in Fig. 13. The solid lines represent the right-hand side of Eq. (104) multiplied by the adjustable factor $\mathcal{G}_0$, equal to twice the conductivity at the Kondo temperature. Table IV lists the parameters resultant from the fits.

As an illustration of the fitting procedure, Fig. 13(a) plots the experimental conductance for the smallest dopant concentration, $x = 0.30$, at the scaled temperature T/T_K as a function of the universal moment $\mathcal{L}_{00}^{(0)}(T/T_K)$. The procedure starts with plots of this kind for various trial Kondo temperatures. The optimal choice, ($T_K = 60.5$ K for $x = 0.30$) maximizes the range of temperatures over which the data form a straight line. The ordinate of the straight line at the point $T = T_K$, equal to $\mathcal{G}_0/2$, yields the multiplicative parameter ($\mathcal{G}_0 = 31.50$ kS/cm for $x = 0.30$). The slope of the line, equal to $-\mathcal{G}_0\cos(2\delta)$, then determines the phase shift ($\delta = 0.111\,\pi$ for $x = 0.30$).

Analogous plots for $x = 0.52,\ 0.66$, and 0.87, which show superior agreement with straight lines, yield the data in Table IV. For the lower concentrations in Ref. [64] ($x =$ 0–0.25), the fitting procedure yields poor agreement with straight lines and, worse, slopes that are smaller than $-\mathcal{G}_0$, which correspond to $\cos(\delta) > 1$. This inconsistency with Eq. (102) indicates breakdown of Kondo-impurity physics, in harmony with the conclusions of Ref. [64].

For $x = 0.30$, in the temperature range $3\,\mathrm{K} < T < T_K$, the data in Fig. 13(a) practically coincide with the straight line. The disagreement above 60 K is due to broad maximum of the resistivity, as the fit to the +'s in Fig. 13(b) shows. All solid curves in Fig. 13(b) show similar incongruence with the experimental data, an indication that higher levels of the Ce ion, well above the ground-state doublet, make progressively larger contributions to the resistivity as T rises above 50 K.

At lower temperatures, all solid curves in Fig. 13(b) show excellent agreement with the experimental data over a wide range of temperatures. At the highest dopant concentrations, $x = 0.87,\ 0.66$, and 0.52, the congruence extends to the lowest temperature in the measurement, $T = 0.5$ K. At still lower concentration, as already discussed, there is significant deviation below 3 K for $x = 0.30$.

Equation (102) shows that the curvature of the resistivity is controlled by the phase shift. Below T_K, the curvature has the sign of $\cos(2\delta)$ and is hence positive for $\delta < \pi/4$. The different curvatures in Fig. 13(a) are associated with the phase shifts in Table IV, which decay from near $\pi/2$ in the La-rich sample to near 0 for $x = 0.30$.

This behavior is consistent with competition between the Kondo effect and the Ce-Ce RKKY interactions [28,41]. For samples with high La concentration concentration, the magnetic moments of the Ce ions are individually screened by the Kondo cloud, and the phase shift approaches $\pi/2$. As x diminishes, the RKKY interaction $\mathcal{I}$ between Ce ions grows. Under these conditions, the Kondo cloud first burgeons as the temperature drops from the vicinity of the local moment fixed point, but the RKKY interaction checks the expansion at $k_BT \approx \mathcal{I}$. The amount of screening is therefore limited, and the Friedel sum rule brings the phase shift down.

b. Thermopower. In contrast with the conductance, the thermopower maps nonlinearly onto the universal moments $\mathcal{L}_{00}^{(0)}$ and $\mathcal{L}_{01}^{(1)}$. A linear relation can, nevertheless, be established [53]. To this end, we substitute the right-hand side of Eq. (101) for $\mathcal{L}_1$ and the right-hand side of Eq. (102) for $\mathcal{L}_0$ on the right-hand side of Eq. (72). Straightforward manipulations then show that

$$\frac{h\mathcal{L}_{01}^{(1)}(T/T_K)}{eS(T/T_K)} = \frac{\sqrt{2}}{\pi}\left(h\cot(2\delta)\mathcal{L}_{00}^{(0)}(T/T_K) - \cot(\delta)\right). \tag{113}$$

The universal functions $\mathcal{L}_{00}^{(0)}(T/T_K)$ and $\mathcal{L}_{01}^{(1)}(T/T_K)$ are easily computed. Thus, given (i) a tabulation of thermopowers measured in a range of temperatures and (ii) a trial Kondo temperature T_K, the left hand-side of Eq. (113) can be computed and plotted as a function of the right-hand side. As in Sec. IV B 6 a, bisection indexed by the curvature of the plot then determines the Kondo temperature and, subsequently, the phase shift.

An example to demonstrate the effectiveness of this procedure seems warranted. No measurements of the thermopower in side-coupled geometry have been reported, however. While numerous studies focused on the conductance of nanostructured devices are found in the literature from the last two decades, the other transport properties have received virtually no attention, and the two recent exceptions preferred the bridge geometry [6,65].

Substitutional alloys with low concentration of a magnetic species offer an attractive alternative, since Eqs. (71)–(73) describe their transport properties in the dilute limit, up to a system dependent proportionality factor. Here, the discussion is centered on the rare-earth compound $\mathrm{Lu_{0.9}Yb_{0.1}Rh_2Si_2}$ and the thermal dependence of its thermopower at moderately low temperatures [66]. The crystal field of the lattice splits the ground-state multiplet of the free Yb ion into four doublets. The lowest doublet lies 210 K below the first excited one. To reduce the contribution from the excited doublets, the following analysis will be restricted to temperatures below 75 K. Under these conditions, the Yb becomes approximately equivalent to a spin-1/2 impurity coupled to the conduction electrons, a Kondo system, that is.

Figure 14 depicts the thermal dependence of the thermopower. The circles represent the laboratory data [66], and the solid line is an optimized fit rooted in the mappings (101) and (102). To account for the distinction between the one-

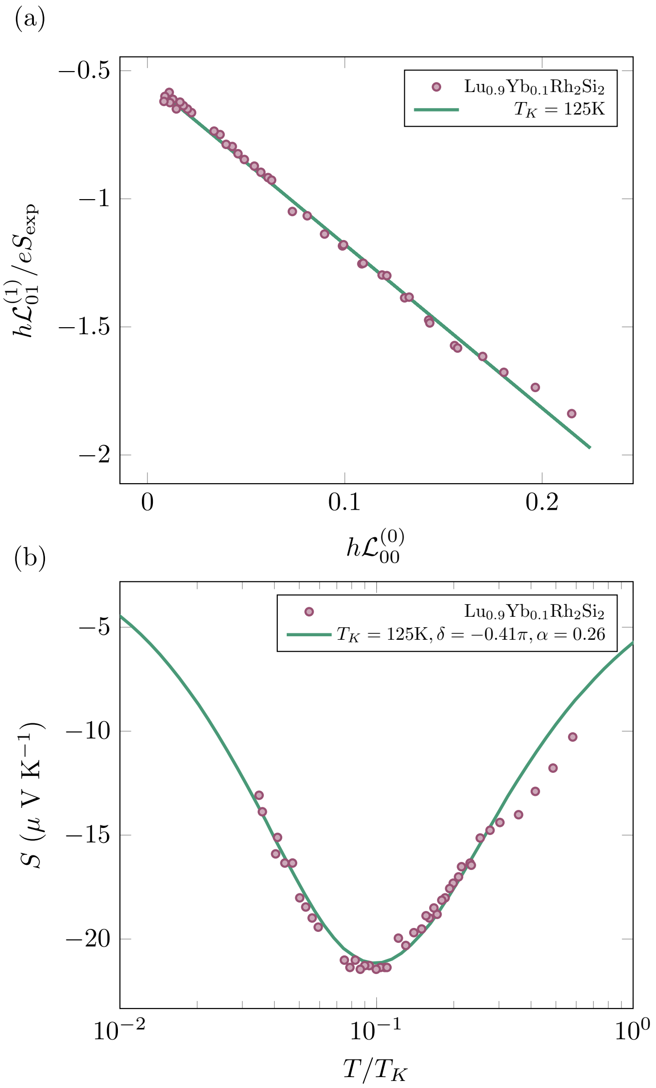

FIG. 14. Thermopower of the Kondo system $\mathrm{Lu_{0.9}Yb_{0.1}Rh_2Si_2}$. The filled circles are measurements reported in Ref. [66], and the solid lines are optimized fits resulting from Eq. (114) with the constants in the legend of (b). (a) plots the left-hand side of Eq. (114) as a function of $\mathcal{L}_{00}^{(0)}(T/T_K)$ to display the linear regression from which δ and α were obtained. (b) shows the Seebeck coefficient as a function of temperature.

dimensional side-coupled device and the lattice system, the left-hand side of Eq. (114) was multiplied by an adjustable dimensionless parameter α. This led to the expression

$$S(T) = \alpha \frac{2h}{e} \frac{\mathcal{L}_{01}^{(1)}(T)}{h\cot(2\delta)\mathcal{L}_{00}^{(0)} - \cot(\delta)} \quad \text{(bulk)}. \qquad (114)$$

The solid line in the figure represents Eq. (114) with $T_K = 125\,\mathrm{K}$, $\delta = 0.41$, and $\alpha = 0.26$. The Kondo temperature was determined by the aforementioned bisection procedure, which converged to the straight line fitting Eq. (114) in Fig. 14(a). The slope $m = -\alpha\cot(2\delta)$ and the intersection $c = \alpha\cot(\delta)$ of that line then determined the phase shift δ and coefficient α, and yielded the fit in panel (b). The systematic deviations separating the rightmost circles from the solid lines in both panels reflect the contributions from the excited doublets of the Yb ions, which are frozen out as the temperature is reduced below 40 K. The agreement in both panels confirms Köhler's interpretation [66], which associated the relatively high thermopower in the substitutional compound with the Kondo effect.

The order-of-magnitude difference between the Kondo temperatures in Ref. [66] and in Fig. 14 calls for a brief discussion. Köhler identified the Kondo temperature with the temperature T_{min} at which the thermopower is minimum. By contrast, we define T_K as the temperature $T_{1/2}$ at which the conductance is half the conductance quantum, that is, $G(T_K) = e^2/h$. As Figs. 5 and 6 show, the ratio between $T_{1/2}$ and T_{max} depends on particle-hole asymmetry. For runs A, B, and C, the ratios are approximately 3×10^{-1}, 2×10^{1}, and 8×10^{1}, respectively. On the bottom panel in Fig. 14 the last two values bracket the ratio $T_K/T_{\mathrm{min}} \approx 10$. The ratio between the Kondo temperature (125 K) calculated from Eq. (113) and the value (12 K) identified in the experimental report [66] is therefore in line with the numerical results.

c. Thermal conductance. The first term on the right-hand side of Eq. (73) is the energy moment $\mathcal{L}_2(T)$, which maps linearly onto the universal moment $\mathcal{L}_{00}^{(2)}$. Even though the second term breaks the linearity, it is a simple matter to restore it. The right-hand sides of Eqs. (101), (102), and (103) can be substituted for $\mathcal{L}_1$, $\mathcal{L}_0$, and $\mathcal{L}_2$ to convert Eq. (73) into a mapping that is approximately linear:

$$\beta\kappa(T/T_K) + \frac{\pi^2}{2}\frac{\left(\mathcal{L}_{01}^{(1)}(T/T_K)\right)^2\sin(2\delta)}{\frac{1}{h}\cot(\delta) - \cot(2\delta)\mathcal{L}_{00}^{(0)}(T)} = \frac{2\pi^2}{3h}\cos^2(\delta) - \cos(2\delta)\mathcal{L}_{00}^{(2)}(T). \qquad (115)$$

Equation (115) is less convenient than Eq. (113), or (114), because its left-hand side depends on the phase shift. An iterative procedure is now required to determine T_K and δ. The second term on the left-hand side vanishes for $\delta = \pi/2$, and is small in the Kondo regime. In the first iteration, that term is neglected, the left-hand side becomes analogous to Eq. (114), and the bisection procedure described in Secs. IV B 6 a and IVB6b yields a first estimate: $T_K = T_K^1$ and $\delta = \delta^1$. This concludes the first iteration.

In the nth iteration, substitution of T_K^{n-1} and δ^{n-1} for T_K and δ turns the second term on the right-hand side of Eq. (115) into a known function $f(T/T_K^{n-1})$. Given a trial T_K, the sum $\beta\kappa_{\mathrm{exp}}(T/T_K) + f(T/T_K^{n-1})$ can then be depicted as a function of $\mathcal{L}_{00}^{(2)}(T/T_K)$. This defines a bisection procedure indexed by the curvature of the plot, which determines the improved estimates T_K^n and δ^n, and closes iteration n.

Unfortunately, lack of pertinent experimental data precludes presentation of an example. Measurements of $\kappa(T)$ in lattice systems have been reported, but the contribution of the Kondo cloud cannot be extricated from the phonon and electron-phonon contributions to $\kappa(T)$ [67]. Measurements in side-coupled devices seem therefore necessary before Eq. (115) can be put to the test.

V. SUMMARY

This paper presents an alternative formulation of the NRG procedure, abbreviated eNRG because it is based on an exponentially growing sequence of blocks in real space, instead of on a logarithmic sequence of intervals in momentum space. Projection of the conduction-band Hamiltonian upon the resulting basis yields the discretized form (48), analogous to the codiagonal Hamiltonian generated by the logarithmic discretization [2]. The codiagonal coefficients t_n and $\bar{t}_n$ in the two series decay exponentially as n grows, and the identification $\lambda^2 \equiv \Lambda$ makes the sequence t_n $(n = 0, 1, \ldots)$ asymptotically proportional to the sequence $\bar{t}_n$ $(n = 0, 1, \ldots)$. The proportionality breaks down for small n because the two discretizations are applied to distinct dispersion relations: $\epsilon_k = -2t\cos(k)$ and $\epsilon_k = D(k - k_F)$ in the eNRG and NRG approaches, respectively.

Another distinction is the flexibility afforded by the second parameter in the eNRG discretization. The offset ζ controls the phase of the oscillations artificially added to the computed thermal dependence of physical properties. Averaging over two subsequent offsets eliminates such oscillations and yield accurate approximations to the continuum limit. In addition, larger offsets describe the conduction energies near the band edges more reliably. The high-temperature congruence between the eNRG-computed conductances and the exact results for the noninteracting model in Fig. 4 offers an illustration.

The numerically computed thermal properties for the interacting model, in Sec. IV B 4, survey the accuracy of the eNRG procedure. The eigenvalues and eigenvectors resultant from the iterative diagonalization of the model Hamiltonian yield the energy moments $\mathcal{L}_j$ $(j = 0, 1, 2)$ from which the electrical conductance $G(T)$, the Seebeck coefficient $S(T)$, and the thermal conductance $\kappa(T)$ are computed. As Figs. 8–10 show, the numerical results for the three energy moments agree very well with Eqs. (101), (102), and (103) in the Kondo regime, which map the thermal dependence of the moments onto the three universal functions $\mathcal{L}_{01}^{(1)}(T/T_K)$, $\mathcal{L}_{00}^{(0)}(T/T_K)$, and $\mathcal{L}_{00}^{(2)}(T/T_K)$, respectively.

The mappings onto the universal functions provide insight. To dwell on this point, Sec. IV B 4 c explains why the deviations from the Wiedemann-Franz law shrink as the model parameters move away from particle-hole symmetry. The final section, discusses the algorithms exploiting the linearity of the mappings to the universal functions to extract the Kondo temperature and phase shift from experimental data. Examples targeting electrical conductance data having been presented in previous publications, and the absence of experimental data in side-coupled geometry barring application to the thermal conductance, the illustration in Fig. 14 is focused on a measurement of the thermopower.

With exception of Fig. 4, the above-described results of the eNRG method are linked to universality and could have been obtained via NRG treatment. The eNRG is, however, more than a simple derivation of the NRG Hamiltonian. A real-space formulation is fitter to describe nanostructures than one in momentum space, especially when both involve projections upon incomplete bases. The eNRG construction is expected to describe the RKKY interaction between the magnetic moments of two impurities or quantum dots better than the NRG approach [28], for instance. Additional work is planned to unravel the full potential of the method.

ACKNOWLEDGMENTS

We are grateful to L. H. B. Guessi for suggestions and very helpful discussions, and to H. Yuan for sending us the high-quality experimental data reproduced in Fig. 13. This work has been supported by CAPES Grant No. 88887.475410/2020-00, CNPq Grant No. 312239/2018-1, and Fundação de Amparo à Pesquisa do Estado de São Paulo Grant No. 2017/26215-4.

APPENDIX A: DERIVATION OF Eq. (38)

The first term on the right-hand side of Eq. (37) reads

$$H_{f\lambda}^{\text{diag}} \equiv -t \sum_{n=1}^{\infty} \sum_{j=1}^{\lambda^n} (\alpha_{n,j}\alpha_{n,j+1}^* + \text{c.c.}) f_n^\dagger f_n . \tag{A1}$$

The superscript is a reminder that $H_{f\lambda}^{\text{diag}}$ only comprises the diagonal terms of $H_{f\lambda}$.

Since $H_{f\lambda}^{\text{diag}}$ has no counterpart in the original Hamiltonian, Eq. (28), we wish to choose the coefficients $\alpha_{n,j}$ so that the factor within parentheses in the summand on the right-hand side be equal to zero, for $n = 1, 2, \ldots$ and $j = 1, 2, \ldots, \lambda^n$. In other words, the $\alpha_{n,j}$ must satisfy the condition

$$\text{Re}(\alpha_{n,j}\alpha_{n,j+1}^*) = 0, \tag{A2}$$

from which it follows that the phases $\alpha_{n,j}$ and $\alpha_{n,j+1}$ differ by an odd multiple of $\pi/2$:

$$\phi_{n,j+1} = \phi_{n,j} + (2p+1)\frac{\pi}{2}, \tag{A3}$$

where p is an arbitrary integer.

The simplest expression satisfying Eq. (A3) is

$$\phi_{n,j} = \phi_n + j\frac{\pi}{2}, \tag{A4}$$

where ϕ_n denotes a phase that is uniform within each cell $\mathcal{C}_n$ $(n = 1, 2, \ldots)$.

The ϕ_n remain to be fixed. To this end, let us consider the second term on the right-hand side of Eq. (37):

$$H_{f\lambda}^{\text{off}} = -t \sum_{n=0}^{\infty} (\alpha_{n,\lambda^n}^* \alpha_{n+1,1} f_n^\dagger f_{n+1} + \text{H.c.}), \tag{A5}$$

where the superscript is a reminder that $H_{f\lambda}^{\text{off}}$ only comprises the off-diagonal terms of $H_{f\lambda}$.

The phase of the factor multiplying $f_n^\dagger f_{n+1}$ in the summand on the right-hand side of Eq. (A5) is

$$\phi_{n+1,1} - \phi_{n,\lambda^n} = \phi_{n+1} - \phi_n + \frac{\pi}{2}(1 - \lambda^n), \tag{A6}$$

which, in view of Eq. (32), can be written in the form

$$\phi_{n+1,1} - \phi_{n,\lambda^n} = \phi_{n+1} - \phi_n + \frac{\pi}{2}(1 - \mathcal{G}_{n+1} + \mathcal{G}_n). \tag{A7}$$

We want to make the coefficient of $f_n^\dagger f_{n+1}$ on the right-hand side of Eq. (A5) real positive. The phase difference (A7) must therefore be an odd multiple of π. To satisfy this requirement, we let

$$\phi_n = \frac{\pi}{2}(\mathcal{G}_n + n), \tag{A8}$$

a specification that makes the right-hand side of Eq. (A7) equal to π.

Equation (A8) turns the product of coefficients in the summand on the right-hand side of Eq. (A5) into a negative real number

$$\alpha_{n,\lambda^n}^* \alpha_{n+1,1} = -|\alpha_{n,\lambda^n}||\alpha_{n+1,1}|, \tag{A9}$$

so that Eq. (A5) reads

$$H_{f\lambda}^{\text{off}} = t\sum_{n=0}^{\infty}(|\alpha_{n,\lambda^n}||\alpha_{n+1,1}|\, f_n^\dagger f_{n+1} + \text{H.c.}). \tag{A10}$$

The absolute values $|\alpha_{n,j}|$ are subject to the normalization condition (35), which constrains the dependence on n, but not the dependence on j. The uniform-weight choice $|\alpha_{n,j}| = \alpha_n$ yields off-diagonal coefficients that decay exponentially with n, as a straightforward calculation shows. Specifically, the normalization condition yields

$$|\alpha_n| = \lambda^{-n/2}, \tag{A11}$$

so that Eq. (A10) becomes

$$H_{f\lambda}^{\text{off}} = t\sum_{n=0}^{\infty}(\lambda^{-(n+\frac{1}{2})}\, f_n^\dagger f_{n+1} + \text{H.c.}), \tag{A12}$$

which is equivalent to Eq. (42).

APPENDIX B: EXTENSIONS OF THE eNRG PROCEDURE

1. Alternative definitions of the absolute values $|\alpha_{n,j}|$

Equation (40) specifies the absolute values of the coefficients $\alpha_{n,j} \equiv \{f_n, a_{n,j}\}$ ($n = 0, 1, \ldots$; $j = 1, \ldots, \lambda^n$). While the specification of identical weights to all sites belonging to the same cell is appealing from the physical viewpoint, other choices are acceptable from the algebraic perspective. Simple examples merit discussion, for the sake of comparison. To facilitate normalization, it is convenient to let the $|\alpha_{n,j}|$ be proportional to a j-independent factor.

a. Arithmetic progression

As the first illustration, consider absolute values that grow linearly within each cell:

$$|\alpha_{n,j}| = \bar{\alpha}_n j \quad (n = 0, 1, \ldots; j = 1, \ldots, \lambda^n). \tag{B1}$$

The normalization condition now reads

$$\bar{\alpha}_n^2 \sum_{j=1}^{\lambda^n} j^2 = 1, \tag{B2}$$

from which it follows that

$$\bar{\alpha}_n = \sqrt{\frac{6}{(1+\lambda^{-n})(2+\lambda^{-n})}}\lambda^{-\frac{3n}{2}}. \tag{B3}$$

The product of absolute values on the right-hand side of Eq. (39) then becomes

$$|\alpha_{n,\lambda^n}||\alpha_{n+1,1}| = \frac{6\lambda^{-\frac{3}{2}}}{\sqrt{(1+\lambda^{-n})(1+\lambda^{-n-1})(2+\lambda^{-n})(2+\lambda^{-n-1})}}\lambda^{-2n}. \tag{B4}$$

In conclusion, the specification (B1) leads to codiagonal coefficients $\bar{t}_n$ that become proportional to λ^{-2n} at large n. This choice would identify the common ratio λ with $\Lambda^{1/4}$, instead of $\Lambda^{1/2}$. A common ratio $\lambda = 2$, for instance, would correspond to $\Lambda = 16$, and the discretization would introduce errors of $\mathcal{O}(\exp(-\pi^2/\ln\Lambda) \approx 3\%)$. Even purely practical considerations argue against Eq. (B1).

b. Hyperbolic dependence

The following specification merits more attention, for it may prove valuable for the study of nonequilibrium phenomena, as explained below:

$$|\alpha_{n,j}|^2 = \tilde{\alpha}_n^2 \cosh\left(r\left(j - \frac{\lambda^n+1}{2}\right)\right) \times (n = 0, 1, \ldots; j = 1, \ldots, \lambda^n), \tag{B5}$$

where the parameter r is a very small, positive real number, and the normalization condition (35) determines the prefactor $\tilde{\alpha}_n$:

$$\tilde{\alpha}_n^2 \sum_{j=1}^{\lambda^n} \cosh\left(r\left(j - \frac{\lambda^n+1}{2}\right)\right) = 1. \tag{B6}$$

The sum on the left-hand side of Eq. (B6) can be split into two geometrical series, evaluation of which shows that

$$\tilde{\alpha}_n^2 = \frac{\sinh(r/2)}{\sinh(r\lambda^n/2)}. \tag{B7}$$

This expression for the prefactor can now be combined with Eq. (B5) to determine the absolute values $|\alpha_{n,\lambda^n}|$ and $|\alpha_{n+1,1}|$ ($n = 0, 1, \ldots$) in the summand on the right-hand side of Eq. (A10), and the following equality results:

$$H_{f\lambda}^{\text{off}} = \sum_{n=0}^{\infty}(t_n\, f_n^\dagger f_{n+1} + \text{H.c.}), \tag{B8}$$

where

$$t_n = t\sinh\left(\frac{r}{2}\right)\sqrt{\frac{\cosh\left(\frac{r(\lambda^n-1)}{2}\right)\cosh\left(\frac{r(\lambda^{n+1}-1)}{2}\right)}{\sinh\left(\frac{r\lambda^n}{2}\right)\sinh\left(\frac{r\lambda^{n+1}}{2}\right)}} \times (n = 0, 1, \ldots). \tag{B9}$$

The parameter r, by assumption, is very small. For small n, such that $r\lambda^n \ll 1$, the arguments of the hyperbolic functions are small, and Eq. (B9) takes an approximate form that coincides with Eq. (A12):

$$t_n = t\lambda^{-(n+\frac{1}{2})} \quad (r\lambda^n \ll 1). \tag{B10}$$

At the opposite extreme, with n so large that $r\lambda^n \gg 1$, the square root on the right-hand side of Eq. (B9) approaches unity, and the codiagonal coefficients become approximately independent of n:

$$t_n = t\sinh\left(\frac{r}{2}\right) \quad (r\lambda^n \gg 1). \tag{B11}$$

We can see that, under the condition (B5), the codiagonal coefficients decay exponentially with n for small n and approach a constant at large n. The latter asymptotic form frees the resulting eNRG Hamiltonian from the limitation identified by Rosch [68], which precludes applications of the NRG procedure to nonequilibrium problems. In recent work, to surmount that limitation, Schwarz *et al.* [69] have brought forth a tight-binding Hamiltonian combining NRG-like codiagonal coefficients at high energies with a constant codiagonal coefficient at small energies. Equation (B9) interpolates smoothly between the two extremes and hence offers an alternative in the study of nonequilibrium phenomena.

2. Arbitrary filling of conduction band

The discretization of the model Hamiltonian is designed to reduce the number of levels in the spectrum. As a consequence, the number of electrons in the eigenstates of the discretized Hamiltonian is much smaller than in the model Hamiltonian. For this reason, both the NRG and eNRG approaches operate implicitly in the grand-canonical ensemble.

Usually, the chemical potential μ is set to zero. If the model Hamiltonian displays particle-hole symmetry, this adjustment becomes necessary to make the grand-canonical Hamiltonian symmetric, since μ changes sign under particle-hole transformations. The derivation of the Hamiltonian (42) from Eq. (37) took special care to preserve the particle-hole symmetry of the conduction band Hamiltonian: the phases of the coefficients $\alpha_{n,j}$ were chosen to eliminate the factors of the particle-hole asymmetric operators $f_n^\dagger f_n$ $(n = 0, 1, \infty; j = 1, \ldots, \lambda^n)$. This guaranteed the conduction band to be half-filled, and the chemical potential to be $\mu = 0$.

One might be interested, however, in other fillings of the conduction band, equivalent to $\mu \neq 0$. The grand-canonical form corresponding to Eq. (37) is, then,

$$\begin{aligned} H_\mu \equiv & -t\sum_{n=1}^{\infty}\sum_{j=1}^{\lambda^n-1}(\alpha_{n,j}\alpha_{n,j+1}^* + \text{c.c.})f_n^\dagger f_n \\ & - t\sum_{n=0}^{\infty}(\alpha_{n,\lambda^n}\alpha_{n+1,1}^* f_n^\dagger f_{n+1} + \text{H.c.}) - \mu N. \end{aligned} \tag{B12}$$

In contrast with our treatment of Eq. (37) in Sec. III B 2, there is no reason here to force the summand in the first sum on the right-hand side to be zero. Thus, instead of Eq. (38), an alternative expression must be allowed for the coefficients in the summand:

$$\alpha_{n,j} = |\alpha_n|e^{i\varphi_{n,j}} \quad (n = 0, 1, \ldots; j = 1, 2, \ldots, \lambda^n), \tag{B13}$$

with the same absolute values (40), but a more general expression for the phases:

$$\varphi_{n,j} = \gamma(\mathcal{G}_n - n + j) + n\pi, \tag{B14}$$

where γ is a constant that depends on μ. If $\mu = 0$, γ must be $\pi/2$ to make Eq. (B14) into congruence with Eq. (38).

We next substitute the right-hand side of Eq. (B14) for the phases of the coefficients $\alpha_{n,j}$ on the right-hand side of Eq. (B12) to show that

$$\begin{aligned} H_\mu = & -2t\cos(\gamma)\sum_{n=1}^{\infty}|\alpha_n|^2\sum_{j=1}^{\lambda^n-1}f_n^\dagger f_n \\ & + t\sum_{n=0}^{\infty}(|\alpha_n||\alpha_{n+1}|f_n^\dagger f_{n+1} + \text{H.c.}) - \mu N. \end{aligned} \tag{B15}$$

The normalization condition again yields Eq. (41) for $|\alpha_n|$ $(n = 0, 1, \ldots)$, which reduces Eq. (B15) to the simpler, more explicit form

$$\begin{aligned} H_\mu = & -2t\cos(\gamma)\sum_{n=1}^{\infty}(1-\lambda^{-n})f_n^\dagger f_n \\ & + \sum_{n=0}^{\infty}t_n(f_n^\dagger f_{n+1} + \text{H.c.}) - \mu N. \end{aligned} \tag{B16}$$

The constant γ must now be related to the chemical potential μ. To this end, it is convenient to write a more formal expression for Eq. (B16):

$$\begin{aligned} H_\mu = \lim_{\mathcal{M}\to\infty}\Bigg(& -2t\cos(\gamma)\sum_{n=0}^{\mathcal{M}}(1-\lambda^{-n})f_n^\dagger f_n \\ & + \sum_{n=0}^{\mathcal{M}}t_n(f_n^\dagger f_{n+1} + \text{H.c.}) - \mu N\Bigg). \end{aligned} \tag{B17}$$

Given that the trace of the grand-canonical Hamiltonian must remain finite as $N \to \infty$, the following expression results

$$\begin{aligned} & -2t\cos(\gamma)(\mathcal{M}+1) + 2t\cos(\gamma)\frac{1-\lambda^{-\mathcal{M}-1}}{1-\lambda^{-1}} - \mu(\mathcal{M}+1) \\ & = E_{\mathcal{M}} \quad (\mathcal{M}\to\infty), \end{aligned} \tag{B18}$$

where $E_{\mathcal{M}}$ approaches a finite constant in the infinite limit.

The first and second terms on the left-hand side of Eq. (B18) have absolute values that grow without limit as $\mathcal{M} \to \infty$. They must therefore cancel each other, which requires that

$$-2t\cos(\gamma) = \mu, \tag{B19}$$

and hence determines γ.

Substitution of the right-hand side of Eq. (B19) for the first term within parentheses on the right-hand side of Eq. (B17) then yields the desired expression for the discretized Hamiltonian:

$$H_\mu = \sum_{n=0}^{\infty}t_n(f_n^\dagger f_{n+1} + \text{H.c.}) - \sum_{n=0}^{\infty}\mu_n f_n^\dagger f_n, \tag{B20}$$

where

$$\mu_n \equiv \mu\lambda^{-n}. \tag{B21}$$

If $\mu = 0$, Eq. (B19) yields $\gamma = \pi/2$, and Eq. (B14) reduces to Eq. (A4), with the ϕ_n given by Eq. (A8).

3. Next-neighbor couplings

To discuss the flexibility of the eNRG construction in yet another context, this section considers a tight-binding Hamiltonian with near- and next-near-neighbor couplings:

$$\begin{aligned} H_{nn} = &-\sqrt{2}(ta_0^\dagger a_1 + ra_0^\dagger a_2 + \text{H.c.}) \\ &-\sum_{\ell=1}^{\infty}(ta_\ell^\dagger a_{\ell+1} + ra_\ell^\dagger a_{\ell+2} + \text{H.c.}). \end{aligned} \tag{B22}$$

Unlike the Hamiltonian (2), H_{nn} is particle-hole asymmetric, a circumstance calling for brief digression. The particle-hole transformation (12b) reverses the sign of the chemical potential. For particle-hole symmetric model Hamiltonians, any discretization procedure preserving the symmetry will therefore ensure that $\mu = 0$ after the discretization.

For particle-hole asymmetric Hamiltonians, by contrast, the approximation in Eq. (36) tends to shift μ. The chemical potential must then be adjusted so that the trace of the discretized grand-canonical Hamiltonian be equal to that of the model Hamiltonian. In the interest of briefness, the following analysis will start out with the discretization of the Hamiltonian H and turn to the grand-canonical Hamiltonian at the end. For definiteness, we will fix the offset $\zeta = 1$ and focus our attention on the second term on the right-hand side of Eq. (B22):

$$H_f^{nn} = -\sum_{\ell=1}^{\infty}(ta_\ell^\dagger a_{\ell+1} + ra_\ell^\dagger a_{\ell+2} + \text{H.c.}), \tag{B23}$$

The derivation follows the procedure in Sec. III B 2. Substitution of the right-hand side of Eq. (36) for the operators a_ℓ in Eq. (B22) yields the equivalent equality

$$\begin{aligned} H_{f\lambda}^{nn} = &-t\sum_{n=1}^{\infty}\sum_{j=1}^{\lambda^n-1}(\alpha_{n,j}\alpha_{n,j+1}^* + \text{c.c.})f_n^\dagger f_n \\ &-r\sum_{n=1}^{\infty}\sum_{j=1}^{\lambda^n-2}(\alpha_{n,j}\alpha_{n,j+2}^* + \text{c.c.})f_n^\dagger f_n \\ &-t\sum_{n=0}^{\infty}(\alpha_{n,\lambda^n}\,\alpha_{n+1,1}^*\,f_n^\dagger f_{n+1} + \text{H.c.}) \\ &-r\sum_{n=0}^{\infty}((\alpha_{n,\lambda^n}\,\alpha_{n+1,2}^* + \alpha_{n,\lambda^n-1}\,\alpha_{n+1,1}^*)\,f_n^\dagger f_{n+1} + \text{H.c.}). \end{aligned} \tag{B24}$$

Since the particle-hole symmetry of the Hamiltonian (B22) is broken by the terms proportional to r, the summand in the first term on the right-hand side must vanish. As explained in Sec. III B 2, Eq. (34), with the phases and absolute values given by Eqs. (38) and (40), respectively, satisfies this condition. Substitution of the same expression for the coefficients $\alpha_{n,j}$ ($n = 0, 1, \ldots;\ j = 1, \ldots, \lambda^n$) on the right-hand side of Eq. (B24) eliminates the first term on the right-hand side and reduces the coefficient of the summand in the third term to the product of the absolute values. The coefficients in the summands of the terms proportional to r are also determined by Eqs. (38) and (40). In the second term, the coefficients are real, given by the product of the absolute values: $\alpha_{n,j}\alpha_{n,j+2}^* = -|\alpha_n|^2$. In the fourth term, they are imaginary, $(\alpha_{n,\lambda^n}\,\alpha_{n+1,2}^* + \alpha_{n,\lambda^n-1}\,\alpha_{n+1,1}^*) = 2i|\alpha_n||\alpha_{n+1}|$. Given that $|\alpha_n| = \lambda^{-n/2}$ ($n = 0, 1, \ldots$), Eq. (B24) reduces to the equality

$$\begin{aligned} \mathcal{H}_{f\lambda}^{nn} = &\sum_{n=0}^{\infty}((t_n + 2ir_n)\,f_n^\dagger f_{n+1} + \text{H.c.}) \\ &+\sum_{n=1}^{\infty}(2r(1-2\lambda^{-n}) - \mu)f_n^\dagger f_n - \mu f_0^\dagger f_0\,, \end{aligned} \tag{B25}$$

where the t_n are given by Eq. (43), and the r_n, by an analogous equation:

$$r_n = r\lambda^{-n-\frac{1}{2}} \quad (n = 1, 2, \ldots). \tag{B26}$$

The infinite sums on the right-hand side of Eq. (B25) can then be truncated at $n = \mathcal{N}$, which yields the grand-canonical Hamiltonian

$$\begin{aligned} \mathcal{H}_{f\lambda}^{nn} = &\sum_{n=0}^{\mathcal{N}-1}((t_n + 2ir_n)\,f_n^\dagger f_{n+1} + \text{H.c.}) \\ &+2r\sum_{n=1}^{\mathcal{N}}(1-2\lambda^{-n})f_n^\dagger f_n - \mu\sum_{n=0}^{\mathcal{N}}f_n^\dagger f_n\,. \end{aligned} \tag{B27}$$

As in Appendix B 2, we must now set $\mu = 2r$ to ensure that the trace of the right-hand side remains finite as $\mathcal{N} \to \infty$. Substitution in the last term on the right-hand side of Eq. (B27) then yields the desired expression for the truncated grand-canonical Hamiltonian:

$$\begin{aligned} \mathcal{H}_{f\lambda}^{nn} = &\sum_{n=0}^{\mathcal{N}-1}((t_n + 2ir_n)\,f_n^\dagger f_{n+1} + \text{H.c.}) \\ &-4r\sum_{n=1}^{\mathcal{N}}\lambda^{-n}f_n^\dagger f_n - 2rf_0^\dagger f_0\,. \end{aligned} \tag{B28}$$

4. Two dots coupled to quantum wire

Figure 15 displays the geometry of discretization for quantum wires coupled to two dots d_L and d_R at sites $\ell = \pm r$. The model Hamiltonian now reads

$$\begin{aligned} H_2 = &\sum_{\alpha=L,R}H_{d,\alpha} + \mathcal{V}(d_R^\dagger c_\ell + d_L^\dagger c_{-\ell} + \text{H.c.}) \\ &-t\sum_{\ell=-\bar{L}}^{\bar{L}}(c_\ell^\dagger c_{\ell+1} + \text{H.c.}), \end{aligned} \tag{B29}$$

where the $H_{d,\alpha}$ are defined as in Eq. (3), with dot-dependent gate voltages $V_{g\alpha}$ and the Coulomb repulsions U_α ($\alpha = L, R$).

The separations $2r$ between the dots may be narrow, as in Fig. 15(a), or wide, as in Fig. 15(b). As the drawings show, it is convenient to define two symmetric cell sequences in the former case, and two symmetric pairs of sequences in the latter. For easier comparison, the same common ratio $\lambda = 2$ and offset $\zeta = 1$ defines all sequences in the two panels.

With $\zeta = 1$ the procedure in panel (a) bypasses the site $\ell = r$, which is coupled to the dot orbital d_R, and follows the construction in Fig. 3(b) to define the infinite cell sequence on

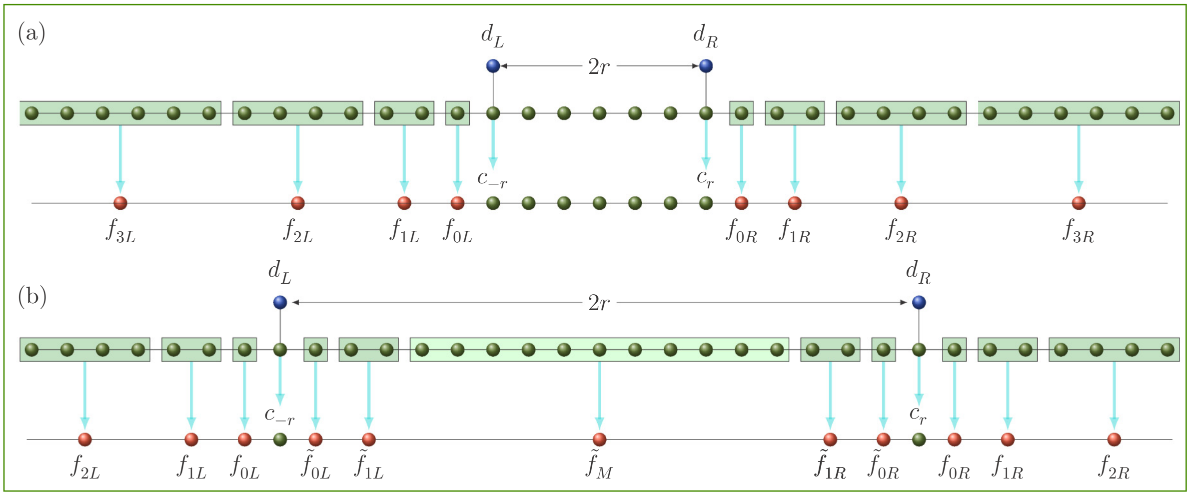

FIG. 15. eNRG discretization of the model Hamiltonian describing two quantum dots side-coupled to a quantum wire. The dots may be close to each other or widely separated, as (a) and (b) indicate, respectively. In each panel, the periodic sequence of spheres at the intermediate row represents the quantum wire. The two quantum dots, represented by the spheres at the top row, are coupled to lattice sites $2r$ apart. (a) shows two infinite sequences of cells defined as in Fig. 3(b), with common ratio $\lambda = 2$ and offset $\zeta = 1$. (b) defines two sequences, again with $\lambda = 2$ and $\zeta = 1$, starting from the site coupled to each dot. As in (a), the two outgrowing sequences are infinite. The ingrowing sequences merge to form the cell with lighter shading, centered at the midpoint between the dot sites.

the right-hand side of dot d_R. A symmetric sequence encloses the sites to the left of dot d_L. From the operators c_ℓ in $\mathcal{C}_n$ ($n = 0, 1, \ldots$), a single Fermi operator $f_n \equiv \lambda^{-n/2} \sum_\ell c_\ell$ is defined, as in Sec. III B 2. Similarly, from the $c_{-\ell}$ in $\bar{\mathcal{C}}_n$, a single operator $\tilde{f}_n \equiv \lambda^{-n/2} \sum_\ell c_{-\ell}$ is defined. Equation (B29) then takes the form

$$H_2^{(a)} = \sum_{\alpha=L,R} H_{d,\alpha} + \mathcal{V}(d_R^\dagger c_r + d_L^\dagger c_{-r} + \text{H.c.}) - t \sum_{\ell=-r}^{r-1} (c_\ell^\dagger c_{\ell+1} + \text{H.c.}) + \sum_{n=0}^{\infty} t_n (f_n^\dagger f_{n+1} + \tilde{f}_n^\dagger \tilde{f}_{n+1} + \text{H.c.}), \tag{B30}$$

with coefficients t_n given by Eq. (43).

The infinite sums on the right-hand side of Eq. (B30) are analogous to Eq. (42). The procedure in Sec. III B 3 truncates, defines a renormalization group transformation, and allows iterative diagonalization of H_2.

For large r, larger than $r = 5$, say, the sum proportional to $-t$ on the right-hand side of Eq. (B30) may make the cost of diagonalizing the truncated Hamiltonian excessive. Under these circumstances, the feasible alternative is the discretization scheme in Fig. 15(b).

Four sequences of cells are then constructed, around the dot sites, two growing away from the central region, and two growing towards the midpoint. The outgrowing sequences are infinite and follow the construction in panel (a). The first cells $\bar{\mathcal{C}}_n$ ($n = 0R, 1R, \ldots, NR$ and $n = 0L, 1L, \ldots, NL$) of the ingrowing sequences mirror the outgrowing cells, but the progressions run towards each other and must be interrupted at finite N to avoid overlap. As the example in Fig. 15(b) shows, the two sequences merge to form a cell $\mathcal{C}_M$. The cutoff N is the largest integer ensuring that $\mathcal{C}_M$ contains more than λ^N sites, that is, ensuring that the central cell is wider than the two neighboring cells. In the example, $\lambda^N = 2$, while the central cell contains 11 sites; if $\lambda^N = 4$, the central cell would contain only three sites.

Again, an operator $f_{\alpha n}$ ($n = 0, 1, \ldots; \alpha = L, R$) is associated with each cell in the outgrowing progressions, an operator $\bar{f}_{\alpha n}$ ($n = 0, 1, \ldots, N; \alpha = L, R$) with each cell in the ingrowing sequence, and the operator $\tilde{f}_M$ with the central cell. Projection of H_2 onto the resulting basis yields the expression

$$H_2^{(b)} = \sum_{\alpha=L,R} H_{d,\alpha} + \mathcal{V}(d_R^\dagger c_r + d_L^\dagger c_{-r} + \text{H.c.}) - t(c_\ell^\dagger (f_{0R} + \tilde{f}_{0R}) + c_{-\ell}^\dagger (f_{0L} + \tilde{f}_{0L}) + \text{H.c.}) + \sum_{\alpha=L,R} \left(\sum_{n=0}^{\infty} t_n f_{n\alpha}^\dagger f_{n+1\alpha} + \sum_{n=0}^{N-1} t_n \tilde{f}_{n\alpha}^\dagger \tilde{f}_{n+1\alpha} + \frac{t}{\sqrt{\lambda^N n_M}} \tilde{f}_{N\alpha}^\dagger \tilde{f}_M + \text{H.c.} \right), \tag{B31}$$

where n_M is the number of sites in cell $\mathcal{C}_M$. Like $H_2^{(a)}$, the Hamiltonian (B31) can be truncated and diagonalized iteratively, which gives access to its physical properties.

5. Analogue of the z trick

In the original formulation of the NRG, the infinite sequence $\mathcal{L}_\Lambda = \{D, D\Lambda^{-1}, D\Lambda^{-2}, \ldots\}$ defines the discretized states $a_{m\pm}$ ($m = 0, 1, \ldots$), as Eq. (20). The z *trick* chooses a second parameter z, a real number in the interval [0.5, 1.5] and generalizes the log sequence to $\mathcal{L}_{\Lambda,z} = \{D, D\Lambda^{-z}, D\Lambda^{-1-z}, D\Lambda^{-2-z}, \ldots\}$. This leads to a tridiagonal form like Eq. (24) with codiagonal coefficients $\bar{t}_n^z$ that must be determined numerically. At large n, the following expression replaces Eq. (26):

$$\bar{t}_n^z = D\frac{1+\Lambda^{-1}}{2}\Lambda^{1-z-\frac{n}{2}} \quad (\Lambda^{-n} \ll 1). \tag{B32}$$

The computed physical properties are now parametrized by Λ and z. Averaging of the results over z in the interval of definition virtually eliminates deviations artificially introduced by the discretization. A mathematical derivation analogous to the analysis in Appendix C, below, shows the amplitude of the deviations in equilibrium transport properties to be proportional to [37]

$$\bar{f}_{\Lambda,z} = \cos(\theta_1 + 2\pi(z-1))\exp\left(-\frac{\pi^2}{\ln(\Lambda)}\right). \tag{B33}$$

where θ_1 is the phase of the oscillation for $z = 1$.

With $z = 0.5$ the phase of the trigonometric function on the right-hand side of Eq. (B33) is $\theta_1 - \pi$. This shows that $f_{\Lambda,z=0.5}$ and $f_{\Lambda,z=1}$ have opposite signs. The average of the transport property over $z = 0.5$ and $z = 1$ eliminates the unphysical oscillations (B33).

The eNRG construction admits an analogous extension. The generalization modifies the number of sites defining the cells in Fig. 3. For simplicity, let the offset be $\zeta = 0$. As in Fig. 3, the first cell, $\mathcal{C}_0$, which is coupled to the impurity, contains a single site, in all cases. The neighboring cell $\mathcal{C}_1$ is called the *seed*. Let it contain w sites—w is the seed width. The subsequent cells $\mathcal{C}_n$ $(n = 2, 3, \ldots)$ are broadened by a factor w, that is, $\mathcal{C}_n$ contains $w\lambda^{n-1}$ sites.

The seed width $w = 1$ recovers the construction in Fig. 3(b). The width $w = \lambda$ recovers Fig. 3(a), but other choices, such as $w = 3$ with $\lambda = 2$ yield distinct sequences. The broadening affects the coefficients $\alpha_{n,j}$. From the specification (40) and the normalization condition (35) we now find the absolute values

$$|\alpha_{n,j}| = \begin{cases} 1 & (n=0) \\ (w\lambda^{n-1})^{-1/2} & (n \geqslant 1) \end{cases}. \tag{B34}$$

Equation (39) then yields the codiagonal coefficients. Notice taken that the coupling between a_0 and a_1 in Eq. (30) is $t\sqrt{2}$, we find that

$$t_n^w = \begin{cases} t\left(\frac{w}{2}\right)^{-1/2} & (n=0) \\ t(w\lambda^{n-\frac{1}{2}})^{-1} & (n \geqslant 1) \end{cases}. \tag{B35}$$

To relate the NRG parameter z to the eNRG parameter w, one must compare the right-hand sides of Eqs. (B32) and (B35). More specifically, one divides the former by the prefactor $D(1+\Lambda^{-1})/2$ (that is, the codiagonal coefficient for $n = 0$ and $z = 1$) and the latter by the corresponding prefactor $t\sqrt{\lambda}$ and equates the two quotients to obtain the mapping

$$z \equiv 1 + \frac{\ln(w)}{2\ln(\lambda)}. \tag{B36}$$

For $w = \lambda$ and $w = 1$, which correspond to Figs. 3(a) $(\zeta = 0)$ and Figs. 3(b) $(\zeta = 1)$, Eq. (B36) yields $z = 1.5$ and $z = 1$, respectively. For this reason, the amplitudes $f_{\lambda,\zeta}$ of the oscillations in physical properties computed with $\zeta = 0$ and with $\zeta = 1$ have opposite signs.

To reach the other limit of the $0.5 \leqslant z \leqslant 1.5$ interval, one must let the seed width be fractionary: Eq. (B36) maps $w = 1/\lambda$ to $z = 0.5$. The nonintegral value $w = 1/\lambda$ cannot be dismissed as atypical, given that the z interval comprises a continuum. The eNRG construction must therefore be further extended, to accommodate fractional and even irrational widths w. This recommends analytical continuation of the sequences in Eq. (B35).

Carlson's theorem proves instrumental in this context [70]. Even though the theorem admits a less restrictive statement, for our purposes it suffices to consider functions $f(\zeta)$ that are (i) analytic in the domain $\mathcal{D} : \{\varkappa \in \mathbb{C} \mid \mathbb{R}(\varkappa) \geqslant 0\}$ and have upper bounds, so that $|f(\varkappa)| \leqslant C$ for some real constant C. Under these conditions, the Theorem states that if $f(n) = 0$ for $n = 0, 1, 2, \ldots$, then $f(\varkappa) = 0$ for all $\varkappa \in \mathcal{D}$.

With the theorem in mind, we start out with the sequence t_0^w $(w = 1, 2, \ldots)$. Given λ, we seek an analytical function $f_0^t(\varkappa)$ $(\varkappa \in \mathcal{D})$ such that (i) $f_0^t(m) = t/\sqrt{\lambda^{-1}+m}$ for $m = 0, 1, \ldots$, and (ii) $|f_0^t(\varkappa)| \leqslant C$, for some real constant C. Conditional to the existence of this function, we define the auxiliary function

$$\mathscr{f}(\varkappa) \equiv f_0^t(\varkappa) - t(\lambda^{-1}+\varkappa)^{-1/2}, \tag{B37}$$

which must vanish identically for $\varkappa \in \mathcal{D}$, because it satisfies the requirements of Carlson's theorem.

Consequently,

$$f_0^t(\varkappa) = t(\lambda^{-1}+\varkappa)^{-1/2}, \tag{B38}$$

which satisfies the assumed conditions and, with w substituted for $\varkappa + \lambda^{-1}$ is the desired extension of the sequence $t_0(w)$ to nonintegral widths $w \geqslant \lambda^{-1}$.

The same reasoning applies to each of the other t_n^s $(n = 1, 2, \ldots)$ and shows that the function

$$f_n^t(\varkappa) \equiv t\lambda^{-n-\frac{1}{2}}(\lambda^{-1}+\varkappa)^{-1} \quad (n = 1, 2, \ldots) \tag{B39}$$

is the extension of $t_n(w)$ to nonintegral widths $w \geqslant \lambda^{-1}$.

In practice, Eqs. (B38) and (B39) validate Eq. (B35) for all real widths $w \geqslant \lambda^{-1}$. Equation (B36) maps this inequality onto the inequality $z \geqslant 0.5$. In particular, the standard NRG interval $0.5 \leqslant z < 1.5$ corresponds to the interval $\lambda^{-1} \leqslant w \leqslant \lambda$, and the amplitudes of the oscillations in the eNRG procedure are proportional to [37]

$$f_{\lambda,w} = \cos(\phi_w)\exp\left(-\frac{\pi^2}{2\ln(\lambda)}\right), \tag{B40}$$

where

$$\phi_w = \phi_1 + \pi\frac{\ln(w)}{\ln\lambda}, \tag{B41}$$

and ϕ_1 is the phase for $w = 1$.

To confirm Eq. (B41), Fig. 16 shows the conductance for the side-coupled device with $U = 0$, computed for widths $w = \lambda^{-1/2}, 1, \lambda^{1/2}$, and λ, to which Eq. (B36) associates $z = 0.75, 1, 1.25$, and 1.5, respectively. Each curve displays the expected sinusoidal oscillations around the continuum limit, due to the discretization of the conduction band levels. The phase of the oscillations grows uniformly from $\phi_1 - \pi/2$ for $w = \lambda^{-1/2}$ to $\phi_1 + \pi$ for $w = \lambda$. For $w = \lambda^{3/2}$ (not shown), the plot coincides with the solid light olive curve.

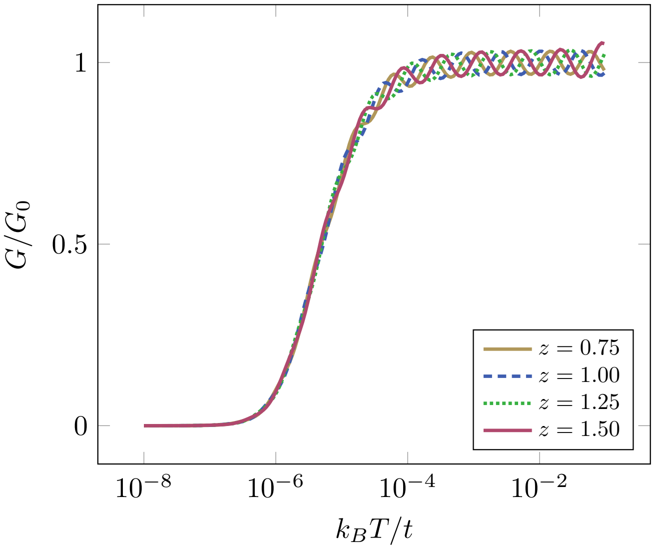

FIG. 16. Thermal dependence of the electrical conductance for the $U = 0$ side-coupled device calculated for four seed widths w. The solid light olive, dashed blue, dotted green, and dark magenta lines were computed with $w = 1/\sqrt{\lambda}$, 1, $\sqrt{\lambda}$, and λ, respectively, which Eq. (B36) maps onto the four indicated zs.

In computations of excitation properties the extension of Eq. (B35) to nonintegral w becomes especially important, because it allows numerical differentiation of excitation energies with respect to w. The resulting derivatives enter the z-trick algorithm allowing conversion of the discrete golden-rule transition lines into smooth spectra [35]. When thermodynamical or transport properties are wanted, the extension is of no importance, since averaging over two integer widths ($w = 1$ and $w = 0$, which correspond to offsets $\zeta = 1$ and $\zeta = 0$, respectively) is sufficient, as Eq. (B41) indicates, and the plots in Figs. 5–12 show. In fact, as illustrated by the computation in Sec. IV B 1, it is sufficient to average over two successive offsets ($\zeta = 3$ and 4, in the example), even though offsets $\zeta > 1$ find no equivalent in the w-construction.

6. Extension to nonintegral λ.

The common ratios λ defining the eNRG discretization are natural numbers, $\lambda = 1, 2, \ldots$. This should be sufficient for most applications. Nonetheless, given that the NRG procedure can be defined for arbitrary real $\Lambda > 1$, one may want to include real numbers in the set of allowed common ratios.

The extension poses no algebraic challenge. For $n > 0$, for instance, in analogy with the reasoning leading to Eq. (B37), we seek an analytic, bounded function $g_n^t(\mathscr{z})$ ($\mathscr{z} \in \mathcal{D}$) such that $g_n^t(m) = t(1+m)^{-(n+1/2)}$ ($m = 0, 1, \ldots$) and define the auxiliary function

$$\mathscr{g}(\mathscr{z}) \equiv g_n^t(\mathscr{z}) - t(1+m)^{-(n+1/2)}, \tag{B42}$$

which satisfies the requirements of Carlson's theorem and hence vanishes identically in $\mathcal{D}$.

It follows that

$$g_n^t(\mathscr{z}) = t(1+m)^{-n+1/2}. \tag{B43}$$

With $1 + m \to \lambda$, Eq. (B43) extends Eq. (43) to real $\lambda \geqslant 1$. Similar analysis extends Eq. (44).

Under certain physical conditions, such as application of a position-dependent potential to the lattice sites, it may be necessary to preserve the concept of a cell as a unit enclosing a natural number of sites. In such cases, the sequence of real numbers $1, \lambda, \lambda^2, \ldots$ becomes a mere guideline, and the nearest integer $\lceil \lambda^n \rfloor$ defines the number of sites in cell $\mathcal{C}_n$. Let $\lambda = \sqrt{2}$, for instance. To one decimal place, the sequence of real numbers reads 1, 1.4, 2.0, 2.8, 4, 5.7, 8, 11.3, 16.0, 22.6, …, and the cell sizes are 1, 1, 2, 3, 4, 6, 8, 11, 16, 23, …

The rounding of nonintegral numbers to the nearest integers tends to shift the number of sites in each cell, but the absolute value of the shift in each cell size is capped by 1/2. Since cell $\mathcal{C}_n$ ($n = 1, 2, \ldots$) contains approximately λ^n sites, the rounding of nonintegral numbers to the nearest integer introduces relative deviations $\mathcal{O}(0.5\lambda^{-n})$ in the normalizations in Eq. (41), which determine the codiagonal coefficients t_n ($n = 0, 1, \ldots$). Since the products $t_n f_n^\dagger f_{n+1}$ ($n = 0, 1, \ldots$) are irrelevant operators [2], the significance of such shifts decays rapidly as the energies of interest become much smaller than t.

APPENDIX C: ANALYTICAL COMPUTATION OF THE ELECTRICAL CONDUCTANCE AT A FIXED POINT

To offer insight into the dependence of physical properties on the eNRG discretization parameters, this Appendix computes the temperature-dependent electrical conductance at a fixed point of the renormalization group transformation. As explained in Sec. III B 5, the fixed-point Hamiltonian has quadratic form with eigenvectors $g_{\ell\pm}$ [$\ell = 0, 1, \ldots, (\mathcal{N}+1)/2$] corresponding to eigenvalues

$$\varepsilon_{\ell\pm} = \pm\lambda^{2(\ell\mp\frac{\delta}{\pi})}. \tag{C1}$$

To compute the conductance, we will need to express the eNRG operator f_0 on the basis of the eigenoperators $g_{\ell\pm}$. From analogy with the pertinent NRG expression one expects $\{f_0^\dagger, g_{\ell\pm}\}^2$ to be proportional to $\varepsilon_{\ell\pm}$. This is confirmed by numerical diagonalization of the fixed-point Hamiltonian (54). More specifically, fits to plots of $\{f_0^\dagger, g_{\ell\pm}\}^2/\varepsilon_{\ell\pm}$ as function of $1/\lambda^2$, for various ℓ, yields the following expression:

$$\{f_0^\dagger, g_{\ell\pm}\}^2 = \alpha_0^2\,\lambda^{2\ell}\cos^2\delta_\ell, \tag{C2}$$

where the coefficient is accurately described by the expression

$$\alpha_0^2 = \frac{1}{2\sqrt{\lambda}}\frac{1-\lambda^{-2}}{1+\lambda^{-2}}\left(1 + \frac{\lambda^{-4}}{(1+\lambda^{-2})^2}\right), \tag{C3}$$

with deviations that are insignificant [$\mathcal{O}(10^{-5})$] for $\lambda = 2$ and shrink as λ grows.

The conductance is given by Eq. (65). At a fixed point, Eqs. (C1)–(C3) bring that equality to the form

$$G(T) = \frac{G_0\alpha_0^2}{4\rho}\sum_{\ell\pm}\frac{\bar{\beta}\lambda^{2\ell}\cos^2\delta}{\cosh^2(\bar{\beta}\varepsilon_{\ell\pm}/2)}, \tag{C4}$$

with the shorthand

$$\bar{\beta} = t_{\mathcal{N}-1}\beta. \tag{C5}$$

Our choice of $\mathcal{N}$ makes $\bar{\beta} \ll 1$. For small ℓ, such that $\bar{\beta}\varepsilon_\ell/2 \ll 1$, the denominator of the fraction in the summand on the right-hand side of Eq. (C4) is approximately unitary, while the numerator is small. In the opposite extreme, for large ℓ, such that $\bar{\beta}\varepsilon\ell/2 \gg 1$, the denominator becomes very large, while the numerator is comparatively small. It follows that the sums over ℓ can be extended to $\pm\infty$, and the equality, rewritten as

$$G(T) = \frac{G_0\alpha_0^2\cos^2\delta}{4\rho}\Bigg(\sum_{\ell=-\infty}^{\infty}\frac{\bar{\beta}\lambda^{2\ell}}{\cosh^2(\bar{\beta}\varepsilon_{\ell+}/2)} + \sum_{\ell=-\infty}^{\infty}\frac{\bar{\beta}\lambda^{2\ell}}{\cosh^2(\bar{\beta}\varepsilon_{\ell-}/2)}\Bigg). \tag{C6}$$

Given the similarity between the two sums on the right-hand side of Eq. (C6), it is sufficient to evaluate the first one. To this end, we define the function

$$\Phi(\varkappa) \equiv \frac{(\bar{\beta}/w)\lambda^{2\varkappa}}{\cosh^2\left(\frac{\bar{\beta}}{2w}\lambda^{2(\varkappa-\frac{\delta}{\pi})}\right)}\cos^2\delta, \tag{C7}$$

which is real and analytic on the real axis.

A Sommerfeld-Watson transformation [71] then shows that

$$\sum_{\ell=-\infty}^{\infty}\Phi(\ell) = \int_{-\infty}^{\infty}\Phi(x)dx + 4\pi\,\mathrm{Im}\left(\sum_k R(k)\right), \tag{C8}$$

where $R(k)$ is the residue of the function

$$\phi(\varkappa) = \frac{\Phi(\varkappa)}{1-\exp(-2\pi i\varkappa)} \tag{C9}$$

at its kth pole in the upper half-plane $\mathrm{Im}(\varkappa) > 0$.

The factor $1/[1-\exp(-2\pi i\varkappa)]$ on the right-hand side in Eq. (C9) has poles on the real axis, but it is analytic in the upper half-plane. The numerator $\Phi(\varkappa)$ has poles at the zeros of the hyperbolic cosine on the right-hand side of Eq. (C7), that is, for $\varkappa = \varkappa_k$ satisfying

$$\frac{\bar{\beta}}{w}\lambda^{2\varkappa_k-\frac{\delta_k}{\pi}} = \pm(2k+1)\pi i \quad (k = 0, 1, 2, \ldots). \tag{C10}$$

If the sign is positive, the phase of the right-hand side is $(4m+1)\pi/2$ ($m = 0, \pm1, \pm2, \ldots$). If it is negative, the phase is $(4m+3)\pi/2$. The poles in the upper half plane therefore lie at

$$\varkappa(k) = \frac{\delta}{\pi} + \frac{\ln\left((w/\bar{\beta})\pi(2k+1)\right)}{2\ln\lambda} + \frac{(2m+1)\pi i}{4\ln\lambda} \quad (m = 0, 1, \ldots). \tag{C11}$$

This shows that the imaginary part of $\varkappa_k$ grows with m. In all cases, substitution of z_k for z in the denominator on the right-hand side of Eq. (C9) makes the exponential very large, even with $m = 0$. It is therefore a good approximation to substitute the product $-\Phi(z)\exp(2\pi iz)$ for the fraction and to consider only the residues of the poles with $m = 0$ and $k = 0, \pm1, \ldots$ in Eq. (C11).

Since the poles are of second order, the residue at the kth pole is

$$R(k) = \frac{\cos^2\delta\,\frac{d}{d\varkappa}\left(e^{2\pi iz}\frac{\bar{\beta}}{w}\lambda^{2\varkappa}\right)}{\sinh^2\left(\frac{\bar{\beta}}{2w}\lambda^{2(\varkappa-\frac{\delta}{\pi})}\right)\left(\frac{d}{dz}\left(\frac{\bar{\beta}}{2w}\lambda^{2(\varkappa-\frac{\delta}{\pi})}\right)\right)^2}\Bigg|_{\varkappa=\varkappa_k}, \tag{C12}$$

where $\varkappa_k$ denotes the right-hand side of Eq. (C11) with $m = 0$.

The squared hyberbolic sine in the denominator on the right-hand side of Eq. (C12) is unitary. The derivatives in the numerator and denominator are readily computed and yield the expression

$$R(\varkappa_k) = \frac{2\lambda^{\frac{2\delta}{\pi}}e^{2\pi i\varkappa_k}}{\frac{\bar{\beta}}{w}\lambda^{2(\varkappa_k-\frac{\delta}{\pi})}}\frac{\pi i+\ln\lambda}{\ln^2\lambda}\cos^2\delta. \tag{C13}$$

With $m = 0$, Eq. (C11) implies that $(\bar{\beta}/w)\lambda^{2(\varkappa_k-\delta/\pi)} = \pi(2k+1)i$. It follows that

$$\sum_k R(\varkappa_k) = 2\frac{\lambda^{2\frac{\delta}{\pi}}\cos^2\delta}{\pi\ln^2\lambda}(\pi - i\ln\lambda)\exp\left(\frac{-\pi^2}{2\ln\lambda}\right) \times\sum_{k=0}^{\infty}\frac{\exp\left\{i\left[2\delta+\pi\frac{\ln\left(\pi\frac{w}{\bar{\beta}}(2k+1)\right)}{\ln\lambda}\right]\right\}}{2k+1}. \tag{C14}$$

The term within the first parentheses on the right-hand side can be converted to polar form:

$$\pi - i\ln\lambda = \sqrt{\pi^2+\ln^2\lambda}\,\exp(i\varphi), \tag{C15}$$

where

$$\tan\varphi \equiv -\frac{\ln\lambda}{\pi}. \tag{C16}$$

This conversion brings Eq. (C14) to the form

$$\sum_k R(\varkappa_k) = \frac{2\lambda^{2\frac{\delta}{\pi}}\cos^2\delta}{\pi\ln^2\lambda}\sqrt{\pi^2+\ln^2\lambda}\,e^{i\left(\varphi+2\delta+\pi\frac{\ln(\pi\frac{w}{\bar{\beta}})}{\ln\lambda}\right)} \times e^{-\frac{\pi^2}{2\ln\lambda}}\lim_{k_M\to\infty}\sum_{k=0}^{k_M}\frac{e^{i\pi\frac{\ln(2k+1)}{\ln\lambda}}}{2k+1}. \tag{C17}$$

Regarded as functions of $\ln(k_M)$, the real and imaginary parts of the sum oscillate sinusoidally, with small amplitude and period $\ln\lambda$. Numerical averaging of sum on the right-hand side of Eq. (C17) over k_M yields

$$\left\langle\sum_{k=0}^{k_M}\frac{e^{i\pi\frac{\ln(2k+1)}{\ln\lambda}}}{2k+1}\right\rangle = \Xi\,e^{i\kappa}, \tag{C18}$$

where the modulus Ξ and phase κ are computed numerically. For $\lambda = 2$, for instance, $\Xi = 1.1$, and $\kappa = 0.18$ rad.

Substitution of Eq. (C18) on the right-hand side of Eq. (C8) finally yields the equality

$$\sum_{\ell=-\infty}^{\infty} \frac{\frac{\bar{\beta}}{w}\lambda^{2\ell}}{\cosh^2\left(\frac{\bar{\beta}\varepsilon_{\ell+}}{2w}\right)} \cos^2\delta = \int_{-\infty}^{\infty} \Phi(x)\,dx + 8\Xi\lambda^{2\frac{\delta}{\pi}} \frac{\sqrt{\pi^2+\ln^2\lambda}}{\ln^2\lambda} e^{-\frac{\pi^2}{2\ln\lambda}} \times \sin\left(\varphi + 2\delta + \kappa + \pi\frac{\ln\left(\pi\frac{w}{\bar{\beta}}\right)}{\ln\lambda}\right) \times \cos^2\delta. \tag{C19}$$

Similar analysis shows that, with the substitution $\delta \to -\delta$, the right-hand side of Eq. (C19) yields the second term within parentheses on the right-hand side of Eq. (C6).

These results provide insight into the numerical results in Secs. IV and VII. The first term on the right-hand side of Eq. (C19) is the continuum limit, the result that would be obtained if the calculations could be carried out with $\lambda = 1$. The second term describes the deviations introduced by the discretization. As in NRG computations, the deviations are periodic functions of $\ln(k_BT/t)$ with amplitude that grows with the discretization parameter. Roughly, the prefactor $\exp(-\pi^2/2\ln\lambda)$ controls the amplitude and makes the deviations small, even with $\lambda = 4$.

Equation (C19) shows that, at fixed temperature, the deviation from the continuum limit is a periodic function of the logarithmic width $\ln w$. Averaging over w eliminates the deviatios. In particular, since the offsets $\zeta = 0$ and $\zeta = 1$ are equivalent to $w = \lambda$ and $w = 1$, respectively, the deviations in the conductances computed with $\zeta = 0$ and $\zeta = 1$ have the same absolute value and opposite signs. To eliminate the artificial oscillations and unveil the continuum limit, it is therefore sufficient to average the conductances computed with these two offsets.

APPENDIX D: DERIVATION OF Eqs. (89) AND (90)

Equations (89) and (90) are immediate consequences of a linear relation between the spectral densities of the operators ϕ_0 and ϕ_1. To establish this relation, we consider the symmetric Anderson Hamiltonian and write down the Dyson equation for the retarded conduction-electron Green's function:

$$\mathbb{G}^S_{kk'}(\epsilon) = \mathbb{G}^0_k(\epsilon)\delta_{kk'} + \frac{V^2}{N}\mathbb{G}^0_k(\epsilon)\mathbb{G}^S_d(\epsilon)\mathbb{G}^0_{k'}(\epsilon), \tag{D1}$$

where the superindex S indicates association with the symmetric model, $\mathbb{G}^S_d(\epsilon)$ is the retarded dot-level Green's function, and $\mathbb{G}^0_k$ is the free conduction-electron Green's function:

$$\mathbb{G}^0_k = \frac{1}{\epsilon - \epsilon_k + i\eta}. \tag{D2}$$

We want to determine the spectral densities of the operators ϕ_0 and ϕ_1, which are linear combinations of the LM eigenoperators g_ℓ. The following equations relate the conduction-electron Green's function to the desired spectral densities:

$$\rho^S_0(\epsilon, T) = -\frac{1}{\pi N}\,\mathrm{Im}\sum_{kk'}\mathbb{G}^S_{kk'} \tag{D3}$$

and

$$\rho^S_1(\epsilon, T) = -\frac{2\rho^2}{\pi N}\,\mathrm{Im}\sum_{kk'}\epsilon_k\epsilon_{k'}\mathbb{G}^S_{kk'}. \tag{D4}$$

To determine ρ^S_0, we must sum both sides of Eq. (D1) over the momenta k and k':

$$\sum_{k,k'}\mathbb{G}^S_{kk'}(\epsilon) = \sum_k \mathbb{G}^0_k + \frac{V^2}{N}\left(\sum_k \mathbb{G}^0_k\right)^2 \mathbb{G}^S_d(\epsilon). \tag{D5}$$

Given Eq. (D2), it is straightforward to compute the sums over momenta on the right-hand side of Eq. (D5). It results that

$$\sum_k \mathbb{G}^0_k = -\pi\rho N i + \mathcal{O}(\rho\epsilon). \tag{D6}$$

At the low temperatures of interest, terms of $\mathcal{O}(\rho\epsilon)$ can be safely neglected. Substitution of the right-hand side of Eq. (D6) for the sums on the right-hand side of Eq. (D5) reduces the latter to the expression

$$\sum_{k,k'}\mathbb{G}^S_{kk'}(\epsilon, T) = -\pi\rho N\big(i + \pi\rho V^2\mathbb{G}^S_d(\epsilon, T)\big). \tag{D7}$$

Comparison with Eq. (D3) then yields the following expression for the ϕ_0 spectral function:

$$\rho^S_0(\epsilon, T) = \rho - \pi\rho\Gamma\rho^S_d(\epsilon, T), \tag{D8}$$

where

$$\rho^S_d(\epsilon, T) = -\frac{1}{\pi}\,\mathrm{Im}\,\mathbb{G}^S_d(\epsilon, T) \tag{D9}$$

is the dot-level spectral density.

Analogous algebra relates ρ_1 to ρ^S_d. Multiplication of both sides of Eq. (D1) by $\epsilon_k\epsilon_{k'}$ followed by summation over both momenta yields the equality

$$\sum_{k,k'}\epsilon_k\epsilon_{k'}\mathbb{G}^S_{kk'}(\epsilon) = \sum_k \epsilon_k^2\mathbb{G}^0_k + \frac{V^2}{N}\left(\sum_k \epsilon_k\mathbb{G}^0_k\right)^2\mathbb{G}^S_d(\epsilon). \tag{D10}$$

The first term on the right-hand side of Eq. (D10) is of $\mathcal{O}(\rho\epsilon)$. The sum within parentheses in the second factor is given by an equality analogous to Eq. (D6):

$$\sum_k \epsilon_k\mathbb{G}^0_k = N + \mathcal{O}(\rho\epsilon). \tag{D11}$$

Comparison with Eq. (D4), now yields the following expression for the ϕ_1 spectral density:

$$\frac{\pi}{2}\rho^S_1(\epsilon, T) = \rho\Gamma\rho^S_d(\epsilon, T). \tag{D12}$$

The left-hand side of Eq. (D12) can now substituted for $\rho\Gamma\rho_d^S(\epsilon, T)$ in the last term on the right-hand side of Eq. (D8), with the result

$$\rho_0^S(\epsilon, T) = \rho - \frac{\pi^2}{2}\rho_1^S(\epsilon, T). \tag{D13}$$

The universal moments $\mathcal{L}_{00}^{(j)}(T/T_K)$ $(j = 0, 2)$ are the energy moments $\mathcal{L}_j(T/T_K)$ for the particle-hole symmetric model. In other words, they can be obtained from by Eq. (68) with ρ_0^S substituted for ρ_0, in the integrand on the right-hand side:

$$\mathcal{L}_{00}^{(j)} \equiv \frac{2}{\rho h}\int\left(-\frac{\partial f_\beta}{\partial\epsilon}\right)\rho_0^S(\epsilon, T)(\beta\epsilon)^j\,d\epsilon \quad (j = 0, 2). \tag{D14}$$

Likewise, the moments $\mathcal{L}_{11}^{(j)}$ $(j = 0, 2)$ are related to the ϕ_1 spectral density:

$$\mathcal{L}_{11}^{(j)} \equiv \frac{2}{\rho h}\int\left(-\frac{\partial f_\beta}{\partial\epsilon}\right)\rho_1^S(\epsilon, T)(\beta\epsilon)^j\,d\epsilon \quad (j = 0, 2). \tag{D15}$$

Substitution of the right-hand side of Eq. (D13) for ρ_0^S on the right-hand side of Eq. (D14) and comparison with Eq. (D15) then leads to the expression

$$\mathcal{L}_{00}^{(j)}(T/T_K) = \frac{2}{h}\int\left(-\frac{\partial f_\beta}{\partial\epsilon}\right)(\beta\epsilon)^j\,d\epsilon - \frac{\pi^2}{2}\mathcal{L}_{11}^{(j)}(T/T_K) \times (j = 0, 2). \tag{D16}$$

The integral on the right-hand side of Eq. (D15) is dimensionless. For $j = 0$, it is unitary, and Eq. (89) follows. For $j = 2$, the integral equals $\pi^2/3$, and Eq. (90) follows.

[1] K. G. Wilson, Rev. Mod. Phys. **47**, 773 (1975).
[2] H. R. Krishna-murthy, J. W. Wilkins, and K. G. Wilson, Phys. Rev. B **21**, 1003 (1980).
[3] H. R. Krishna-murthy, J. W. Wilkins, and K. G. Wilson, Phys. Rev. B **21**, 1044 (1980).
[4] R. Bulla, T. A. Costi, and T. Pruschke, Rev. Mod. Phys. **80**, 395 (2008).
[5] R. Patel, Y. Agrawal, and R. Parekh, Microsystem Technologies **27**, 1863 (2021).
[6] B. Dutta, D. Majidi, A. García Corral, P. A. Erdman, S. Florens, T. A. Costi, H. Courtois, and C. B. Winkelmann, Nano Lett. **19**, 506 (2019).
[7] T. A. Costi, Phys. Rev. B **100**, 161106(R) (2019).
[8] T. A. Costi, Phys. Rev. B **100**, 155126 (2019).
[9] Y.-C. Xiong, N. Nan, Y.-Z. Dong, Z.-D. He, Z.-W. Zhu, and Y.-P. Wu, Results Phys. **15**, 102601 (2019).
[10] G. Barcza, K. Bauerbach, F. Eickhoff, F. B. Anders, F. Gebhard, and Ö. Legeza, Phys. Rev. B **101**, 075132 (2020).
[11] J. Böeker and F. B. Anders, Phys. Rev. B **102**, 075149 (2020).
[12] G.-Y. Yi, C. Jiang, L.-L. Zhang, S.-R. Zhong, H. Chu, and W.-J. Gong, Phys. Rev. B **102**, 085418 (2020).
[13] H. T. M. Nghiem, H. T. Dang, and T. A. Costi, Phys. Rev. B **101**, 115117 (2020).
[14] J. B. Rigo and A. K. Mitchell, Phys. Rev. B **101**, 241105(R) (2020).
[15] C. A. Philipps, P. G. B. Shiota, F. M. Zimmer, and J. V. B. Ferreira, J. Magn. Magn. Mater. **499**, 166259 (2020).
[16] Y. Teratani, R. Sakano, T. Hata, T. Arakawa, M. Ferrier, K. Kobayashi, and A. Oguri, Phys. Rev. B **102**, 165106 (2020).
[17] G. Diniz, G. S. Diniz, G. B. Martins, and E. Vernek, Phys. Rev. B **101**, 125115 (2020).
[18] F. Eickhoff, E. Kolodzeiski, T. Esat, N. Fournier, C. Wagner, T. Deilmann, R. Temirov, M. Rohlfing, F. S. Tautz, and F. B. Anders, Phys. Rev. B **101**, 125405 (2020).
[19] B. M. de Souza Melo, L. G. G. V. D. da Silva, A. R. Rocha, and C. Lewenkopf, J. Phys.: Condens. Matter **32**, 095602 (2020).
[20] N. Nan, W. Li, P.-C. Wang, Y.-J. Hu, G.-L. Tan, and Y.-C. Xiong, Phys. Chem. Chem. Phys. **23**, 5878 (2021).
[21] M. Debertolis, S. Florens, and I. Snyman, Phys. Rev. B **103**, 235166 (2021).
[22] G. T. D. Pedrosa, J. F. Silva, and E. Vernek, Phys. Rev. B **103**, 045137 (2021).
[23] M. Žonda, O. Stetsovych, R. Korytar, M. Ternes, R. Temirov, A. Raccanelli, F. S. Tautz, P. Jelínek, T. Novotny, and M. Svec, J. Phys. Chem. Lett. **12**, 6320 (2021).
[24] P. Zalom and T. Novotny, Phys. Rev. B **104**, 035437 (2021).
[25] A. K. Mitchell, M. R. Galpin, S. Wilson-Fletcher, D. E. Logan, and R. Bulla, Phys. Rev. B **89**, 121105 (2014).
[26] K. M. Stadler, A. K. Mitchell, J. von Delft, and A. Weichselbaum, Phys. Rev. B **93**, 235101 (2016).
[27] B. Bruognolo, N.-O. Linden, F. Schwarz, S.-S. B. Lee, K. Stadler, A. Weichselbaum, M. Vojta, F. B. Anders, and J. von Delft, Phys. Rev. B **95**, 121115(R) (2017).
[28] J. B. Silva, W. L. C. Lima, W. C. Oliveira, J. L. N. Mello, L. N. Oliveira, and J. W. Wilkins, Phys. Rev. Lett. **76**, 275 (1996).
[29] R. Bulla, H.-J. Lee, N.-H. Tong, and M. Vojta, Phys. Rev. B **71**, 045122 (2005).
[30] J. W. M. Pinto and L. N. Oliveira, Comput. Phys. Commun. **185**, 1299 (2014).
[31] V. L. Campo and L. N. Oliveira, Phys. Rev. B **72**, 104432 (2005).
[32] P. W. Anderson, J. Phys. C **3**, 2436 (1970).
[33] B. Jones, Phys. B: Condens. Matter **171**, 53 (1991).
[34] D. C. Langreth, Phys. Rev. **150**, 516 (1966).
[35] H. O. Frota and L. N. Oliveira, Phys. Rev. B **33**, 7871 (1986).
[36] M. Yoshida, M. A. Whitaker, and L. N. Oliveira, Phys. Rev. B **41**, 9403 (1990).
[37] W. C. Oliveira and L. N. Oliveira, Phys. Rev. B **49**, 11986 (1994).
[38] K. Chen, C. Jayaprakash, and H. R. Krishnamurthy, Phys. Rev. Lett. **58**, 929 (1987).
[39] R. M. Fye, J. E. Hirsch, and D. J. Scalapino, Phys. Rev. B **35**, 4901 (1987).
[40] B. A. Jones and C. M. Varma, Phys. Rev. Lett. **58**, 843 (1987).
[41] B. A. Jones, C. M. Varma, and J. W. Wilkins, Phys. Rev. Lett. **61**, 125 (1988).

[42] B. A. Jones, C. M. Varma, and J. W. Wilkins, Phys. Rev. Lett. **61**, 2819 (1988).

[43] R. M. Fye, Phys. Rev. Lett. **72**, 916 (1994).

[44] I. Affleck, A. W. W. Ludwig, and B. A. Jones, Phys. Rev. B **52**, 9528 (1995).

[45] T. A. Costi, A. C. Hewson, and V. Zlatic, J. Phys.: Condens. Matter **6**, 2519 (1994).

[46] D. Goldhaber-Gordon, H. Shtrikman, D. Mahalu, D. Abusch-Magder, U. Meirav, and M. A. Kastner, Nature (London) **391**, 156 (1998).

[47] D. Goldhaber-Gordon, J. Göres, M. A. Kastner, H. Shtrikman, D. Mahalu, and U. Meirav, Phys. Rev. Lett. **81**, 5225 (1998).

[48] S. M. Cronenwett, H. J. Lynch, D. Goldhaber-Gordon, L. P. Kouwenhoven, C. M. Marcus, K. Hirose, N. S. Wingreen, and V. Umansky, Phys. Rev. Lett. **88**, 226805 (2002).

[49] M. Yoshida and L. N. d. Oliveira, Phys. B: Condens. Matter **404**, 3312 (2009).

[50] T. A. Costi and V. Zlatić, Phys. Rev. B **81**, 235127 (2010).

[51] V. Schöps, V. Zlatić, and T. A. Costi, J. Phys.: Conf. Ser. **273**, 012155 (2011).

[52] M. Yoshida, A. C. Seridonio, and L. N. Oliveira, Phys. Rev. B **80**, 235317 (2009).

[53] D. F. Aranguren-Quintero, E. Ramos, J. Silva-Valencia, M. S. Figueira, L. N. Oliveira, and R. Franco, Phys. Rev. B **103**, 085112 (2021).

[54] A. C. Seridonio, M. Yoshida, and L. N. Oliveira, Europhys. Lett. **86**, 67006 (2009).

[55] A. C. Seridonio, M. Yoshida, and L. N. Oliveira, Phys. Rev. B **80**, 235318 (2009).

[56] T.-S. Kim and S. Hershfield, Phys. Rev. Lett. **88**, 136601 (2002).

[57] J. R. Schrieffer and P. A. Wolff, Phys. Rev. **149**, 491 (1966).

[58] F. D. M. Haldane, Phys. Rev. Lett. **40**, 416 (1978).

[59] F. D. M. Haldane, An extension of the Anderson model as a model for mixed valence rare earth materials, Ph.D. thesis, U. Cambridge, 1978.

[60] K. Zawadzki and L. N. Oliveira, Eur. Phys. J. B **91**, 136 (2018).

[61] N. Ashcroft and N. Mermin, *Solid State Physics* (Holt, Rinehart and Winston, New York, 1976).

[62] S. W. Angrist, *Direct Energy Conversion*, 3rd ed., Allyn and Bacon series in Mechanical Engineering and Applied Mechanics (Allyn and Bacon, Boston, 1977).

[63] J. Kondo, Prog. Theor. Phys. **32**, 37 (1964).

[64] J.-C. Xu, H. Su, R. Kumar, S.-S. Luo, Z.-Y. Nie, A. Wang, F. Du, R. Li, M. Smidman, and H.-Q. Yuan, Chin. Phys. Lett. **38**, 087101 (2021).

[65] A. Svilans, M. Josefsson, A. M. Burke, S. Fahlvik, C. Thelander, H. Linke, and M. Leijnse, Phys. Rev. Lett. **121**, 206801 (2018).

[66] U. Köhler, Thermoelectric transport in rare-earth compounds, Ph.D. thesis, Technical University Dresden, Dresden, Germany, 2007; U. Köhler, N. Oeschler, F. Steglich, S. Maquilon, and Z. Fisk, Phys. Rev. B **77**, 104412 (2008).

[67] A. K. Bashir, M. B. T. Tchokonté, D. Britz, B. M. Sondezi, A. M. Strydom, and D. Kaczorowski, J. Phys.: Conf. Ser. **592**, 012004 (2015).

[68] A. Rosch, Eur. Phys. J. B **85**, 6 (2012).

[69] F. Schwarz, I. Weymann, J. von Delft, and A. Weichselbaum, Phys. Rev. Lett. **121**, 137702 (2018).

[70] E. C. Titchmarsh, *The Theory of Functions*, 2nd ed. (Oxford University Press, London, 1939), see Sec. 5.81.

[71] J. Matthews and R. L. Walker, *Mathematical Methods of Physics* (Addison Wesley, 1971).